2020

Integration of Large PV Power Plants and Batteries in the Electric Power System

Oluwaseun M. Akeyo
University of Kentucky, ochichikeyo@gmail.com
Author ORCID Identifier:
https://orcid.org/0000-0002-2862-9527
Digital Object Identifier: https://doi.org/10.13023/etd.2020.448

STUDENT AGREEMENT:

I represent that my thesis or dissertation and abstract are my original work. Proper attribution has been given to all outside sources. I understand that I am solely responsible for obtaining any needed copyright permissions. I have obtained needed written permission statement(s) from the owner(s) of each third-party copyrighted matter to be included in my work, allowing electronic distribution (if such use is not permitted by the fair use doctrine) which will be submitted to UKnowledge as Additional File.

I hereby grant to The University of Kentucky and its agents the irrevocable, non-exclusive, and royalty-free license to archive and make accessible my work in whole or in part in all forms of media, now or hereafter known. I agree that the document mentioned above may be made available immediately for worldwide access unless an embargo applies.

I retain all other ownership rights to the copyright of my work. I also retain the right to use in future works (such as articles or books) all or part of my work. I understand that I am free to register the copyright to my work.

REVIEW, APPROVAL AND ACCEPTANCE

The document mentioned above has been reviewed and accepted by the student's advisor, on behalf of the advisory committee, and by the Director of Graduate Studies (DGS), on behalf of the program; we verify that this is the final, approved version of the student's thesis including all changes required by the advisory committee. The undersigned agree to abide by the statements above.

Oluwaseun M. Akeyo, Student

Dr. Dan M. Ionel, Major Professor

Dr. Daniel Lau, Director of Graduate Studies

Integration of Large PV Power Plants and Batteries in the Electric Power System

DISSERTATION

A dissertation submitted in partial fulfillment of the requirements for the degree of Doctor of Philosophy in the College of Engineering at the University of Kentucky

By

Oluwaseun Akeyo

Lexington, Kentucky

Director: Dr. Dan M. Ionel, Professor and L. Stanley Pigman Chair in Power

Lexington, Kentucky 2020

https://orcid.org/0000-0002-2862-9527

ABSTRACT OF DISSERTATION

INTEGRATION OF LARGE PV POWER PLANTS AND BATTERIES IN THE ELECTRIC POWER SYSTEM

The declining cost of renewables, the need for cleaner sources of energy, and environmental protection policies have led to the growing penetration of inverter-based resources such as solar photovoltaics (PV), wind, and battery energy storage systems (BESS) into the electric power system. The intermittent nature of these resources poses multiple challenges to the power grid and substantial changes in the conventional generation and electrical power delivery practices will be required to accommodate the large penetration of these renewable power plants. The impact of large solar PV penetration on both generation and transmission systems, and the use of BESS to mitigate some of the challenges due to solar PV penetration has been studied in this dissertation.

One of the major challenges in evaluating the impact of inverter-based resources (IBR) such as solar PV systems is developing an equivalent model adequate to represent its operation. This work proposes a detailed solar PV model suitable for analyzing the configurations, design, and operation of multi-MW grid connected PV systems. This model which takes into account the contributions of the power electronics control and operation was used to evaluate the impact of transient changes in solar PV power on an example transmission system. The benefits of a battery system configuration connected to the grid through an independent inverter were analyzed and its operation during transient conditions was also evaluated.

After developing a detailed solar PV and BESS modules for analyzing the effect of IBR on transmission systems, an innovative approach for evaluating the impact of solar PV plants on both generation and transmission system based on a practical minute-to-minute economic dispatch model was proposed. The study demonstrates that large solar PV penetration may lead to both over- and under-generation violations, and substantial changes to conventional generation dispatch and unit commitment will be required to accommodate the growing renewable solar PV penetration.

The terminal voltage of a battery pack varies based on multiple parameters and cannot be modeled as a constant voltage source for a detailed analysis BESS operation. A novel approach for estimating the equivalent circuit parameters for utility-scale BESS using equipment typically available at the installation site was proposed in this dissertation. This approach can be employed by utilities for monitoring energy storage system operation, ensure safety and avoid lithium-ion battery "thermal runaway".

The new methods developed, configurations and modules proposed in this dissertation may be directly applicable or extended to a wide range of utility practices for evaluating the impact of renewable resources and estimating the maximum solar PV capacity a service area can accommodate without significant upgrades to existing infrastructures.

KEYWORDS: Solar PV, battery, hosting capacity, economic dispatch, PV penetration, parameter estimation

Author's signature: Oluwaseun Akeyo

Date: November 11, 2020

Integration of Large PV Power Plants and Batteries in the Electric Power System

By

Oluwaseun Akeyo

Director of Thesis: Dr. Dan M. Ionel

Director of Graduate Studies: Dr. Daniel Lau

Date: November 11, 2020

To Oretha and Jayden

ACKNOWLEDGEMENTS

I will start by expressing my profound gratitude and appreciation to my Ph.D. advisor, Professor Dan M. Ionel, FIEEE whose guidance, support, and encouragement have been invaluable not just in my academic development but also in my personal life. Through his teachings and vision I have learned to strive relentlessly to accomplish ambitious goals and productively contribute to research and profession. I am very fortunate and most grateful to have an advisor who created a home for me in the SPARK Laboratory family, not only directing my Ph.D. studies in a fashion second to none, but also a mentor who saw my development potential leading to early career achievements.

I would also like to extend my sincere thanks to post-doctoral and insightful mentor, Dr. Vandana Rallabandi, now with GE Research and with whom I had the privilege of working in the SPARK Laboratory. Her teachings and advice on electric power systems will forever stay with me.

I am very thankful for the continued support of my Ph.D. committee members, Professors Aaron Cramer, Nicholas Jewell, Yuan Liao, Joseph Sottile, and of the outside examiner, Professor Gabriel Dadi. Their valuable feedback greatly contributed to the development of the dissertation.

My utmost gratitude is due to the Louisville Gas and Electric, and Kentucky Utilities (LG&E and KU), University of Kentucky, the L. Stanley Pigman endowment, the Power and Energy Institute of Kentucky (PEIK) and the Electrical and Computer Engineering Department for the support over the years and through my Ph.D. studies.

At LG&E and KU, special thanks are due to Mr. Aron Patrick for his technical advice for the development of the minute-based dispatch model, and of the systematic evaluation framework for transmission and generation. His strong support and close

mentorship, including personal teachings applicable to my future career in industry, are gratefully acknowledged. I have collaborated with Dr. Nicholas Jewell on the battery energy storage system experiments and simulations and greatly benefited of his expertise and friendly help for which I am very thankful.

I will also thank my student colleagues from the SPARK Laboratory family: Damien, Donovin, Evan, Gerald, Huanjie, Murat, Narges, Rosemary, Yibin, and senior colleague Dr. Peng Han for their kind support and special friendship.

I can never give enough gratitude to my loving parents, Engr. Micheal Akeyo and Mrs. Victoria Akeyo, who have given me unending love and sacrificed the most to support me throughout my life. Thank you both for providing me with all the tools I need to reach my dreams.

The greatest appreciation goes to my darling wife, Oretha Akeyo, and my dear son, Jayden Akeyo, for the sensational impact their presence, love and affection had on my Ph.D. years.

Akeyo Oluwaseun

November, 2020

Contents

List of Tables

List of Figures

Chapter 1

Introduction and Problem Formulation

1.1 Background

Due to the rapid decline in cost, the need for clean alternative energy resources, and favoring energy policies, the installed capacity of intermittent renewable energy resources has been exponentially growing over the past two decades. Further growth is expected with policy targets for renewable energy installations and decarbonization of the world [1]. A significant portion of carbon and greenhouse gas emission is related to electricity generation, therefore, the electric sector remains the main target for renewable adoption.

The transition from conventional fossil-based electricity generation to renewable sources poses a significant threat to the stability of the electric grid mainly due to the intermittency of renewable sources. Hence, it is of timely interest to identify the challenges related to high renewable systems penetration, propose alternatives for maximizing energy from installed renewable systems, recommend approaches to mitigate challenges related to intermittency, and estimate the maximum renewable

hosting capacity for a specified network without significant upgrades to its existing infrastructure.

Furthermore, significant changes in conventional generator operation and transmission system planning will be required to accommodate increasing solar PV penetration. Therefore, utilities and regulatory bodies need to evaluate the impact of increasing solar PV penetration in their network while considering the responses of conventional generators in order to estimate their system hosting capacity.

The impact of high renewable energy system penetration and the maximum intermittent resources that can be connected to a transmission network will vary by circuit and depend on multiple factors including the point of interconnection, thermal limit of connecting transmission lines, and voltage violations. This makes it necessary to exhaustively evaluate the impact of solar PV plant performance on a network circuit and identify necessary upgrades required to ensure stable operation.

Battery energy storage systems (BESS) can in principle be integrated to mitigate most of the challenges related to renewable sources intermittency. However, there are substantial safety concerns in addition to the relatively high cost, preventing global deployment of BESS. Hence, effective performance evaluation and monitoring techniques will be required to ensure stable operation.

A detailed equivalent circuit model for battery energy storage systems can provide additional insight into its operation and evaluate its performance to ensure safe utilization. Since utility-scale BESS typically include multiple cells with different chemical composition connected in series and parallel, a straight-forward methodology for estimation its equivalent circuit parameters using equipment readily available

at the installation site is vital.

There are multiple configurations for integrating solar PV and BESS into the power system. The selected configuration has multiple impacts on the system operation including the capacity factor, cost, efficiency, and overall stability. Also, the characteristics of the battery system and its voltage variation range is required for effective power electronics design.

This dissertation systematically evaluates the impact of integrating large solar PV plant and BESS in the electric power system. One of the main contributions of this dissertation is proposing a practical minute-to-minute economic dispatch model capable of capturing the effect of solar PV intermittency and estimating the maximum capacity a generation portfolio can accommodate. Other example challenges addressed in this study include the optimal sizing of a BESS for improving the PV capacity factor and hosting capacity of a network and a novel technique for estimating the equivalent circuit parameters for a utility-scale BESS.

1.2 Literature review

The integration of solar PV and other inverter-based resources (IBR) must respect standards and grid codes enforced by the service area [2]. These standards provide the technical specifications for testing, and validating the interoperability of utility-scale and distributed renewable energy resources [3, 4]. However, these standards are mostly focused on a single interconnection request and do not provide details related to the combined impact of multiple inverter-based resources connection.

Until recently, inverter-based resources have been regulated to disconnected during

transient disturbances or fault conditions that threaten the stability of the power grid [5]. However, current studies have validated that IBR can contribute unique functionalities that may improve the performance of the grid during transient and steady-state conditions [6]. For systems with substantial inverter-based resources, their disconnection from the grid during the transient period will not decrease the disturbance but mostly likely intensify its impact on the grid [7].

Inverter based resources such as solar PV systems have been represented as controllable current and power sources in average model simulation studies, which do not require the evaluation of power electronics converter and control [8]. Since renewable sources such as solar PV plants require adequate power electronics conversion system to be connected to the ac grid, power electronic topologies with and without dc-dc converter have been proposed for the design and simulation studies of solar PV systems [9]. Designs including wide band-gap devices, which increase the overall system efficiency and in some cases eliminates the need for traditional transformer for grid integration have been proposed [10, 11].

Battery energy storage systems (BESS) can in principle be integrated into the grid to mitigate the challenges related to solar PV penetration [12]. These BESS can also be configured to provide other grid ancillary services in addition to supporting the solar PV operation [13]. Advanced BESS operation modes such as frequency-watt, Volt-VAr, and Volt-Watt have demonstrated the benefits of these systems and further emphasize their role in the future electric power system [14].

There is a limit to the maximum amount of renewable sources that may be connected to a network without a need for significant changes to the existing infrastructure and operation [15]. The maximum amount of renewable penetration on the power system depends on the limits of the transmission and distribution circuits as well as the physical limits of the connected generators [16, 17]. Recent literature has been focused on either evaluating the impact of intermittent renewable sources on generation or transmission systems [18–21]. For the studies related to impact on generation, hourly economic dispatch models have mostly been employed [22]. These models assume changes in aggregated electrical demand are minimal and generation capacity can always match demand [23]. Economic dispatch models may be employed to analyze the impact of renewable penetrations as well as recommend additional generation resources that may be required to increase renewable energy sources penetration [24, 25].

Furthermore, proposed frameworks for evaluating the impact of solar PV on transmission systems have mostly adopted standard dispatch models, which follow a linear generation capacity dispatch [26]. Transmission and distribution circuit parameters such as voltage deviations, transmission line thermal limits, frequency variation, and total harmonic distortion may be used to estimate the PV hosting capacity of a network [27, 28].

A detailed model of the renewable system components is required to effectively analyze their impact on the grid. Some literature exist on methods to develop equivalent circuit models on PV and battery systems [29–31]. Dynamic electromagnetic transient models for solar PV systems have been proposed in [32, 33]. This model is

suitable for solar PV systems within a range limited by its configuration and component specifications. An extensive effort and complex approach will be required for detailed dynamic models whose capacity can vary over wide ranges.

The future grid may be able to take advantage of the predominantly Lithium-ion based BESS at multiple power distribution levels. A detailed model of the BESS will be required for monitoring its performance and recommending changes to enhance its operation. In addition to the detailed power electronics configuration and control, an equivalent circuit model including multiple parameters will be required for a BESS model. Battery system parameter estimation algorithms for single-cell based on recursive least square methods [34, 35], augmented unscented Kalman filter, and particle swarm optimization techniques have been proposed [36]. Furthermore, approaches for scaling up the parameters of single cells to represent a battery system with multiple cells have been evaluated [37].

Analyses have demonstrated that single-stage PV systems are cheaper, smaller in size, and more efficient compared to dual-stage systems with dc-dc converters [38, 39]. Conventionally, configurations for integrating BESS into existing PV plants include two dc-dc converters with substantial losses in the additional components [40]. In [41], a battery pack was directly connected to the dc-link between the dc-dc and ac-dc converter of a PV system. However, this configuration requires additional overvoltage protection for the safe operation of the battery system.

Extensive literature review on more detailed aspects of the challenges and recommendations for renewable integration is distributed throughout this dissertation and included in each chapter. These include methodologies for mitigating the impact of

large PV plants using BESS, the maximum PV hosting capacity for generation and transmission systems based on economic dispatch models, the approaches for developing a detailed model of PV and battery system equivalent circuit, and configurations for integrating BESS into existing PV plants to increase its capacity factor.

1.3 Research objectives, dissertation outline, and original contributions

Research objectives - Statement of problem

Conventional generation planning and operation practices have to adapt to changes in the generation mix, which mostly trends from the transition from the conventional synchronous ac rotation machines to inverter-based resources in the form of PV, wind, battery, and other systems. Due to the peculiar nature of these resources, a detailed model capable of capturing the dynamics of their components and control is required to evaluate their impact on the traditional power systems.

Solar PV plants can lose up to 90% of its output power in one minute. Hence, traditional hourly dispatch models are incapable of evaluating the impact of solar PV intermittency on the power system and identifying periods of generation imbalances due to solar PV penetration. Furthermore, large inverter-based resources penetration may have a significant impact on the transmission network operation and a detailed evaluation of the system voltage response, branch power flow, and overall operation during transient and steady-state operation is required to estimate the maximum PV penetration the system can sustain without needing significant changes to existing

infrastructure.

In order to evaluate the performance of BESS, ensure safety operation, and develop accurate models for simulation studies, a detailed equivalent circuit model (ECM) of the battery system is required. Conventional approaches for estimating the ECM of battery cell requires subjecting it to charge/discharge cycles in a laboratory setup, which will be complex and unsuitable for a utility-scale battery system which includes thousands of cells connected in series and parallel.

It is of timely interest to propose and evaluate configurations for adequately integrating BESS with existing solar PV systems to improve its capacity factor, mitigate challenges related to its intermittency and support the overall operation of the power system. Conventional configurations are expensive, require a new power converter system and complex changes to the PV system operation.

Another issue specific to solar PV and BESS system integration is the preferred power and energy capacity for the BESS and application to size it for. Parameters such as the location of the PV system, its ac and dc capacities, and the regulation limits for the service area are vital for estimating the BESS capacity for mitigating the solar PV intermittency challenges and enhancing its operation. Therefore, the optimal battery capacity becomes complicated due to the diverse application and variation in solar PV irradiance based on geographical location.

Dissertation outline:

For the purpose of effectively evaluating the impact of intermittent renewable energy sources and analyzing methodology for integrating BESS in the power system, the following chapters have been included in this dissertation.

Chapter 2 proposes an approach for developing electromagnetic models for utility-scale PV and BESS. This model captures the contribution of inverter-based resources power electronics and can be employed for analyzing their transient effect on the traditional power system. Chapter 3 presents a framework, which includes a minute-to-minute economic dispatch model that may be used to estimate the maximum PV system a select network can sustain without significant upgrades to the existing infrastructure. Chapter 4 introduces a novel framework for estimating the equivalent circuit parameters of utility-scale BESS using equipment typically available at the installation site. A new configuration for dc connected battery and PV systems that may be adopted for significant increases in PV capacity factor, inverter utilization factor, and array MPPT stability is presented in chapter 5. Conclusions and future works are provided in chapter 6.

Original contributions:

The challenge of effectively evaluating the impact of inverter-based resources on the power system becomes complex when the setup includes a considerable amount of modular plants. In this dissertation, an approach for developing utility-scale electromagnetic transient models for IBR based on an operational 10MW PV plant and a 1MW/2MWh BESS was proposed. The developed models take into account the contributions of the power electronic converters, detailed controls, and their transient impact on the conventional generation and transmission systems.

A framework for analyzing the impact of increasing PV penetration on generation and transmission networks while considering the responses of conventional generators to changes in solar PV output power was proposed. Contrary to traditional

approaches in which it is assumed that generation can always match demand, this framework employs a detailed minute-to-minute (M-M) dispatch model capable of capturing the impact of renewable intermittency and estimating the over- and under-generation dispatch scenarios due to PV volatility and surplus generation.

A dynamic IBR resource module with a variable capacity that can be employed for multiple systems including solar PV, wind, and battery system was proposed. This module may be regarded as a hybrid system that combines the comprehensive benefits of detailed IBR models with the reduced computational requirement of the average models.

Opposed to the rapid pulse discharge cycles employed in traditional cell parameter estimation approaches, a new charge/discharge cycle for identifying the equivalent circuit parameters for utility-scale battery systems using equipment readily available at installation sites without the need for laboratory setups is proposed. Furthermore, the performance of utility-scale equivalent circuit models developed at multiple sub-component levels, i.e. at the rack, module, and cell levels were compared and evaluated.

A solar PV and BESS configuration for recuperating PV energy that will otherwise be curtailed or "clipped" was proposed. This configuration utilizes a single dc-dc converter capable of simultaneously operating as a battery charge controller and a maximum power point tracking device. In addition to improving the overall system capacity factor, increasing the conversion efficiencies, and ensuring MPPT stability, the proposed configuration offers a simple solution for adding energy storage to existing PV installations.

1.4 Publications

The main elements of this dissertation have been peer-reviewed and published in the following journal papers:

- Akeyo, O., Rallabandi, V., Jewell, N., Patrick, A., and Ionel, D. M., "Parameter Identification for Cells, Modules, Racks, and Battery for Utility-Scale Energy Storage Systems", in IEEE Access, Vol. 8, doi: 10.1109/ACCESS.2020.3039198 (2020) [42]

- Akeyo, O., Rallabandi, V., Jewell, N., and Ionel, D. M., "The Design and Analysis of Large Solar PV Farm Configurations with DC Connected Battery Systems", IEEE Transactions on Industry Applications, Vol. 56, No. 2, doi: 10.1109/TIA.2020.2969102, pp. 1-10 (2020) [43]

- Rallabandi, V., Akeyo, O. M., Jewell, N., and Ionel, D. M., "Incorporating Battery Energy Storage Systems into Multi-MW Grid Connected PV Systems", IEEE Transactions on Industry Applications, Vol. 55, No. 1, pp. 638-647, doi: 10.1109/TIA.2018.2864696 (2019) [44] - *IEEE Industry Application Society (IAS) 2020 RESCCS Best Paper Award: Third Prize*

An additional number of seven peer-reviewed conference proceedings papers have been published and are listed in the following:

- Akeyo, O. M., Patrick, A., and Ionel, D. M., "Impact of High Renewable Energy Penetration on a Benchmark Transmission System", Proceedings, IEEE PESGM 2020, Montreal, Canada (Aug 2020) [45]

- Akeyo, O., Rallabandi, V., Jewell, N., and Ionel, D. M., "Measurement and Estimation of the Equivalent Circuit Parameters for Multi-MW Battery Systems", Proceedings, IEEE ECCE 2019, Baltimore, MD, USA, 2019, doi: 10.1109/ECCE.2019.8912233, pp. 2499-2504 (Oct 2019) [46]

- Akeyo, O. M., Rallabandi, V., Jewell, N., and Ionel, D. M., "Modeling and Simulation of a Utility-Scale Battery Energy Storage System", Proceedings, IEEE PESGM 2019, Atlanta, GA, doi: 10.1109/PESGM40551.2019.8974042, pp. 1-5 (Aug 2019) [47]

- Akeyo, O. M., Gong, H., Rallabandi, V., Jewell, N., and Ionel, D. M., "Power Utility Tests for Multi-MW High Energy Batteries", Proceedings, IEEE ICRERA 2018, Paris, France, pp. 2504-2509, doi:10.1109/ICRERA.2018.8566920 (Oct 2018) [48]

- Akeyo, O. M., Rallabandi, V., Jewell, N., and Ionel, D. M., "Improving the Capacity Factor and Stability of Multi-MW Grid-Connected PV Systems with Results from a 1MW/2MWh Battery Demonstrator", Proceedings, IEEE ECCE 2018, Portland, OR, pp. 2504-2509, doi: 10.1109/ECCE.2018.8558253 (Sep 2018) [49]

- Akeyo, O. M., Rallabandi, V., and Ionel, D. M., "Multi-MW Solar PV Pumping System with Capacity Modulation and Battery Voltage Support", Proceedings, IEEE ICRERA 2017, San Diego, CA, doi: 10.1109/ICRERA.2017.8191097, pp. 423-428 (Nov 2017)[50]

- Rallabandi, V., Akeyo, O. M., and Ionel, D. M.,"Modeling of a Multi-megawatt Grid Connected PV System with Integrated Batteries", Proceedings, IEEE ICRERA 2016, doi: 10.1109/ICRERA.2016.7884512, pp. 1146-1151 (Nov 2016) - *Best Poster/Paper Award at the 2016 IEEE ICRERA* [51]

Two other papers have been completed, one for journal and one for conference proceedings, and are currently under review:

- Akeyo, O. M., Patrick, A., and Ionel, D. M., "Minute-to-minute economic dispatch model and transmission framework for estimation solar PV hosting capacity", Electric Power Components and Systems (2021) - *under review*
- Akeyo, O. M., Bankes, G., Patrick, A., and Ionel, D. M., "Utility-Scale Solar PV and Battery Energy Storage Penetration Study on a Proposed Transmission Benchmark System", IEEE Power and Energy Society General Meeting (2021) - *under review*

Chapter 2

Incorporating Battery Energy Storage Systems into Multi-MW Grid Connected PV Systems

2.1 Introduction

The focus on grid resilient has led to the increasing penetration of renewable energy resources including solar photovoltaics (PV) and wind power plants. Among these renewable sources, solar PV plants are the fastest growing and the easiest to implement in small scale. Multi-MW solar PV farms pose multiple threats to the operation of the traditional grid due to their intermittent nature. However, some of the challenges could be in principle mitigated with the integration of battery energy storage systems (BESS).

Some of the recent studies related to solar PV systems have been focused on their operation and controls [52, 53]. The techniques for maximum power point tracking (MPPT) algorithm were recently reviewed in [54, 55], and some of the recommended power electronics topologies for PV systems integrated with BESS have been analyzed in [56]. Battery energy storage system are typical sized based on the configuration

for PV integration and application [57]. The methodology for sizing BESS connected to the dc link of a PV system was proposed in [43]

Inverter based resources such as BESS have the ability to almost instantaneously respond to electricity demand. Hence, in addition to supporting the PV operation, BESS may also be employed for grid ancillary services including frequency response, reactive power support, peak shaving and load shifting [58].

This study reviews the configurations for solar PV system incorporated with BESS, evaluates the impact of large solar PV penetration on a transmission network and propose a methodology for sizing batteries to make solar PV dispatchable. This study is an expanded follow-up to the study in [51]. Additional contributions include the review of dc-dc converter in PV systems, methodologies for the inverter control and the systematic study to analyze the impact of PV and BESS on the power system.

The following sections of this chapter is focused on the configurations for PV and BESS and the analysis of the experimental system. The review of multiple controls for grid connected inverters and evaluates the benefits of integrating dc-dc converters in the PV systems for MPPT are also included in this chapter. A comparative study evaluating the operation of both the simulated and field implemented PV systems during periods of excess irradiance was presented. The solar PV transient responses and BESS applications for supporting PV and grid operations are also presented. Additionally, a systematic BESS sizing approach for a 10MW PV to be dispactable is also included in this chapter.

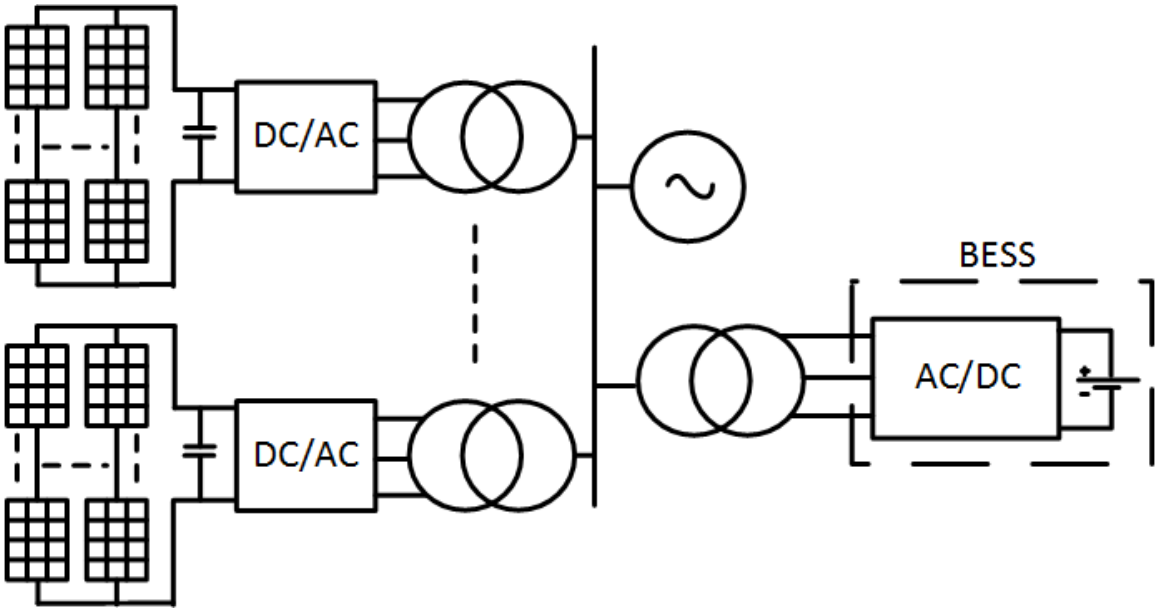

Figure 2.1: Schematic of a practical field implementation for a multi-MW grid tied solar PV system including several modular units connected in parallel. The BESS comprises a battery unit and its associated inverter.

2.2 PV system configuration and control

Due to limited power rating of power electronics devices, multi-MW PV farms are typically divided into multiple section with independent power conversion systems. The field implemented solar PV setup employed in this study consist of ten operational PV sections. Each section includes a PV array rated for 1.4MW and a 1MVA inverters system. In other to mitigate some of the challenges of the PV system and improve the overall grid performance, the setup also includes an ac connected 1MW/2MWh battery energy storage system as illustrated in Fig. 2.2.

In order to analyze and evaluate the performance of the PV and BESS, representative electromagnetic transient (EMT) models were developed in PSCAD^{TM}/EMTDC^{TM},

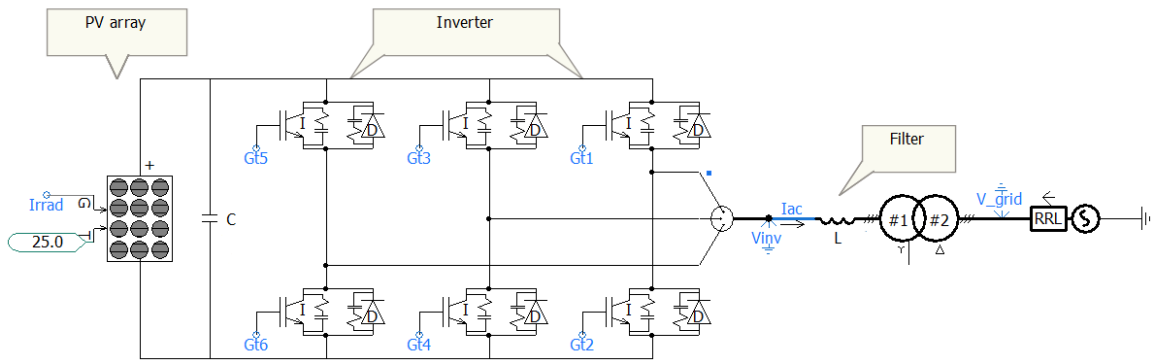

Figure 2.2: Power circuit diagram in the PSCAD software for a module comprising a PV array, a 2-level inverter, filter, and a transformer connected to the power grid. Traditional PV systems typically include a dc-dc converter between the PV array and the inverter and use this for MPPT control. In the current implementation, the real power output of the inverter is directly controlled in order to achieve MPPT for the PV array.

which is a software typically employed for transient studies. The PV cell in the software is developed based on the Norton equivalent circuit model, which includes a current source connected in parallel to a diode along with shunt and series resistances. The output current of the PV cell, i, is expressed as:

$$i = i_g - i_o \left[\exp\left(\frac{V + iR_{sr}}{nKT_c/q} \right) - 1 \right] - \left(\frac{V + iR_{sr}}{R_{sh}} \right), \tag{2.1}$$

where, i_g represents the component of cell current due to photons; i_o, the saturation current; K, the Boltzmann constant (K = 1.38 $\times$ $10^{-23} j/K$); q, the electron charge (q = 1.6x10^{-19}C); V, the output voltage; T_c, the cell temperature; R_{sh}, the shunt resistance and R_{sr}, the series resistance. The photo-current i_g of a PV cell depends on the amount of solar irradiance incident on the PV cell and its temperature. The

photo-current relationship with solar irradiance and cell temperature is expressed as:

$$i_g = i_{scR} \frac{G}{G_R} \left[1 + \alpha_T \left(T_c - T_{cR}\right)\right], \tag{2.2}$$

where, i_{scR} is the short circuit current at the reference solar radiation and temperature; G_R, the reference solar radiation; T_{cR}, the reference temperature; G, the solar irradiance at which current is being calculated; α_T, the temperature coefficient of the photo-current, usually 0.0017A/K for Si solar cells and T_c, the cell temperature. At standard test conditions, G_R is 1000W/m^2 and T_{cR}, 25°C. Other standard test conditions include the photovoltaic for utility scale application test condition (PTC) with G_R and T_{cR} set at 1000W/m^2 and 20°C respectively.

The saturation current, also known as the "dark-current", is expressed as a function of the cell temperature,

$$i_o = i_{oR} \left(\frac{T_c^3}{T_{cR}^3}\right) \exp\left[\left(\frac{1}{T_{cR}} - \frac{1}{T_c}\right) \frac{qe_g}{nk}\right], \tag{2.3}$$

where, i_{oR} is the saturation current at the reference temperature; e_g, the band gap energy of the solar cell material and n, the diode ideal factor, typically 1.3 for silicon solar cells.

Power conditioning devices for PV systems are typically specified for a limited voltage and current range. Hence, PV modules are typically connected in series and parallel to meet power conditioning devices limitation. For the field implemented system employed for the study, each section includes 19 modules connected in series and 236 module strings in parallel. Each module was developed based on manufacturer specified data. For this PV array, the modules are rated for 46.75V open circuit

Table 2.1: PV cell and array module specifications.

Parameters	**Value**
Cell open circuit voltage(V)	1.17
Cell short circuit current (A)	4.01
Cell saturation current (kA)	1e-12
Temperature coefficient of i_g	0.001
Series resistance per cell (Ω)	0.02
Shunt resistance per cell (Ω)	1000
Module open circuit voltage(V)	46.75
Module short circuit current(A)	9.02
Voltage at MPP (V)	37.40
Current at MPP (A)	8.50
Maximum power(W)	316.50

voltage and 9.02A short circuit current. The details of the simulated PV array and field implemented system are presented in Table. 5.1.

The maximum power a PV array can deliver varies based on the available solar irradiance and the cell temperature. The output power also varies based on the array terminal voltage, hence, the need to integrate an algorithm to ensure the PV array operates at the voltage corresponding to its maximum power, maximum power point (MPP). There are multiple algorithms for estimating the voltage corresponding to PV array MPP, including the commonly used incremental conductance (InC) and pertub and observe (P&O) methods. For the P&O method, the terminal voltage and current for the PV array is measured recorded at the initial state. In order to estimate the voltage corresponding to the MPP reference, the PV array terminal voltage is slightly disturbed and the changes in its output current is used to estimate the direction for approach MPP voltage reference. This algorithm can approach its MPP faster with larger perturbation. However, larger perturbations lead to reduced algorithm accuracy and inefficient dynamic response.

Additionally, the inability of the P&O to settle at the voltage corresponding to the PV array MPP further introduces oscillations at steady state operation. The alternative InC method which was developed to address the shortcomings of the P&O continuously monitors the power-voltage characteristics of the PV array was employed in this study. The algorithm introduces a reduced amount of oscillations to the system in addition to improving the accuracy of the algorithm during transient conditions [59].

2.3 Grid-connected inverters

The methodology for ensuring PV array operates at the voltage corresponding to its MPP varies depending on the configuration of its system. Solar PV systems of relatively lower capacities, MPPT may be performed at the module or string level without significant cost implications. For increased reliability and lower cost, multi-MW PV system typically perform MPPT at array levels.

In some cases, the PV arrays are connected through dc-dc converters and inverters in order to make sure the array terminal voltage is regulated within the inverter operation range. In such two-level inverter configuration, the dc-dc converter is typically employed for MPPT and to boost the terminal voltage of the PV array to a reference value suitable for grid integration with the inverter. Also, two-stage solar PV systems introduces an additional benefit for dc-coupled energy storage system integration and ensures such storage systems may be integrated with minimal changes to the PV operation [50].

The PV system developed in this study is based on the LG&E ad KU E.W. Brown

system, which includes multiple inverters used for MPPT and power conversion. The field implemented PV system features ten Freesun FS1050CU-24299T 2-level inverters, each rated for 1MW with input voltage ranging between 700-1000V. The MPPT voltage window for this inverter varies based on the operation condition, where the inverter is capable of operation between 642V-820V at 50°C and 712V-820V at 25°C. This inverter also includes the IEEE 1547 utility interconnect with interactive control functions, has a full range power factor and the ability to curtail its output power at 0.1% steps.

This approach employs a decoupled voltage source inverter control in which the direct and quadrature voltage and current components are regulated to vary its output power. When the direct axis of the reference frame is aligned along the grid voltage, the direct axis component is equal to the magnitude of the grid voltage and its quadrature component is equal to zero. For the employed inverter, the reference components are expressed as:

$$V_d^* = -V_d' + \left(V_{gd} + \omega_e \, L_g \, i_q\right), \tag{2.4}$$

$$V_q^* = -V_q' + \left(V_{gd} + \omega_e \, L_g \, i_d\right), \tag{2.5}$$

where,

$$V_d' = R_g \, i_d + L_g \frac{\mathrm{d}i_d}{\mathrm{d}t}, \tag{2.6}$$

$$V_q' = R_g \, i_q + L_g \frac{\mathrm{d}i_q}{\mathrm{d}t}. \tag{2.7}$$

V_{gd} and V_{gq}, the direct and quadratic components of the grid voltage and V_d^* and V_q^* the corresponding references, i_d and i_q are driven by the inverter direct and quadrature voltages components and the L_g and R_g represent the grid resistance and inductance, respectively.

The output power of the inverter are expressed as:

$$P_g = \frac{3}{2} V_{gd} i_d, \tag{2.8}$$

$$Q_g = -\frac{3}{2} V_{gq} i_q, \tag{2.9}$$

where, P_g and Q_g are the real and reactive powers respectively. The inverter varies its direct axis current components in order to regulate its real power output and ensures the PV array terminal voltage is maintained at its MPP reference value. In this approach, the reactive current component, I_q^*, is maintained at zero in this study for unity power factor operation of the PV inverter, however, in principle, its value can be derived from an outer reactive power controller, as shown in Fig. 2.3.

In order to maintain the currents at their set references and ensure grid synchronization, grid voltage oriented control, illustrated in Fig. 2.4, is used. A phase locked loop (PPL) block generates, from grid voltage measurements, the phase angle employed in reference frame transformations to decouple the 3-phase inverter currents into direct and quadrature components, which can be independently tuned to control real and reactive power flow into the grid, respectively.

Simulation studies were conducted on the system of Fig. 2.2, which employs the inverter for both MPPT and dc-ac conversion. Its performance under different

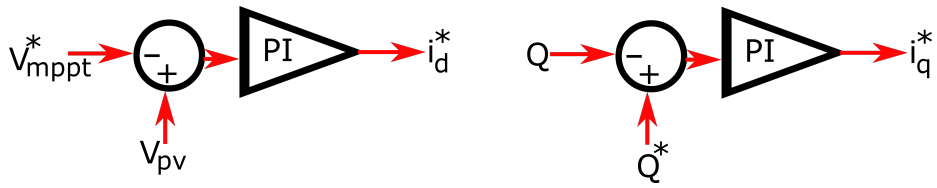

Figure 2.3: PV inverter controls for reference current components. Zero current control for i_q^* ensures unity power factor operation.

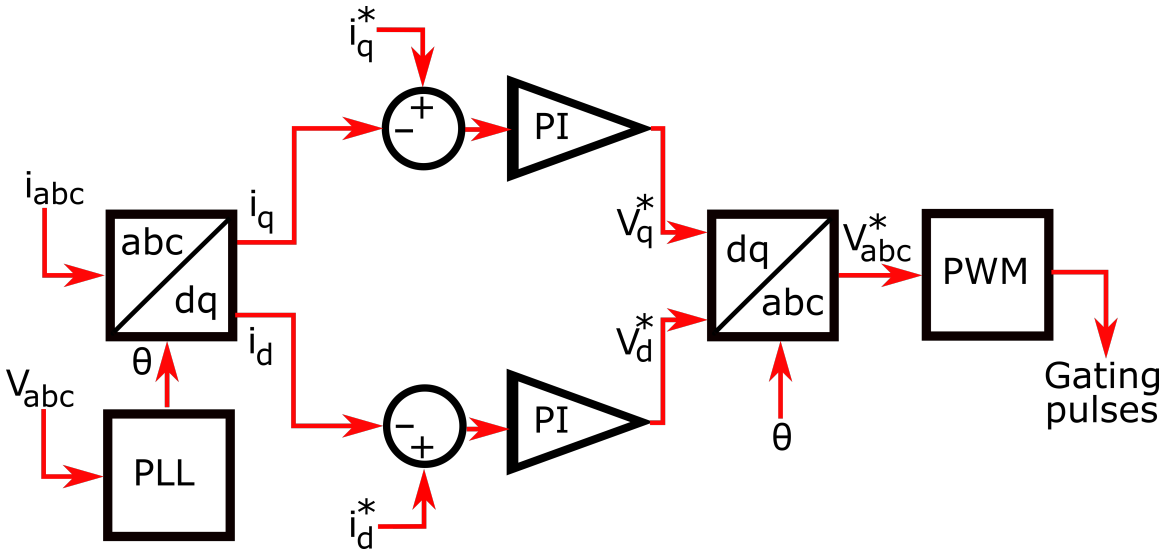

Figure 2.4: Inverter control in order to ensure decoupled regulation of active and reactive power components. The grid voltage-oriented reference frame employed for transformations uses the phase angle provided by instantaneous voltage measurements.

conditions and sudden changes of irradiance was compared with a 2-stage system, which includes a dc-dc converter for MPPT and an inverter for grid interfacing. It was observed that the power outputs of the two systems are very closely comparable (Fig. 2.5).

Using the grid connected inverter for MPPT helps to eliminate the additional cost of acquiring a dc-dc converter rated for the entire PV array power as well as the loss within the converter. Since irradiance and temperature variations lead to little change in the MPP, and thus the dc-bus voltage, normal operation of the inverter is unaffected by varying conditions. Cases for which the inverter cannot be configured in order to control its dc-link voltage, previously studied by the authors [50], or alternatively, situations with the PV array terminal voltage below requirements, may necessitate an intermediate dc-dc stage.

2.4 Constant power generation

Solar PV plants nameplate dc rating are typically not equal to the ac ratings for multiple reasons including capacity factor requirements by regulatory bodies and the utilization factor of the inverter. Solar PV power plant inverter load ratio, ILR, which is the dc to ac ratio varies with the capacity and application. The example system employed has a 1.4 ILR, where each section is rated for 1.4MW$_{dc}$ with 1MVA inverter systems. Since the inverter cannot output power exceeding its rated capacity, during periods of excess irradiance, the inverter will raise the operating voltage of the PV array deviate it from its MPP reference towards an output corresponding to its rated capacity.

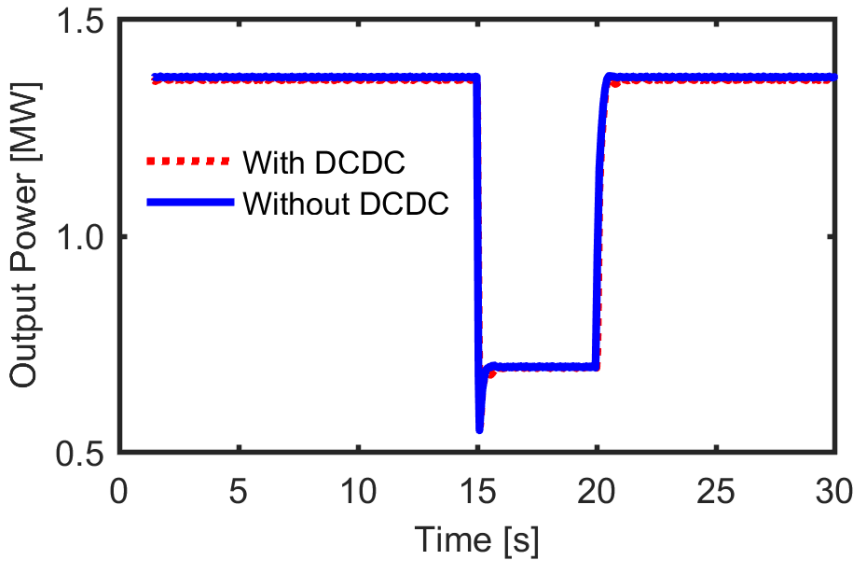

Figure 2.5: Variation of the power fed to the grid due to shading of the PV system leading to a drop in irradiance from 1000W/m^2 to 500W/m^2. The output powers from systems with and without a dc-dc converter between the PV array and inverter are virtually the same, demonstrating that MPPT is possible for different conditions, even if the dc-dc converter is absent.

In order to develop a representative electromagnetic transient (EMT) model for the field implemented 10MW$_{dc}$/14MW$_{ac}$ system, irradiance data were retrieved from the two weather stations distributed across the 45 acres field. This solar farm includes more that 40,000 fixed tilt solar panels and the average measured irradiance (I_{exp}) from the two weather stations for an example clear was used to represent the irradiance on the entire system in PSCAD. The operation of the developed model and control was evaluated for the example day over a PSCAD accelerated time-scale, such that 1s simulation time is equivalent to 24mins. The results show similar output power variation for both experimental (P_{exp}) and simulated (P_{sim}) models (Fig. 2.6). A partial mismatch between the two models at later periods of the day, which may be due to the cell temperature build up in the field implementation was observed.

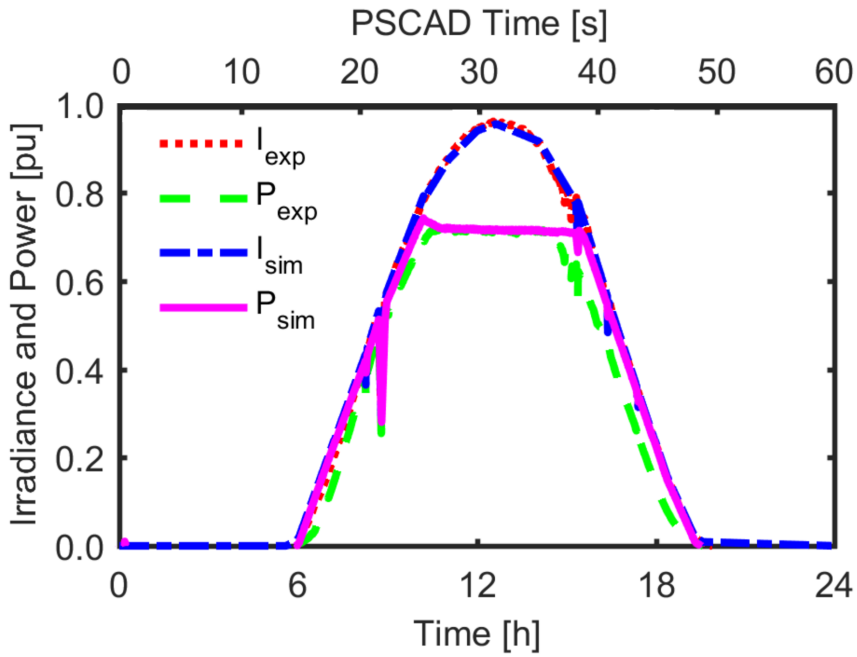

Figure 2.6: Experimental and simulated irradiance and PV system output power during a sunny day with sporadic shading. The capacity of the PV plant is purposely limited, i.e. "clipped", to 0.71 p.u. The behavior of the system is simulated by applying a linearly accelerated time frame in PSCAD.

The PV inverter was controlled to regulate PV array terminal voltage at its MPP reference. In order to ensure the inverter operates within its rated capacity, I_d^* is limited to 2.1kA which in this case corresponds to the rated capacity of the inverter (Fig. 2.7). Hence, during periods of surplus irradiance when the measured irradiance exceeds approximately 0.7pu, as the inverter I_d^* is reaches its saturation limits, the PV array terminal voltage further deviates from its MPP reference and towards open-circuit as illustrated in Fig. 2.8. An intermediate dc-dc converter may be employed to ensure stable operation during curtailment [60]. The proposed model can be used to evaluate the harmonics contribution of the solar PV plant. Harmonics introduced due to circulating current from the multiple inverter sections and the power electronic devices operation can isolated and analyzed. It is important to recognize

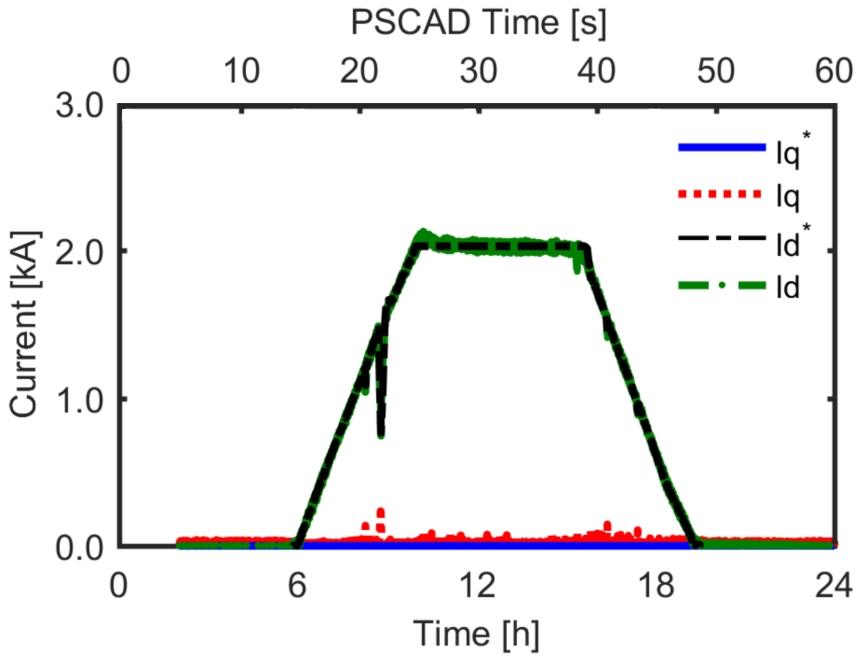

Figure 2.7: Current components for the PV inverter. Constant power generation at mid-day is achieved by imposing saturation limits on the outer dc-bus voltage controllers providing the d-axis current reference.

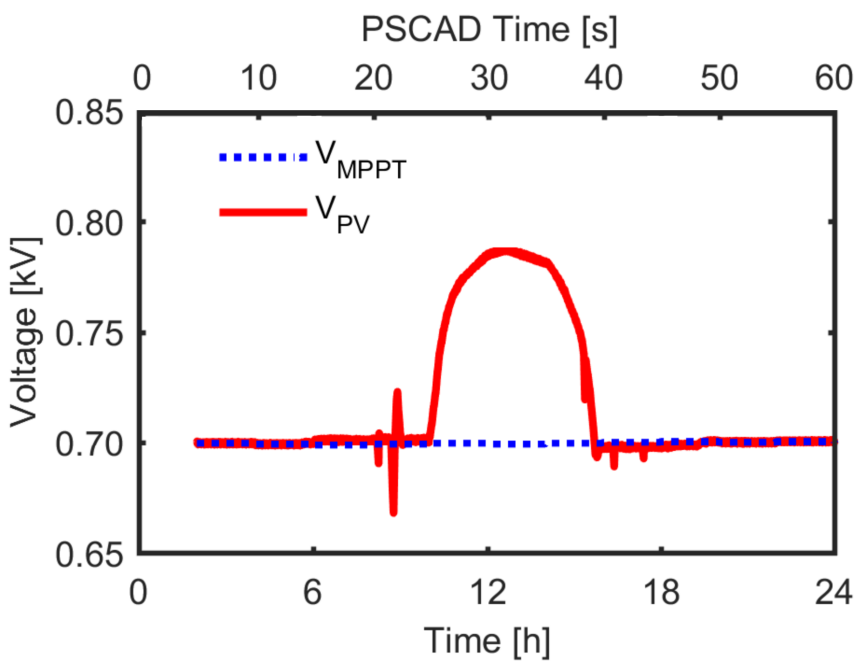

Figure 2.8: PV array terminal voltage and its set point determined by the MPPT controller. The inverter is operated in constant power mode at 0.71 p.u. when large irradiance values would yield higher PV power output.

that large filter are typically required for two-level inverters similar to the proposed model and multi-level inverters may be employed to ensure more sinusoidal output power components and reduced the filter size [61].

2.5 Battery energy storage systems applications

The intermittent behavior of renewable energy limits their large scale grid integration. The output power of a PV system varies with change in the level of irradiance, which is generally not constant throughout the day. Batteries can be used to improve power dispatchability by storing excess energy during peak irradiance and discharging to the grid when the power from the solar energy source is small.

The 1MW/2MWh energy storage system at LG&E KU includes a Li-ion battery bank stored in two 6.06x2.44x2.6m shipping containers. The battery modules include 28-cells, with 17-modules stacked per rack such that each container has 10-racks. In order to maintain the battery temperature at the required value, the containers are equipped with heating and cooling systems, which maybe energized from the battery.

Each of the LG Chem M48126P3b1 ESS battery modules has a nominal output voltage of 51.8V and a capacity of 126Ah. These modules are connected in series and parallel so that the terminal voltage from each container is about 950Vdc and it is directly connected to the Dynapower CPS-1000 1MW inverter. This energy storage inverter can be controlled to perform various functions some of which include; the Autonomous Frequency-Watt Mode, where the system charges or discharges depending on the difference between the measured and reference grid frequencies. The inverter can also be controlled for power smoothing, which instructs the system on

dynamically modifying the Watt input or output in response to fast changes in the commanded power.

In the studied system, the BESS includes a battery and an inverter, which is controlled using a grid voltage oriented reference frame, such that the d-axis component of the current controls the active power, and the q-axis component, the reactive power. The d-axis current component is derived from an outer power loop, as described in the following,

$$i_d^* = (P_{ref}^* - P_{pv} - P_{batt}) * \left(K_{p1} + \frac{K_{i1}}{s}\right), \tag{2.10}$$

The controller regulates the battery power such that the sum of the battery and PV powers follows a desired profile, determined, for example from a power smoothing algorithm (Fig. 2.9). The reactive current is maintained at zero as the BESS system operates in this study, at unity power factor, though in principle, non-zero values can also be used.

2.5.1 PV power smoothing

Smoothing of PV power is generally accomplished by controlling the BESS to track the difference between instantaneous and filtered PV powers for which moving average (MA) or low pass filters are employed. With MA filters, the smoothed or filtered power output variation is found as,

$$P_o[i] = P_{pv}[i] - \frac{1}{n}\sum_{j=0}^{n-1} P_{pv}[i+j], \tag{2.11}$$

where, P_o is the net power to be supplied by the PV and BESS; i, the sampled point; P_{pv}, the power of the PV system and n, the number of points in the average.

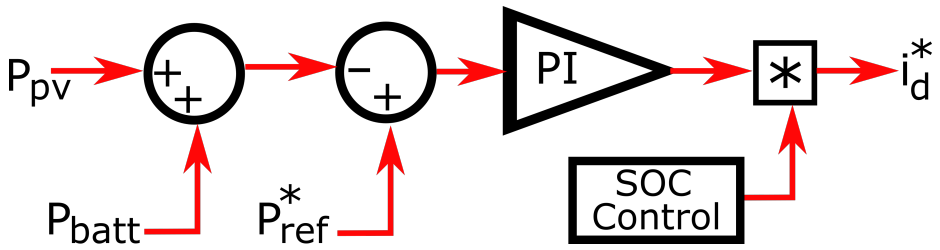

Figure 2.9: Control strategy for the BESS ensuring that the PV and battery output powers sum up to a predefined reference value, which is determined depending on the net power to be supplied. The BESS inverter is controlled in order to supply the commanded currents using a grid voltage-oriented reference frame and PWM (not shown). The set power is supplied to the grid provided that the BESS state of charge is within the prescribed limits.

The sum of the powers supplied by the battery and PV system is the smoothed output. In other words, the battery absorbs and supplies the "power ripple". The power rating of the battery may be found as the maximum difference between the PV and the net powers. The battery, net and PV powers for an irradiance variation on a cloudy day in the LG& E and KU E.W. Brown facility are shown in Fig. 2.10. It is observed that the battery needs to supply approximately 0.5 p.u. of the power, but for very short times, indicating that the BESS is rated relatively high in terms of power, although a relatively small energy rating may be sufficient for this purpose.

The performance of the PV and BESS system when connected to an IEEE-14 bus system, which represents a portion of the American electric power system in the Midwestern US and is widely accepted by researchers to implement new ideas and concepts in power system engineering related topics such as short circuit analysis, load flow studies, and grid interconnection problems [62] is studied. This system consists of 14 buses, 11 loads and 5 generators of which 3 are synchronous condensers and one slack bus. The Manitoba HVDC research center model of the IEEE 14 bus system in PSCAD^{TM}/EMTDC^{TM} was adopted in this study [63].

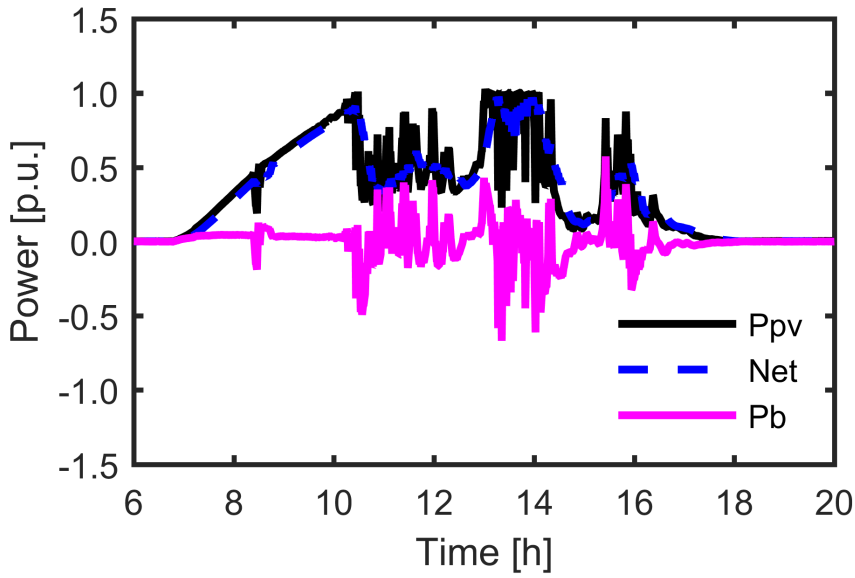

Figure 2.10: Power from the PV system using experimental data for a cloudy day. The net power is smoothed using a moving average filter with the BESS controlled in order to track the difference between the net and PV powers.

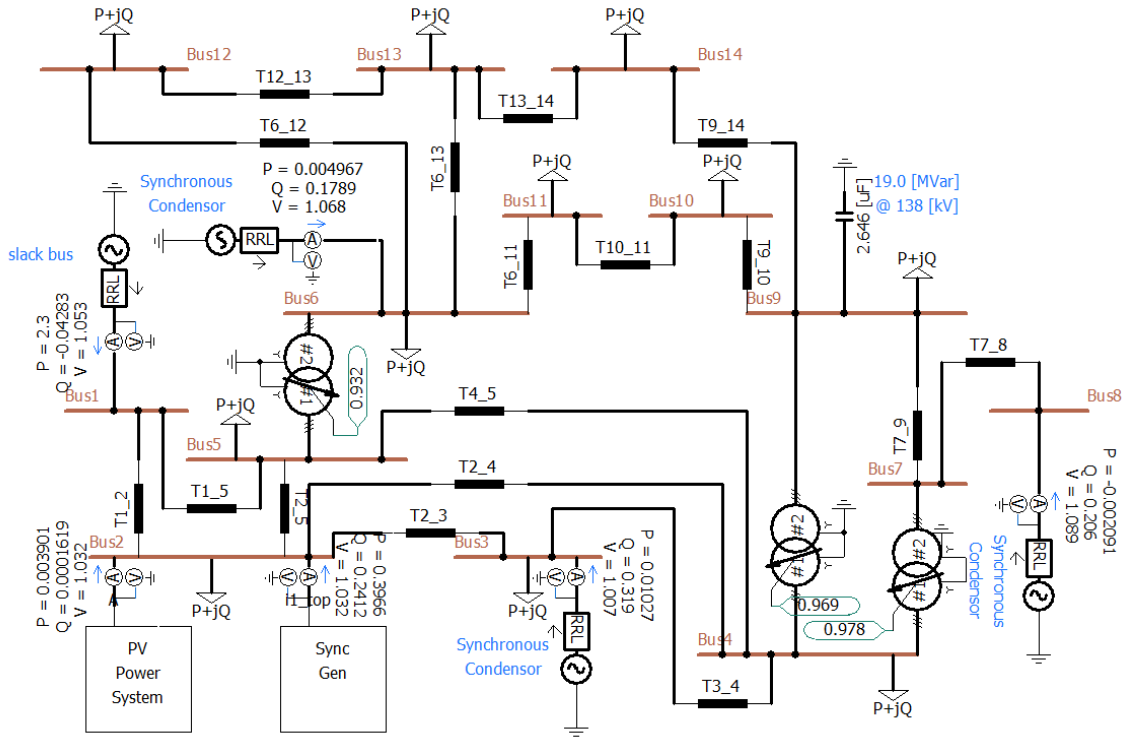

Figure 2.11: Modified IEEE 14 bus system with the PV system incorporating a BESS supplying part of the power at Bus no. 2

In the modified IEEE 14 bus system, the 3-phase voltage supply at bus no. 2 is replaced with the designed 10MW PV system connected in parallel with a 100MVA synchronous generator as shown in Fig. 2.11. With this configuration, the generator, typically operated below its rating, steps up its output power when the PV system integrated with BESS is unavailable due to shading and battery state of charge (SOC) constraints. For the purpose of the study it is considered that the battery's MW rating is enough to provide all of the power, in case of shading of the PV system. Upto t = 4s, the PV system supplies the power, until it is shaded, when the battery takes over as seen in Fig. 2.12. The battery can supply the deficit power only for a very short duration of time. At 10s simulation time, the battery's SOC falls below minimum, and it stops supplying power, leading to a transient reduction in the bus frequency before the adjacent synchronous generator steps up its real power output to supply the power deficit from the PV (Fig. 2.13). In this case, the synchronous generator can supply without significant effect on its operation, the power deficit since it is rated for 100MVA while the PV system is rated for 10MW.

2.5.2 Frequency regulation

Power smoothing, and compensating for the effect of clouds include short term power supply applications of energy storage systems. Another such application is primary frequency regulation, which involves the supply of power for a short duration of time, up to 30s [64, 65]. Power supply and load variations are leading causes of frequency variations. An increase in irradiance or decrease in connected loads leads to higher grid frequency and likewise, lower irradiance or peak load demands lead to

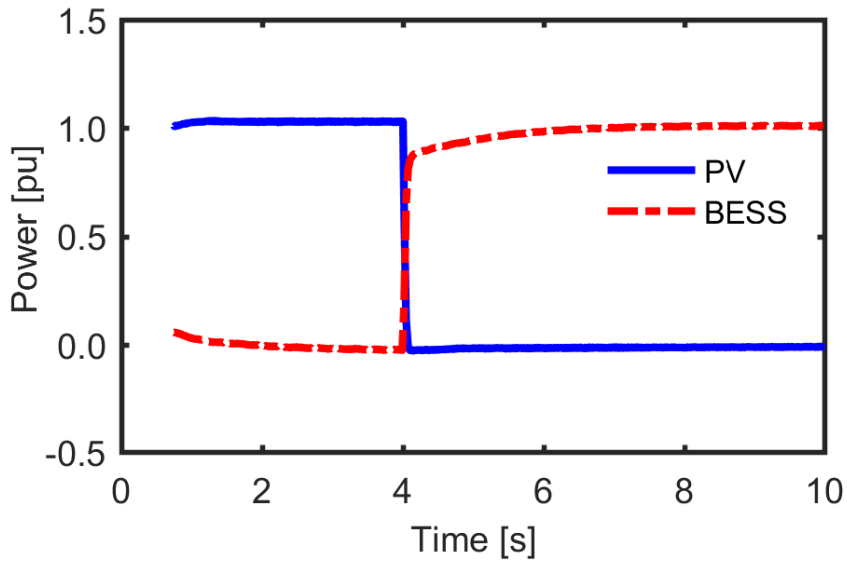

Figure 2.12: Transient simulation for a case study in which at t = 4s the PV arrays are completely shaded and its power output is completely compensated with very fast response by the BESS.

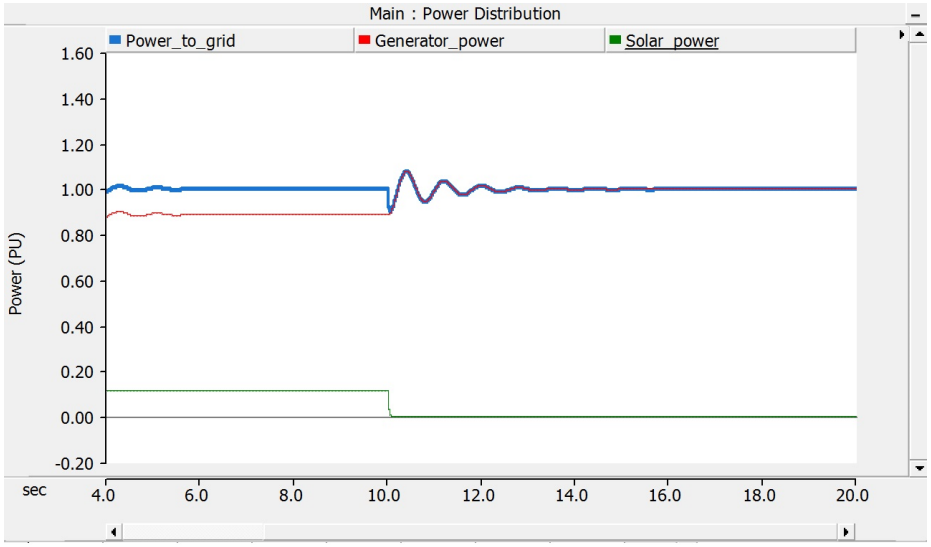

Figure 2.13: Transient simulation for the case study illustrating the effect of power loss from both the PV *and* the BESS t = 10s. Until this instance, power at bus no. 2 was supplied by the combined solar power system with PV and BESS and the synchronous generator. Following the reduction in battery SOC below its minimum value, the synchronous generator supplies the power deficit. Disturbances in power and frequency are observed before the system returns to normal steady state operation.

(a)

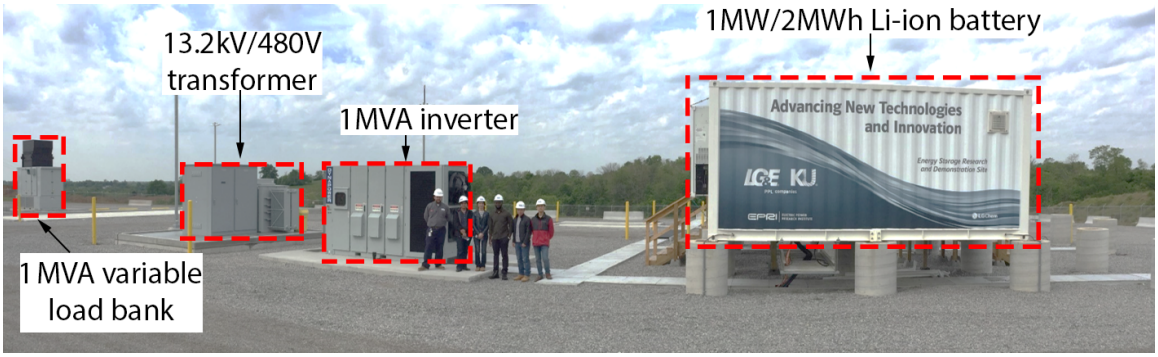

(b)

Figure 2.14: The LG&E and KU 10MW universal solar facility on the E. W. Brown power plant site, which also includes GW rated coal and natural gas fired generators (a) Containers for the 1MW 2MWh battery demonstrator (one shown on the right side of the figure with a second container obscured behind it), BESS inverter (center) and 1MW controllable load (left). The research site also includes a SCADA facility, which is not shown (b).

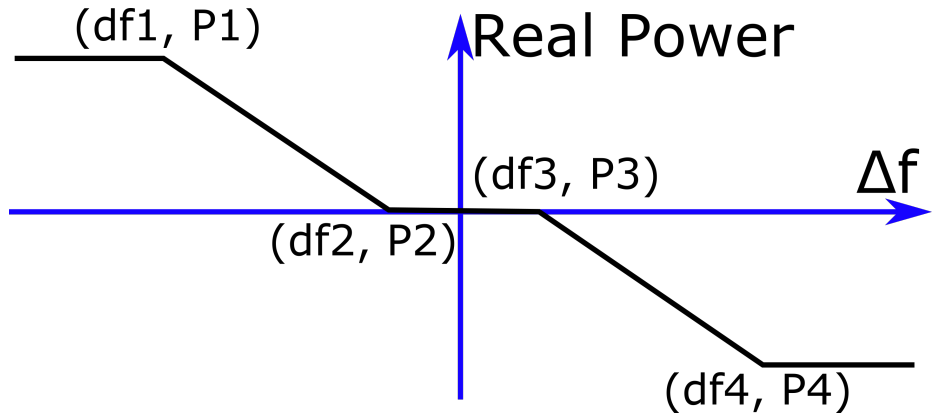

Figure 2.15: Droop characteristics for BESS operation with changes in grid frequency. The real power output is limited to the values corresponding to the rated power of the BESS.

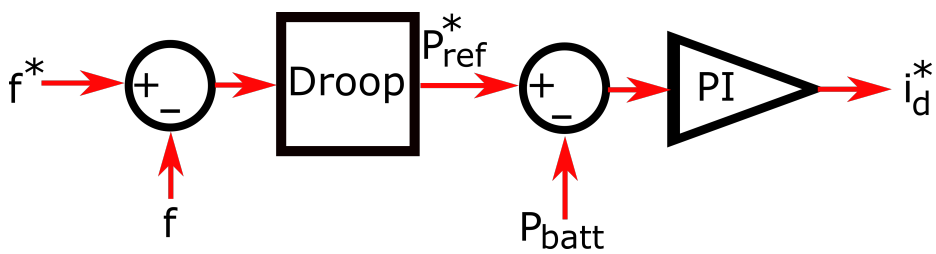

Figure 2.16: BESS control in frequency regulation mode. The active component of the current, i_d^*, is positive and hence the BESS supplies power when the frequency is below the set point, and current reverses for frequency above this value. The BESS output is maintained at zero when the frequency variation is within ± 0.005Hz.

a reduction in grid frequency. Battery energy storage systems can be used to regulate utility frequency such that the battery charges from the grid when its frequency is above the reference and discharges power to the grid when it is below the reference. The relationship between the frequency change (Δf) and power variation (ΔP) is given as,

$$\Delta P = P_{ref} - \beta \Delta f. \tag{2.12}$$

The amount of power required to restore the frequency of the grid to its reference value depends on the area frequency characteristics (β). For this study, this value

is assumed to be constant such that 1MW power is required for a 0.05Hz frequency change, and these droop characteristics, seen in Fig. 2.15, can be used to determine the amount of power required to restore grid frequency based on the frequency deviation. The control system for the BESS uses the difference between the reference frequency (f^*) and the actual frequency (f) to determine the reference real power output (Fig 2.17). In this study, the maximum output of the controller is limited to the power rating of the BESS. The performance of the BESS for frequency regulation was compared with experimental data retrieved from the LG&E and KU E.W. Brown Universal Solar Facility, pictured along with the 1 MW/2MWh battery energy storage system in Fig. 2.14. An accelerated frequency variation similar to the experimental data result was applied to the proposed system. It is observed that the BESS output power is positive when the frequency drops below its reference, and it absorbs power when the frequency exceeds 60 Hz as seen in Fig. 2.18, in line with experimental measurements, which confirms the successful operation of the BESS for frequency regulation.

2.6 Energy storage sizing for dispatchable PV

In principle, energy storage systems (ESS) may be sized in order to provide constant, P_d, dispatchable power to the grid. This can be achieved by charging the ESS when the instantaneous power from the PV system exceeds the set value and discharged when required, as illustrated in Fig. 2.19. The dispatchable power can be

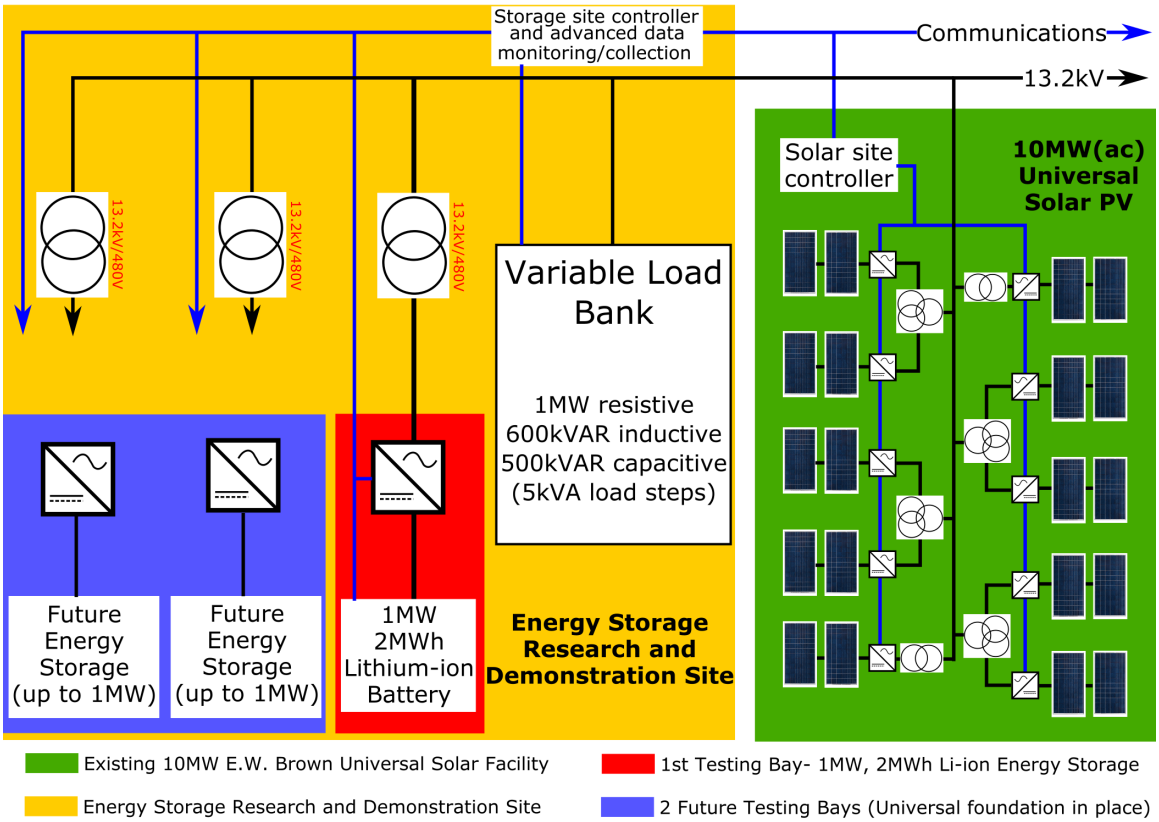

Figure 2.17: Schematic diagram for the experimental setup. Two PV inverters are connected to the grid via a single 3-winding 13,200V/390V transformer. All communication data is synchronized with the local data before being uploaded on a private server.

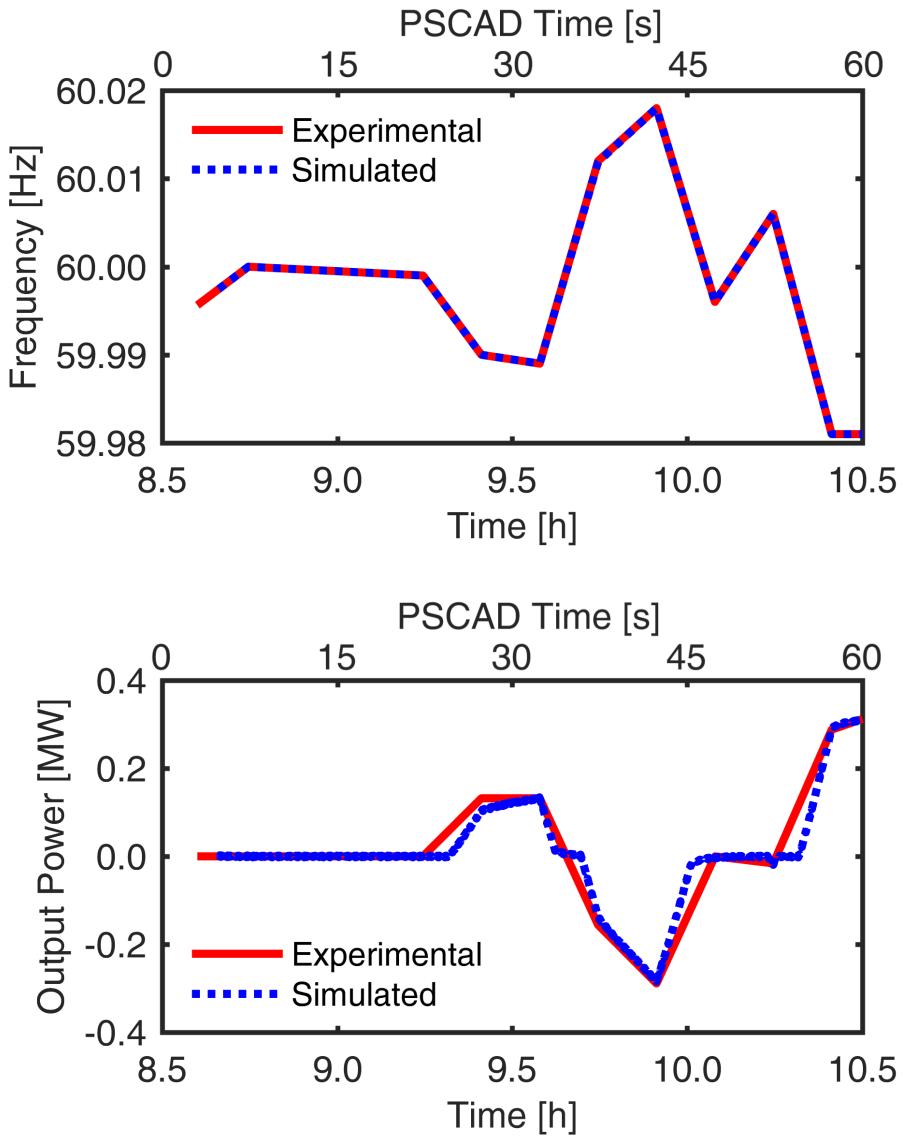

Figure 2.18: (a) Example of grid frequency variation measured over a couple of hours and simulated on a linearly accelerated PSCAD time frame and (b) BESS output power.

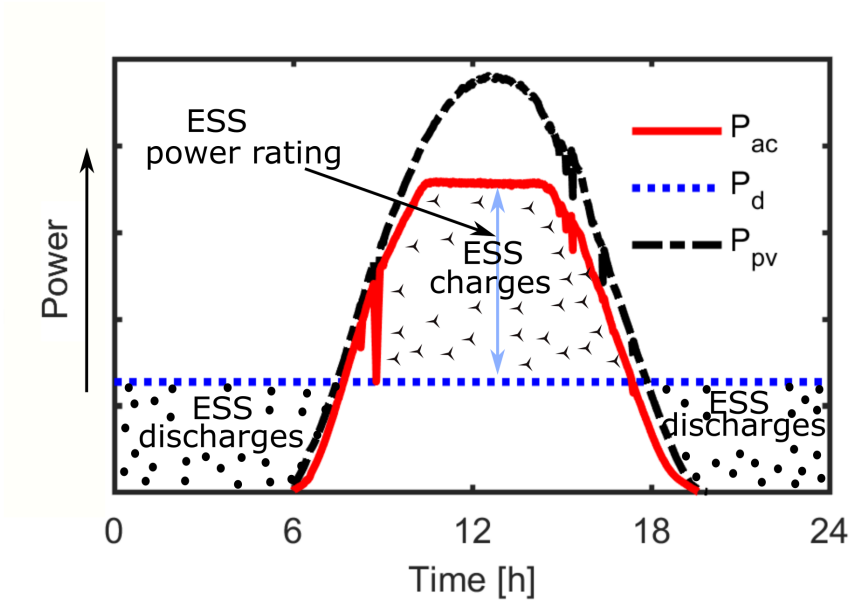

Figure 2.19: Schematic illustration of an energy storage sizing method for 24h constant power, P_d, operation. The ESS charges when the power from the PV system exceeds P_d and discharges otherwise.

defined as

$$P_d = \frac{1}{T}\int_0^T P_{ac} dt, \tag{2.13}$$

where, T is the time period for dispatching, and P_{ac}, the output power from the PV:

$$P_{ac} = \begin{cases} P_{pv} & \text{if } P_{pv} < P_r \\ P_r & \text{otherwise,} \end{cases} \tag{2.14}$$

where P_{pv} is the maximum available PV power and P_r, the rated capacity of the PV plant, which can be "clipped" from the available PV power.

The battery power rating can be obtained as,

$$P_b = P_r - P_d, \tag{2.15}$$

and the energy rating as,

$$E_b = \int_{T_1}^{T_2} (P_{ac} - P_d)\, dt, \tag{2.16}$$

where T_1 is the time corresponding to the positive zero crossing of $P_{ac} - P_d$, and T_2, to the negative zero crossing.

A simple analysis indicates that the larger is the difference between the peak available PV power and the PV plant capacity, the smaller would be the rating for the ESS required to provide constant dispathcable power. Limiting the PV power fed to the grid, an approach that "clips" the power to a constant rated value, could be achieved through a combination of methods, including an MPPT control deviation, as previously discussed, panel reorientation etc, such that the equivalent capcity factor is increased, power fluctuations smoothed out and system reliability enhanced [66].

For the case study considered in this chapter with a rated power of 10MW and a good capacity factor for a sunny day the average power for a 24h period, which could be constantly dispatched would be 3.6MW. Using the simple analysis previously introduced, this would require an ESS with a rating of 6.5MW and 36MWh. The relatively high ratio of energy to power, which is also available to a somewhat lower extent in the 1MW 2MWh demonstrator previously mentioned, is a typical requirement for renewable energy sources that have a relatively low capacity factor. Large ESSS installations employing batteries, such as the 30MW 120MWh Escondido project and the 7.5MW, 30MWh El Cajon development are currently considered in California [67]. As the price of batteries is currently relatively large, BESS technology deployment maybe limited and other ESS systems, such as the innovative pumped hydro solution proposed by Gravity Power [68] may be more feasible.

2.7 Summary

This chapter presents experimental and simulation studies for a 10MW$_{ac}$ grid-connected PV systems, which includes modular section with single-state inverters. The performance of the evaluated configuration and the operation of its MPPT algorithm were validated over multiple irradiance levels. The inverter control was demonstrated to be capable of maintaining the PV array and maximum power point and curtailed excess power during periods of excess irradiance. The study was also establish that a dc-dc converter is not required for effect MPPT, which in turn will lead to substantial cost savings.

The BESS employed in this study was connected to the grid through an independent inverter and transformer. A corresponding equivalent circuit was developed in PSCAD^{TM}/EMTDC^{TM} software environment. The application of the BESS for PV support and other grid ancillary services were demonstrated through two case studies. In order to evaluate the response of the solar PV system during transient shading and to examine how BESS may be employed to mitigate some of the stability challenges due to the solar PV penetration, the solar PV and BESS were connected to a modified IEEE 14 bus system. The results of the study indicate that the BESS when adequately sized is capable of reducing voltage drop due to solar PV intermittency.

The operation of the simulated and field implemented BESS in autonomous frequency response mode was also evaluated. In this mode, the BESS were regulated to absorb real power from the grid when its frequency exceed the reference value and

vice versa. Similar output power response from both 1MW 2MWh battery demonstrator models were recorded when subjected to identical frequency variations. This chapter also proposes a systematic sizing approach to develop a dispatchable solar PV plant with constant power throughout the day. The outcome of the study further emphasize that a relatively high BESS will be required to ensure constant power from a PV plant.

Chapter 3

Study of Renewable Energy Penetration on Generation and Transmission System

3.1 Introduction

Renewable energy resources are rapidly becoming an integral part of electricity generation portfolios around the world due to declining costs, government subsidies, and corporate sustainability goals. Large renewable installations on a transmission network may have potential impacts on the delivered power quality and reliability, including voltage and frequency variations, increased system losses, and higher wear of protection equipment [1]. Estimating the maximum hosting capacity of a transmission network may be used to determine the highest renewable penetration the system can handle without significant violations to the quality of the power delivered and the reliability of the grid.

Most recent literature has been focused on analyzing the impact of intermittent renewables on either generation or transmission systems only [69–72]. In [73], a

methodology for estimating the solar PV hosting capacity based on steady-state circuit violations, without a detailed economic dispatch model was proposed. Typical dispatch models in literature assume generation can always match load or set optimization constraints that are only acceptable for hourly dispatch models with relatively low load variations [74–76]. These hourly dispatch models may not be suitable for capturing the impact of PV systems for practical generation service areas, which record generation imbalance violations over duration as low as 15-minutes.

Furthermore, a substantial portion of literature has been focused on estimating the maximum PV hosting capacity for distributions systems and proposing network configurations that do not consider the contributions of conventional generators [77**?** –79]. However, more than 60% of PV installations in the US are utility-scale setups typically connected to the transmission network [80]. Steady-state and transient analysis of transmission networks were presented in [73, 81], but none of the works considered the variability of the connected loads or present a detailed economic dispatch to capture the responses of the conventional generators.

This research presents a framework for analyzing the impact of increasing PV penetration on both generation and transmission systems. Contrary to conventional approaches dispatching units with substantial intermittent renewable resources with hourly-based dispatch models[82, 83], this approach employs an M-M dispatch model capable of capturing the impact of large solar PV penetration and identifying minute-based periods of generation imbalance due to PV volatility and surplus power. The presented technique is also capable of analyzing the impact of increasing PV system

Table 3.1: Specifications for the generating units in the modified IEEE 12 bus test case studied

Bus no	Type	Rating [MW]	Min gen [MW]	Ramp [MW/min]	Heat rate co-eff. a[10^{-3}]	b	c	Fuel [$/MMBtu]	Aux [$/MWh]
9	NGCC	750	368	10	0.3	7.7	630	176	1.2
10	Coal	640	288	7	4.0	6.4	996	196	1.9
11	NGCT	384	203	9	20.7	2.7	753	176	35.7
12	Hydro	474	-	-	-	-	-	-	-

penetration have on transmission circuits while considering the responses of conventional generators to changes in solar PV power.

The impact of increasing solar PV penetration was analyzed on a modified IEEE 12 bus system [84] with generators, including coal, natural gas combustion turbine (NGCT), natural gas combined cycle (NGCC), and a hydropower plant with practical unit specifications. This study uses generator models developed on data provided by LG&E and KU on operational units to simulate the responses of conventional generators to increasing solar PV penetration (Fig. 3.1). Publicly available one-minute irradiance data for the 10MW PV farm located at the utility's facility was used to model typical variation in solar irradiance [85]. The PV hosting capacity of the example generation and transmission network systems analyzed was estimated based on voltage, thermal, and generator dispatch violations.

3.2 Proposed minute-to-minute economic dispatch model

The real-time changes in load from minute to minute are relatively minimal due to aggregation. However, the volatility of the net demand on conventional thermal

Figure 3.1: The aerial view of the E.W. Brown generating station, which includes Kentucky's largest solar farm, hydropower plant, natural gas units, and coal fired power plants.

generators rises significantly with the increase in intermittent renewable energy penetration. While it is nearly impossible to always match generation with demand for a service area, utilities are penalized by regulators for generation imbalances lasting longer than acceptable minutes [86, 87]. Hence, conventional hourly dispatch models are not suitable to identify the generation imbalances and effectively capture the effect of solar PV intermittency on evaluated service area.

This approach employs a minute-based dispatch since the solar PV power variability due to cloud cover is expected to reduce as the plant capacity and footprint increases. The proposed minute-to-minute dispatch model in this study was developed for the IEEE 12 bus test system illustrated in Fig. 3.2. The system which consists of four generating units was modified based on the specifications presented

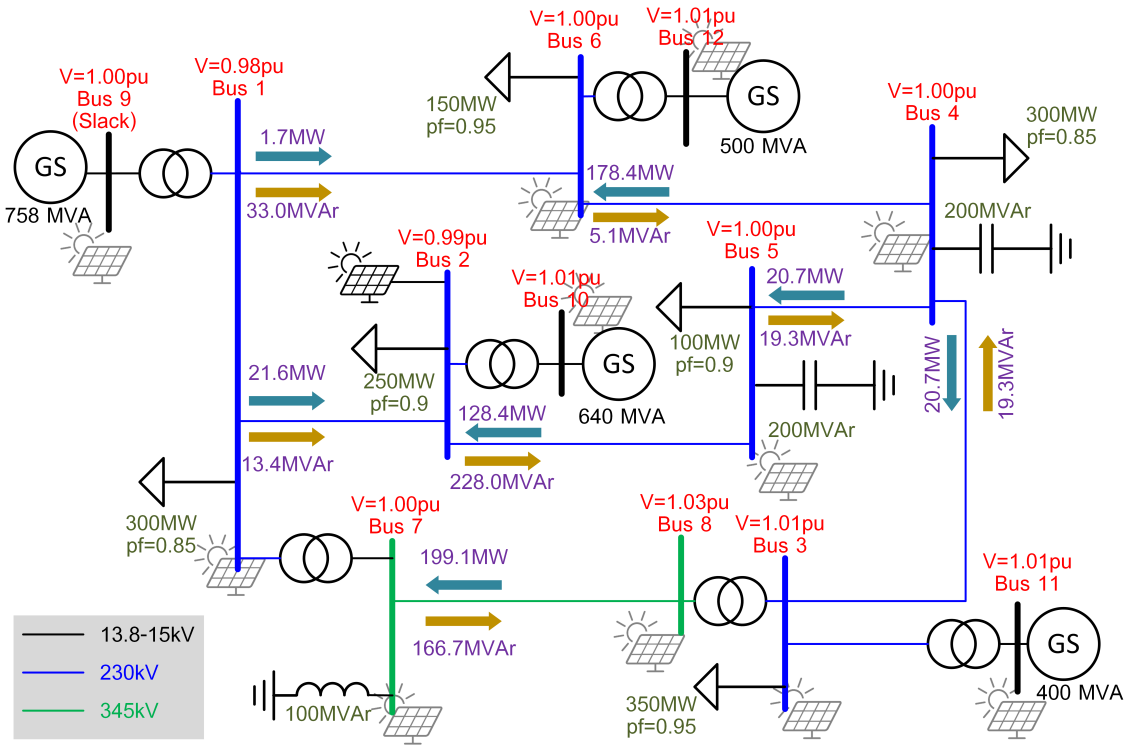

Figure 3.2: Single line diagram for the modified benchmark network with PV plant connected to bus 2 and values corresponding to approximately 65% (1450MW) load level. The transmission circuit was completely assessed for PV connection at any of its buses.

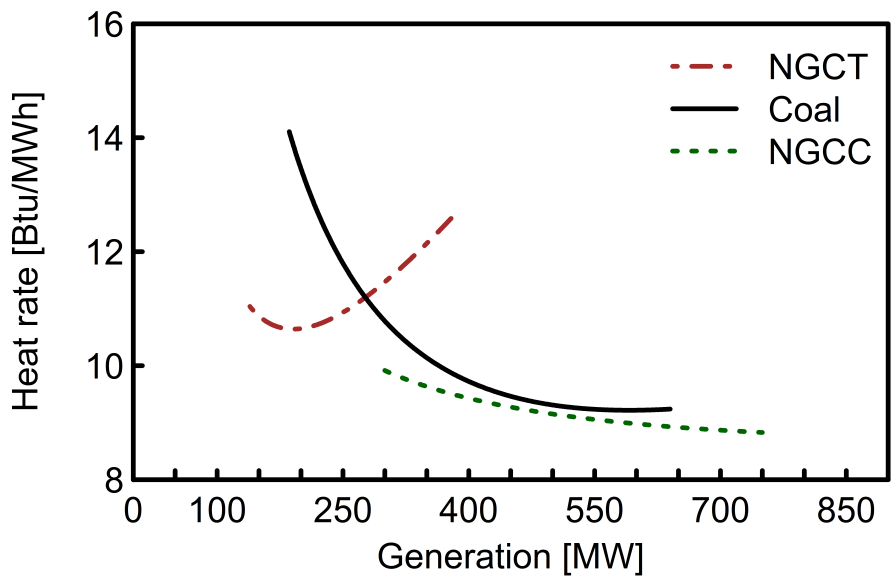

Figure 3.3: Example heat rate curve for natural gas combustion turbine (NGCT), coal, and natural gas combined cycle (NGCC) thermal generators considered in this study.

in Table 3.1 and subjected to realistic load variations for an example day in the Fall season. The efficiency of thermal generating units in terms of their heat rate vary with percentage output for different types of units (Fig. 3.3). In this approach, the heat rates for the thermal units are restricted by the maximum and minimum operation limits is described as follows:

$$\begin{bmatrix} Q_1^R(P_1) \\ Q_2^R(P_2) \\ Q_3^R(P_3) \\ \vdots \\ Q_G^R(P_G) \end{bmatrix} = \begin{bmatrix} Q_1^{in}/P_1 \\ Q_2^{in}/P_2 \\ Q_3^{in}/P_3 \\ \vdots \\ Q_G^{in}/P_G \end{bmatrix} \approx \begin{bmatrix} a_1 & b_1 & c_1 \\ a_2 & b_2 & c_2 \\ a_3 & b_3 & c_3 \\ \vdots & \vdots & \vdots \\ a_G & b_G & c_G \end{bmatrix} \cdot \begin{bmatrix} P_1^2 & P_2^2 & P_3^2 & \dots & P_G^2 \\ P_1 & P_2 & P_3 & \dots & P_G \\ 1 & 1 & 1 & \dots & 1 \end{bmatrix} \tag{3.1}$$

where, $Q_g^R(P_g)$ represents the heat rate for unit g with output power P_g; Q_g^{in} the heat requirement; and a_g, b_g, c_g are the heat rate co-efficient of the generator. Therefore,

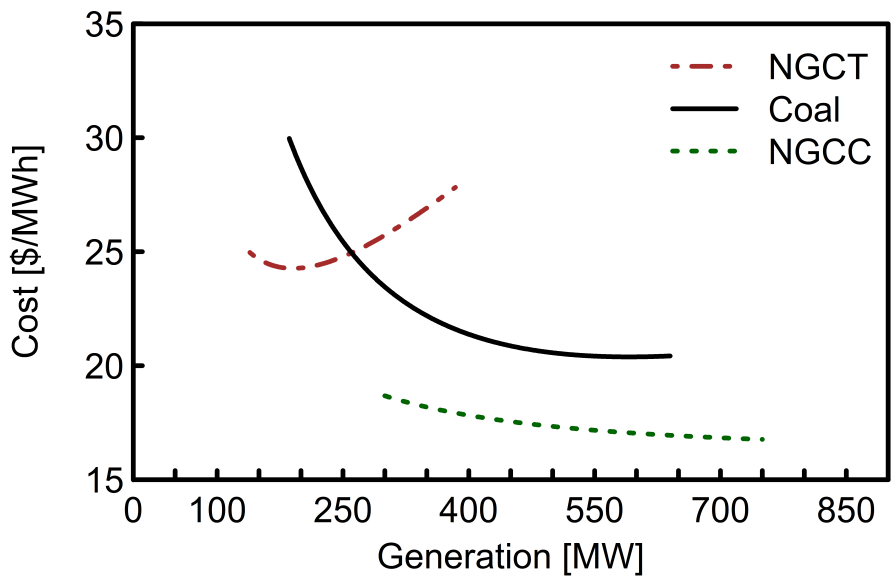

Figure 3.4: The operation cost including the fuel and auxiliary costs for the thermal units considered

the operating cost for each unit may be expressed as:

$$\begin{bmatrix} C_1(P_1) \\ C_2(P_2) \\ C_3(P_3) \\ \vdots \\ C_G(P_G) \end{bmatrix} = \begin{bmatrix} F_1 & Z_1 \\ F_2 & Z_2 \\ F_3 & Z_3 \\ \vdots & \vdots \\ F_G & Z_G \end{bmatrix} \cdot \begin{bmatrix} Q_1^R & Q_2^R & Q_3^R & \dots & Q_G^R \\ 1 & 1 & 1 & \dots & 1 \end{bmatrix} \tag{3.2}$$

where, C_g is the running cost for generator g; F_g, the fuel cost and Z_g, the fixed cost constant, which includes maintenance and emission reduction costs. Therefore, the proposed M-M dispatch model is capable of estimating the running cost of the thermal units for specified output level (Fig. 3.4). The running cost can also be multiplied by the MW output to form a monotonically increasing convex function, which may be further analyzed to calculate the incremental cost curve of each unit.

For a practical economic dispatch problem, the objective is to minimize cost and generation imbalance such that the cheapest combination of generators are regulated to meet demand. Therefore, the economic dispatch model objective can be expressed

as:

$$\min \begin{cases} C_T = \sum_{g=1}^{G} C_g(P_g) \\ \\ \epsilon = |P_T - L_c| \end{cases}, \tag{3.3}$$

where,

$$P_T = P_1 + P_2 + ... + P_G, \tag{3.4}$$

C_T, represents the total operating cost for all units considered; P_T, combined generator output; L_c, the combined service area load; and G the total number of operational units including the PV plant. Following theoretical developments in [88], the minimum C_T for each instance without considering generator constraints and transmission losses occurs when the total differential cost is zero and may be described as follows:

$$\partial C_T = \frac{\partial C_T}{\partial P_1} dP_1 + \frac{\partial C_T}{\partial P_2} dP_2 + ... + \frac{\partial C_T}{\partial P_G} dP_G = 0. \tag{3.5}$$

However, due to generator constraints including ramp-rate limitation of units the result from (3.5) may fall outside operation range. In this approach, the constraints for the thermal units are as follows:

$$\begin{bmatrix} P_1^{min}(t) \\ P_2^{min}(t) \\ P_2^{min}(t) \\ \vdots \\ P_G^{min}(t) \end{bmatrix} \leq \begin{bmatrix} P_1(t) \\ P_2(t) \\ P_2(t) \\ \vdots \\ P_G(t) \end{bmatrix} \leq \begin{bmatrix} P_1^{max}(t) \\ P_2^{max}(t) \\ P_2^{max}(t) \\ \vdots \\ P_G^{max}(t) \end{bmatrix} \tag{3.6}$$

$$\begin{bmatrix} P_1^{min}(t) \\ P_2^{min}(t) \\ P_2^{min}(t) \\ \vdots \\ P_G^{min}(t) \end{bmatrix} = \max \left\{ \begin{bmatrix} \underline{P_1} \\ \underline{P_2} \\ \underline{P_2} \\ \vdots \\ \underline{P_G} \end{bmatrix}, \begin{bmatrix} P_1(t-\Delta t) - \Delta t \cdot R_1^{down} \\ P_2(t-\Delta t) - \Delta t \cdot R_2^{down} \\ P_3(t-\Delta t) - \Delta t \cdot R_3^{down} \\ \vdots \\ P_G(t-\Delta t) - \Delta t \cdot R_G^{down} \end{bmatrix} \right\} \tag{3.7}$$

$$\begin{bmatrix} P_1^{max}(t) \\ P_2^{max}(t) \\ P_2^{max}(t) \\ \vdots \\ P_G^{max}(t) \end{bmatrix} = \min \left\{ \begin{bmatrix} \overline{P_1} \\ \overline{P_2} \\ \overline{P_2} \\ \vdots \\ \overline{P_G} \end{bmatrix}, \begin{bmatrix} P_1(t-\Delta t) - \Delta t \cdot R_1^{up} \\ P_2(t-\Delta t) - \Delta t \cdot R_2^{up} \\ P_3(t-\Delta t) - \Delta t \cdot R_3^{up} \\ \vdots \\ P_G(t-\Delta t) - \Delta t \cdot R_G^{up} \end{bmatrix} \right\} \tag{3.8}$$

where, $P_g^{max}(t)$ and $P_g^{min}(t)$ are the maximum and minimum output power for unit g, respectively; $\overline{P_g}$ and $\underline{P_g}$ are the specified maximum and minimum generator operation limits; R_g^{up} and R_g^{down}, the generator rising and falling ramp rates, respectively.

This study is focused on the impact of increasing PV penetration on an example system with five generators. The proposed framework economic dispatch model employs a multi-objective genetic algorithm (GA) to minimize C_T and ϵ for the three thermal units in the system and the "non-dispatchable" units (PV and hydro) output are set based on reference values from practical modules. Depending on the location of a hydro power plant and regulations preventing flooding, hydro power plant is typically the fastest ramping generator whose output can be in principle be varied to manage generation imbalance. Due to the inability to quantify water backlog that may lead to flooding, the output power for the hydro plant employed in this study was calculated based on an operational system. The solar plant reference power module was developed based on measured irradiance data retrieved from an operational solar PV farm. The PV output power is expressed as follows:

$$P_{pv} = \frac{\gamma}{1000} \times \eta \times \overline{P_{pv}}, \tag{3.9}$$

where P_{pv} is the PV plant power, γ is solar irradiance; η is the inverter efficiency, and $\overline{P_{pv}}$ is the rated capacity. The algorithm goes through multiple combinations

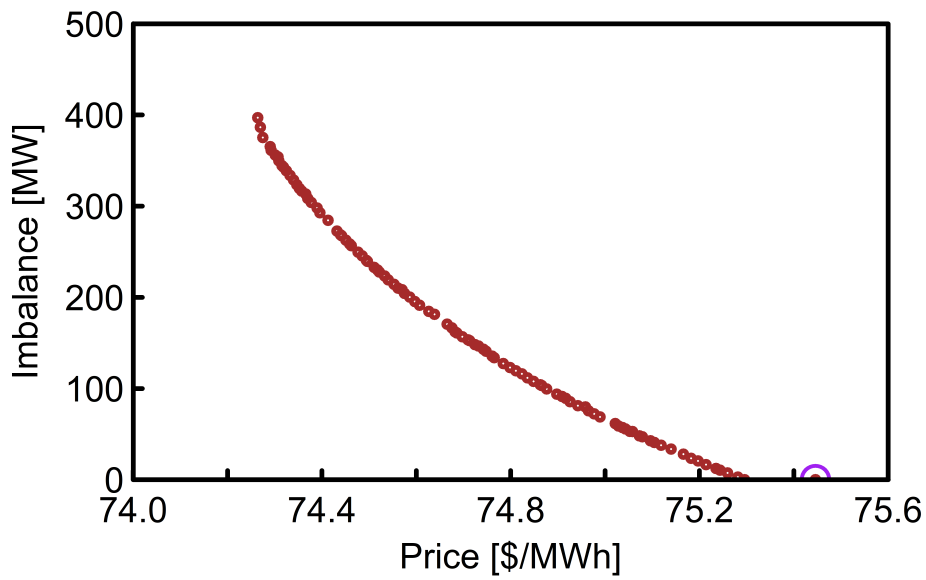

Figure 3.5: The multi-objective optimization Pareto front for example minute. The selected design is the one with the minimum imbalance for every case.

of generator set points limited by $P_g^{min}(t)$ and $P_g^{max}(t)$ for each unit to establish a Pareto front. Since the primary objective of the utilities is to meet demand, the design with the least amount of imbalance is selected for the simulation time-step (Fig. 3.5). In order to identify periods of over- and under-generation, the proposed M-M dispatch model assumes the generators in the transmission circuit are solely responsible for meeting demand for the concerned service area without need for off system sales and electricity power trading. Factors such as units commitment and outage are beyond the scope of this study. Therefore, all units are assumed to be available and committed throughout the example day.

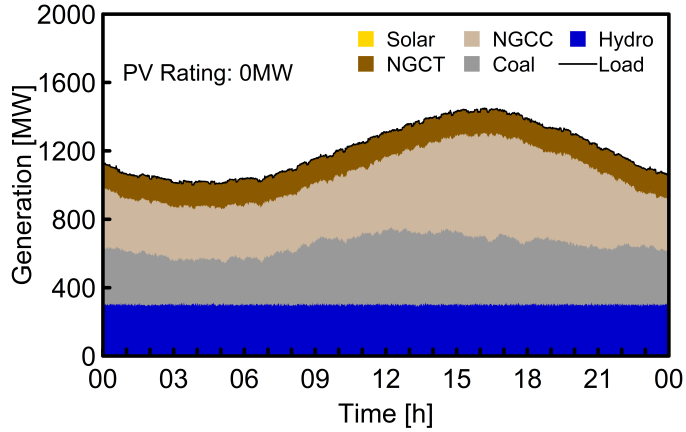

(a)

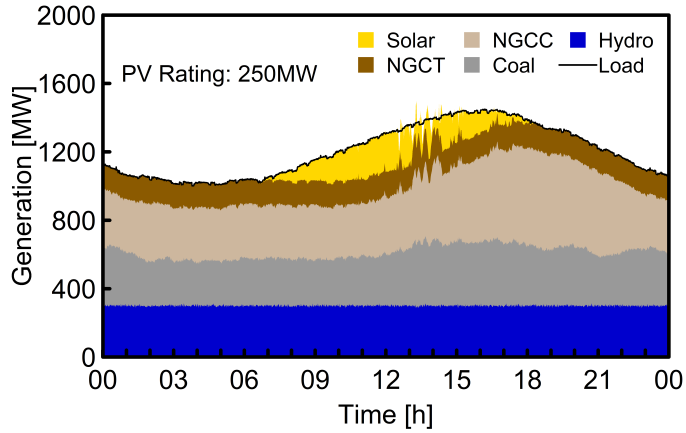

(b)

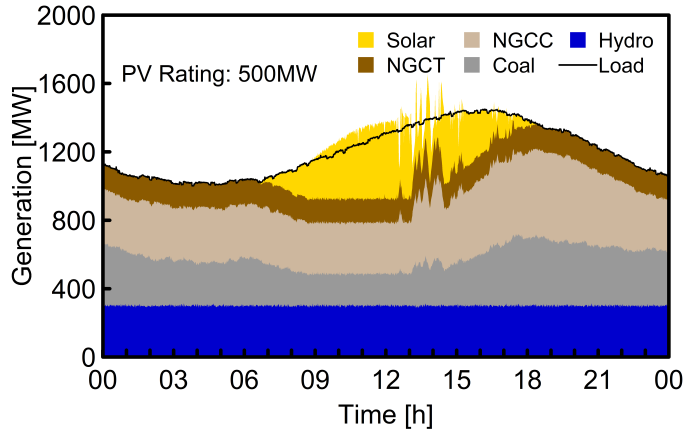

(c)

Figure 3.6: Minute-to-minute (M-M) unit economic dispatch highlighting the impact of increasing PV penetration on an example generation portfolio. The results indicate that large PV penetrations may lead to both over- and under-generation scenarios where combined power from units cannot match demand. The presented analysis include (a) no PV, (b) 250MW PV, and (c) 500MW PV penetration case studies.

3.3 Conventional generators response to increasing PV penetration

Increasing solar penetration can make it more challenging for grid operators to balance generation with load in real-time, since generating units are committed based on load forecast and level of uncertainty. In this study, the integrated PV farms are operated in "must-take" modes, in which thermal units are turned down to accommodate solar PV penetration. The relatively high power variation of the PV plant for the example day considered leads to significant generation imbalance during periods when the operating units cannot ramp up or down fast enough for meet demand.

Due to the minimum generation limit of the available thermal unit, a significant level of over-generation may be observed at hours between 9:00 and 13:00, when the generators could not ramp down further to accommodate the increasing PV penetration (Fig. 3.6). In addition to the rest time required to restart thermal units, a significant amount of time, up to 24 hours for some coal units is required to restart start them which makes it extremely challenging to turn off the units at midday and restart them for evening peak [89].

The current solar PV regulatory standards may not be sufficient for managing high intermittent renewable sources penetration and new standards will be required to ensure grid stability in a future grid [90, 91]. Furthermore, the penetration of distributed renewable sources such as rooftop solar will lead to substantial changes in the apparent load on the transmission network that may call for additional regulations. In this study, a generation violation or imbalance count is recorded when the

area control error, ACE, exceeds ±20MW for defined consecutive minutes. The ACE is expressed as:

$$ACE = (T_m - T_s) + \beta_f(f - f_s), \tag{3.10}$$

where, T_m and T_t are the measured and scheduled tie line lows, f and f_s, the measured and scheduled frequency, and β_f the frequency bias constant for the area. Frequency variation due to generation imbalance is beyond the scope of this study, therefore it was assumed that $f = f_s$, and T_s is always equal to zero. Hence, for this analysis (3.10) can be re-written as:

$$ACE = T_m = P_T - L_c. \tag{3.11}$$

The over- and under-generation imbalance count for the example day was evaluated for increasing PV penetration. A significant level of over-generation can be observed at solar PV penetration levels exceeding 400MW (Fig. 3.7). This is mainly due to the inability of the available units to operate at values below their minimum generation limits during periods of surplus solar generation. For the example day analyzed, there was no under-generation violation lasting more that 15 consecutive minutes (Fig. 3.8). However, significant under-generation violation counts for 5 and 10 consecutive minutes, which was relatively constant for PV penetration above 350MW was recorded. These violations are primarily due to the intermittent behavior of the PV systems and generating units not being able to ramp fast enough to supply deficit power due to sudden shading of the solar panels.

Solar power curtailment can be an effective tool for managing over-generation, in which the solar PV plant output may be held back when there is insufficient

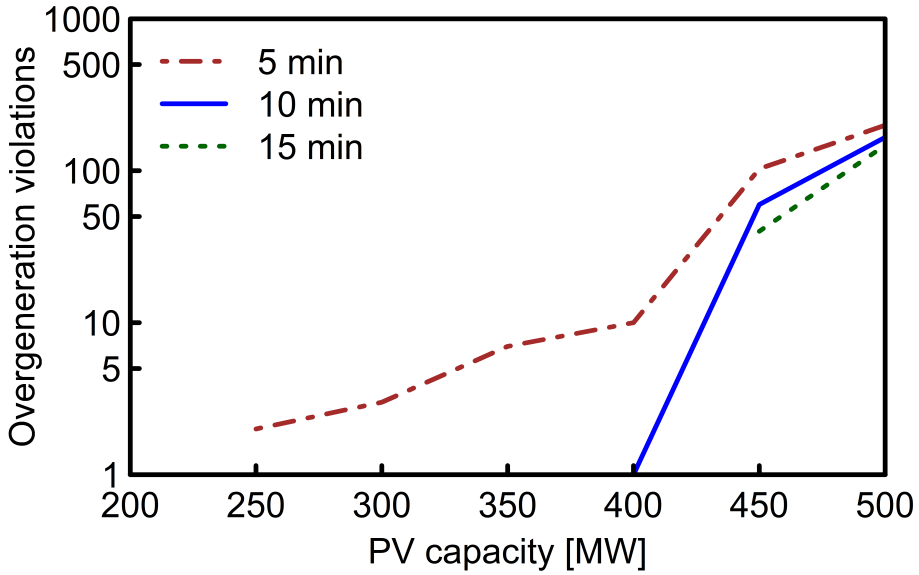

Figure 3.7: Example day over-generation violation count. In this approach a violation count is recorded when the dispatch imbalance exceeds 20MW over defined consecutive minutes (5, 10 and 15).

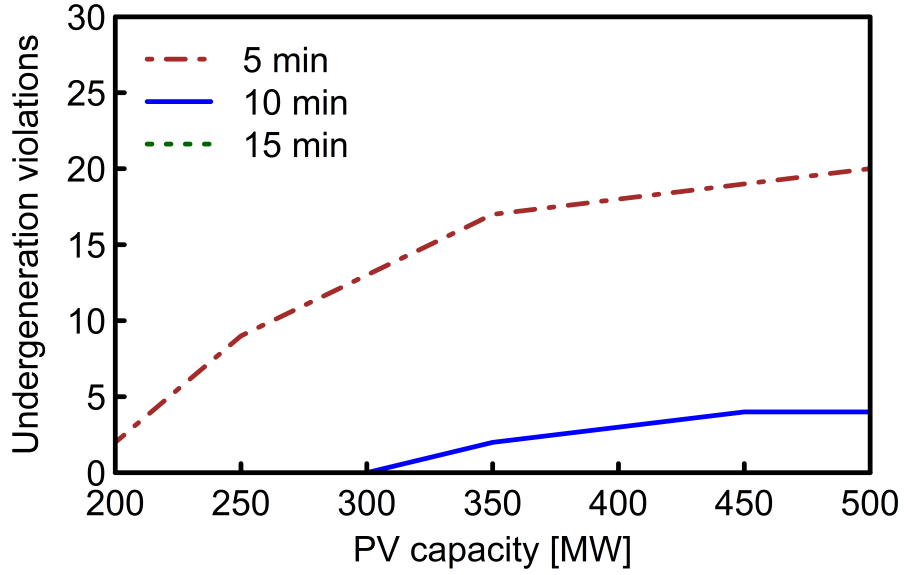

Figure 3.8: Under-generation violation count at increasing PV penetration rate. Under-generation occurs when PV becomes suddenly shaded and thermal units cannot ramp up fast enough to supply deficit power.

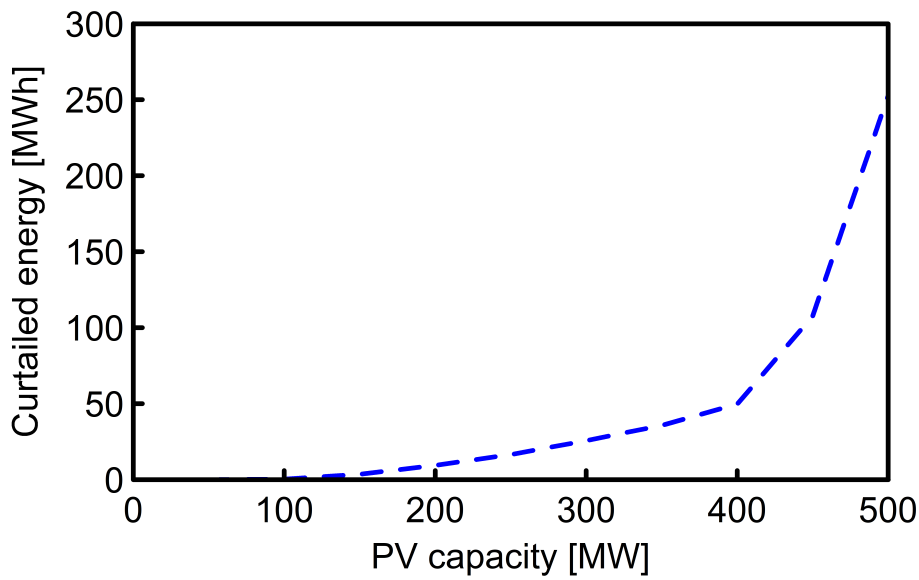

Figure 3.9: Curtailed energy solar energy for example day. In order to limit over-generation, an exponential increase in the total solar PV power curtailed can be observed.

demand to consume production. This study examined how much curtailment will be required to address solar over-generation for the presented generator portfolio over the example day (Fig. 3.9). An exponential increase in the curtailed PV energy in order to avoid over-generation violations was recorded, with rapid increase in curtailment for PV capacity above 400MW. Due to the substantial PV energy curtailed, over 2% reduction in PV capacity factor was reported at 500MW penetration level (Fig. 3.10). Increase in solar PV penetration is expected to lead to significant reduction in running cost without considering the capital cost for the PV system. It is however important to recognize that, PV penetration may lead to more aggressive usage of fast ramping units such as NGCTs, which are typically the most expensive units in generation portfolios. This study evaluated the cost savings for the example day due to increase in PV penetration. A somewhat steady increase in cost savings

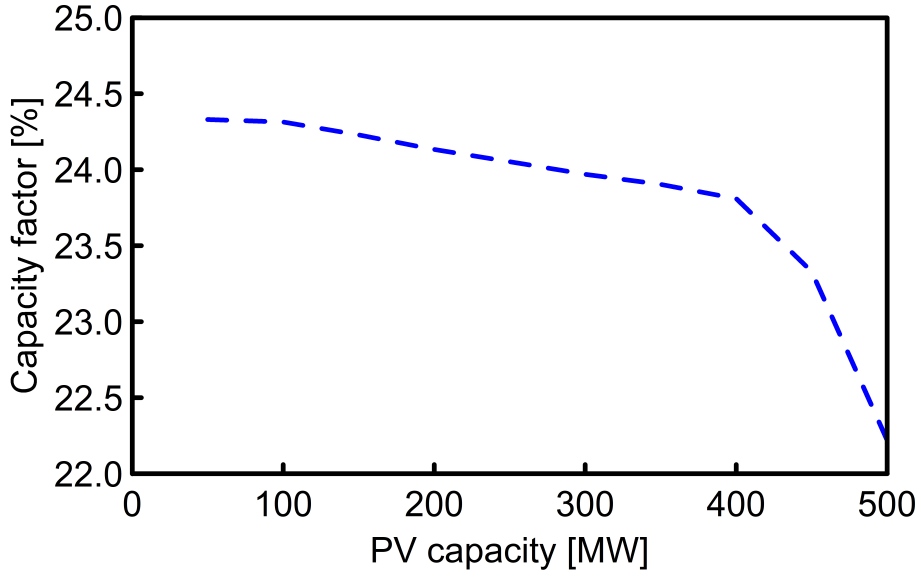

Figure 3.10: PV plant capacity factor based on penetration. Capacity factor can be observed to reduce with increase in curtailed power.

was reported for solar PV penetration above 80MW (Fig. 3.11). However, due to generator commitment and increased operation of the NGCT unit for managing the solar PV variation over the example day, no cost savings was recorded for solar PV penetration below 80MW.

3.4 Modified benchmark transmission network

The modified benchmark transmission system analyzed in this work represents a small islanded power system network with 12 buses and four generating units (Fig. 3.2). This modified transmission network is based on the generic 12-bus test system developed for wind power integration studies presented in [84]. The transmission network base case was developed in PSSE with a single transmission line connecting buses 3 and 4, as opposed to the parallel cables in the initial setup.

At steady-state without renewable integration, the transmission network total

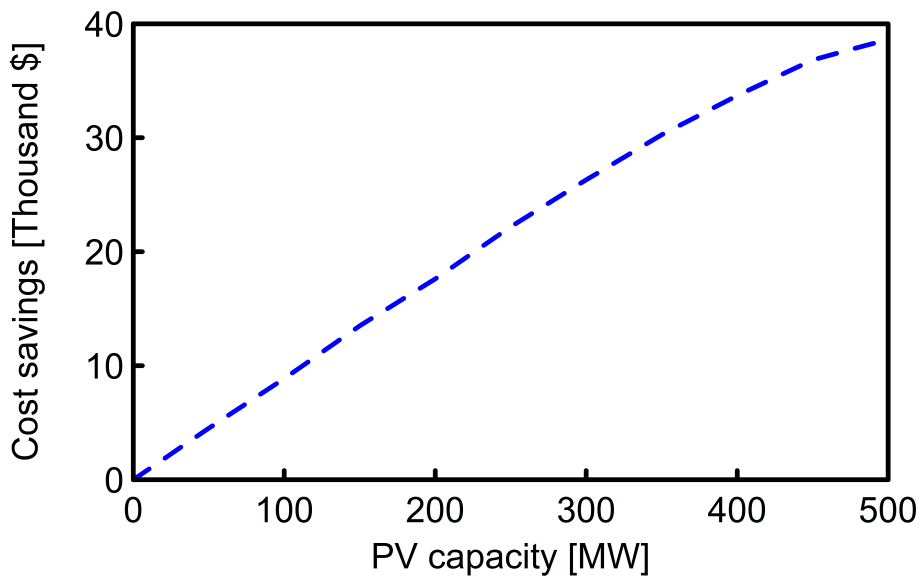

Figure 3.11: Operation cost saving due to increase in PV penetration. For the example day considered, an increase in operation cost was observed for PV penetrations below 500MW due to operation of inefficient units to meet demand.

system load is approximately 65% of the total generation capacity. The bus voltage voltages vary between 0.98pu to 1.03pu. In this example, each of the transmission lines is rated for a maximum of 250MVA power flow with the exception of the transmission lines connecting buses 7 to 8 and 3 to 4, which are rated to 500MVA. At 65% load level without renewable integration, the maximum loading for any of the transmission lines is 71%, which is the power flow between buses 6 and 4.

Solar PV penetration have the maximum impact on generation during periods when load is relatively low. For transmission networks, maximum PV impact is observed during peak periods, when load is rather high and transmission lines are near saturation. In this approach, the transmission network was evaluated for the analyzed example day peak demand and the generating units were dispatched according with respect to minimum operating cost and solar PV penetration.

The benchmark model was further modified to enable renewable system integration, such that a solar PV farm may be connected to either of its 12 buses. In order to connect the PV plant to a selected bus, an additional transformer is introduced to connect the PV plant terminal to the corresponding bus. Based on typical regulatory requirements, the PV plant is configured to be capable of operating at 0.95 power factor to support scheduled grid voltage at the point of interconnection (POI) [92].

3.5 Proposed framework for network PV hosting capacity

The PV hosting capacity for a transmission network is defined as the maximum solar PV capacity that may be connected to the system without significant upgrades to its circuit to ensure steady operation. The maximum hosting capacity of a transmission circuit depends on multiple factors including the bus voltage variation, thermal limits of the transmission lines, frequency variation, fault currents as well as regulated factors such as total harmonic distortion and grid codes. This study focuses on the maximum PV capacity that may be connected to any one of the buses in the example transmission network without violating the bus voltages or the thermal limits of the circuit branches.

The proposed framework established as a combination of modules developed in Python and transmission case studies in PSSE, may be employed to estimate the hosting capacity for a defined transmission network. Opposed to conventional approaches, this framework employs a practical and detailed economic dispatch model,

which defines the output power of all available generating units based on combined running cost. This dispatch model also respects generator minimum power limit and ensures units are set to values within their operation limits. Hence, the combination of units that meet load at the least cost are dispatched for each case study analyzed.

The framework allows the user to define the potential buses for PV connections, the range and maximum PV capacity to be analyzed, and the load levels to be considered. The simulation study is initialized with for the based case without solar PV penetration and the case study is evaluated. The combined load for the analyzed instance is then distributed to all the load buses at a ratio and power factor identical to the base case. The transmission network is then modified such that the minimum PV capacity to be evaluated is connected to the first candidate bus to be analyzed. All the available generators are re-dispatched to accommodate the increase in PV penetration.

The modified circuit is solved in PSSE, and the connected PV rating is increased if the solution converges. The framework keeps increasing the connected PV rating at predefined steps until solution failure or maximum PV rating to be analyzed, after which it resets to a minimum PV rating for the next bus or load level. The simulation comes to an end after the combinations of all PV ratings, connection buses and load levels have been exhaustively tested and results extracted (Fig. 3.12). Based on the criteria defined for the system circuit, the collected results are therefore analyzed to determine the system's maximum hosting capacity.

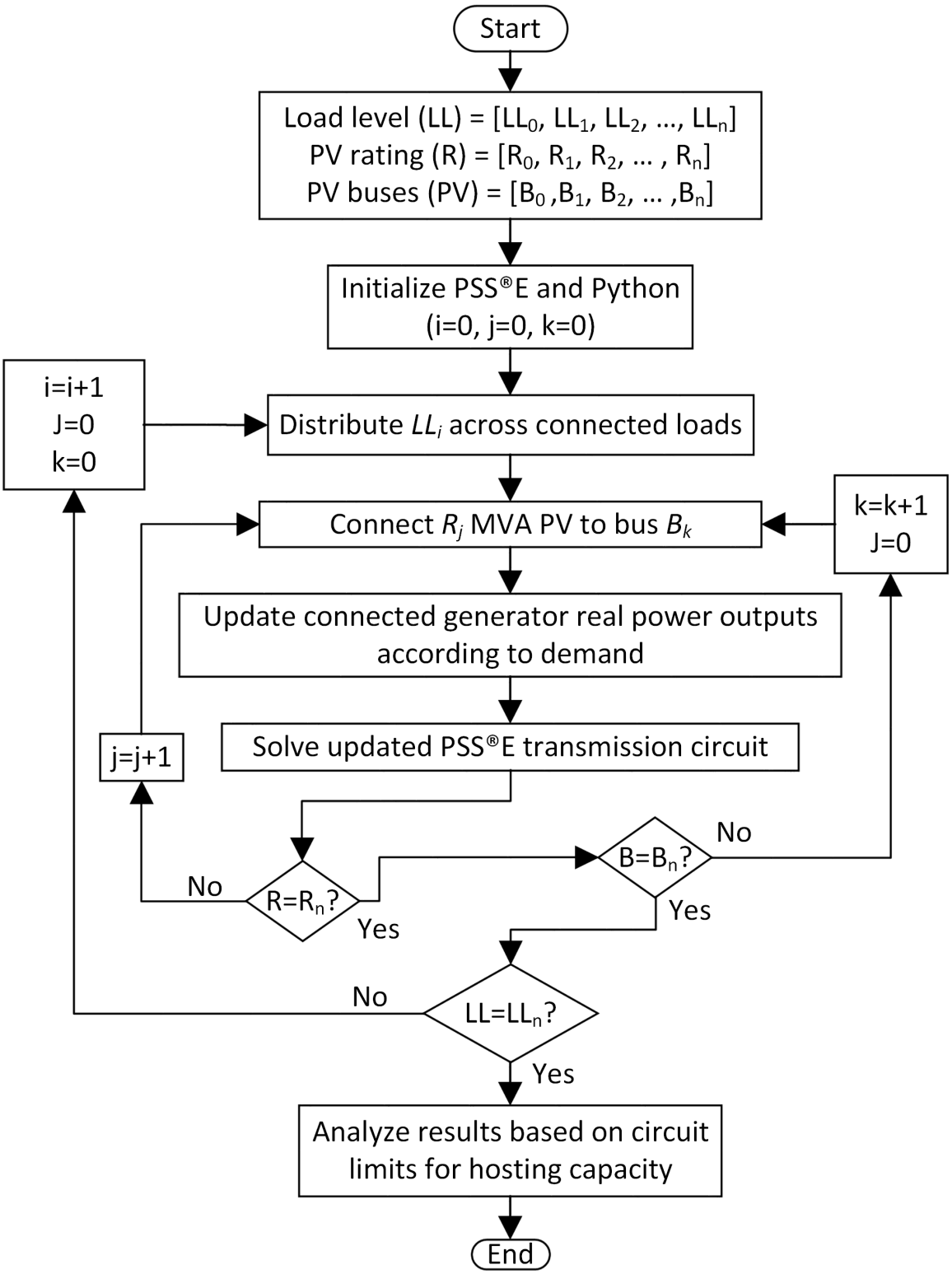

Figure 3.12: Operational flow chart for the proposed framework for estimating the hosting capacity on a transmission network. The steady state impact for increasing solar PV capacity at different POI was evaluated to estimate the maximum PV hosting capacity for the network.

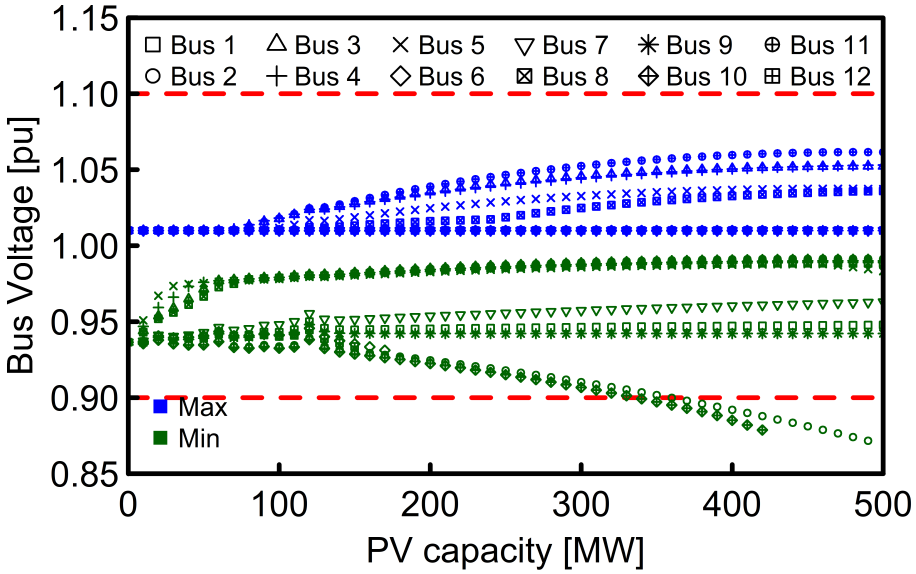

Figure 3.13: The maximum and minimum bus voltage variation for increasing PV capacity over multiple points of interconnection (POI). A PV capacity is undesirable if it leads to bus voltage variation above 1.1 or below 0.9pu.

3.6 Transmission network response to increasing PV capacity

The proposed framework was employed to estimate the PV hosting capacity for the modified IEEE 12 transmission network. The PV hosting capacity was evaluated based on the bus voltage responses of the network, thermal loading and circuit solution convergence. The network was evaluated at 1450MW combined load level, which represents the peak demand for the example day analyzed. Up to 500MW PV penetration level was analyzed for the defined POI and the operational conventional generators were re-dispatch for each case to ensure the combination generator output power with the least cost is selected. the defined POI and the operational conventional generators were re-dispatch for each case to ensure the combination generator output power with the least cost is selected.

Contrary to conventional assumptions, increasing PV penetration does not only lead to increase in bus voltage. This capability for increasing solar PV capacity to lead to both increase and decrease in bus voltages was demonstrated in this study. Variations in bus voltage in some cases are due to substantial changes in power flow, hence significant changes in the voltage drop across the transmission lines. Utilities are typically regulated to maintain their bus voltages within certain limits, and this study assumes a violation when any of the bus voltages exceeds 1.1 or below 0.9pu. Due to multiple factors including substantial circuit violations, networks solutions for PV capacity beyond certain values do not converge and such cases are only evaluated based on available solutions. The maximum and minimum bus voltages for the network varies based on the PV POI as illustrated in Fig. 3.13. Hence, up to 320MW PV capacity can be connected to any of the transmission circuit buses without any voltage violation.

The maximum and minimum bus voltage in a transmission network is significantly influenced by the scheduled voltages of the connected generator units. Hence, a measure of the maximum and minimum bus voltages alone may not be able to capture the impact of increasing solar PV penetration. In addition to the maximum and minimum bus voltage limits, utilities are typically required to maintain bus voltage variation within certain values. This maximum voltage deviation can also be an indicator of the expected voltage variations due to the PV intermittency. For this study, a PV capacity that leads to bus voltage deviation that exceeds 0.08pu is undesirable. The maximum voltage deviation varies based on PV capacity and POI as illustrated in Fig. 3.14. Based on this analysis, up to 140MW PV may be connected to any of

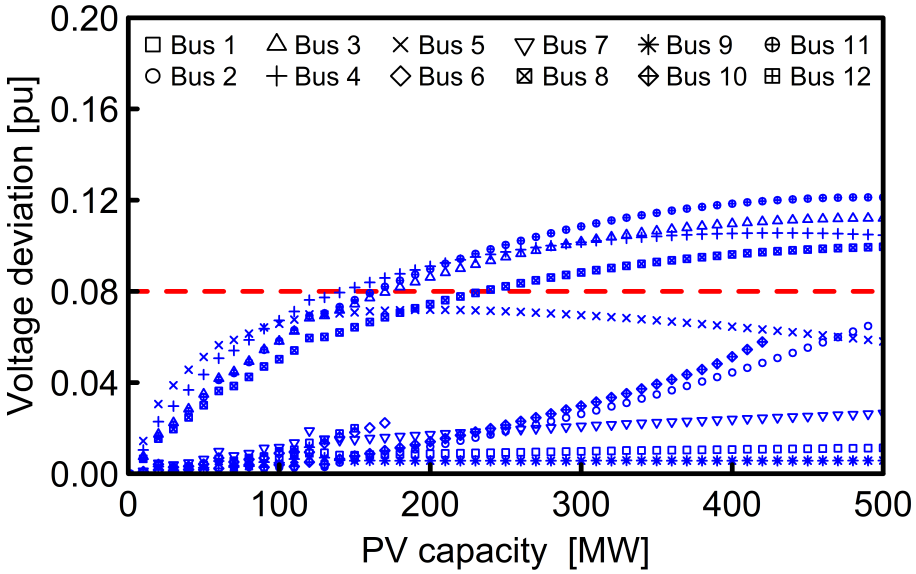

Figure 3.14: Maximum bus voltage deviation for defined PV capacity. A violation is recorded if the maximum voltage deviation exceeds 0.08pu. The maximum voltage deviation is also an indicator of the expected voltage variation due PV intermittency.

the circuit buses with bus voltage deviations exceeding 0.08pu.

Transmission line power flow are typically limited to restrict the temperature attained by energized conductors and the resulting sag and loss of tensile strength. This study focuses on the maximum PV penetration the network can sustain at steady state of a substantial period of time. Hence, the percentage loading for on all the transmission lines were evaluated for defined solar PV capacity. A thermal violation is recorded when the maximum transmission line loading exceeds 100% of its rated capacity. For the example network considered, buses 10, 11 and 12 are the least desirable for PV connection without over loading any of the transmission lines (Fig. 3.15). Based on this analysis, up to 110MW PV may be connected to any of the buses without any thermal violation.

For this example study, a PV capacity is acceptable if all the bus voltages are

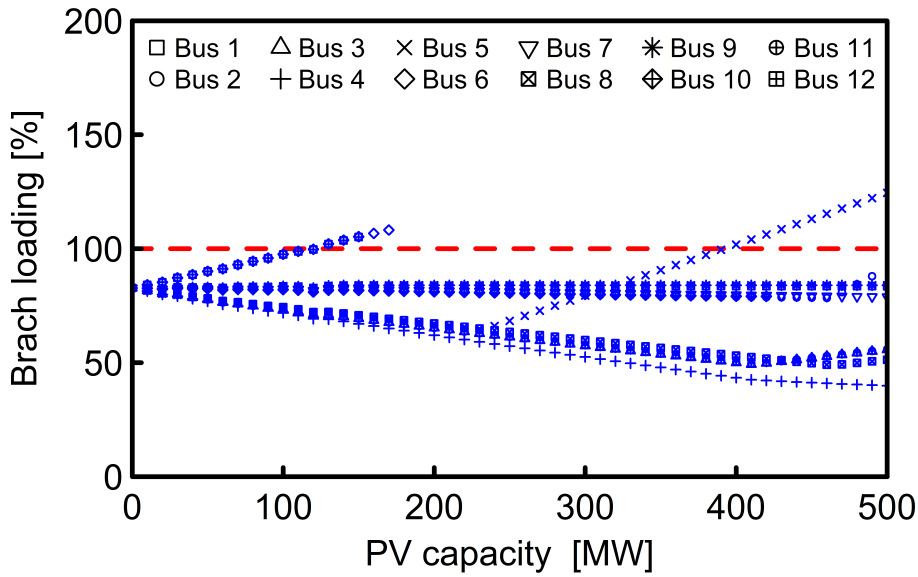

Figure 3.15: Maximum transmission line loading. Depending on the POI, PV integration may lead to substantial reduction in transmission line loading.

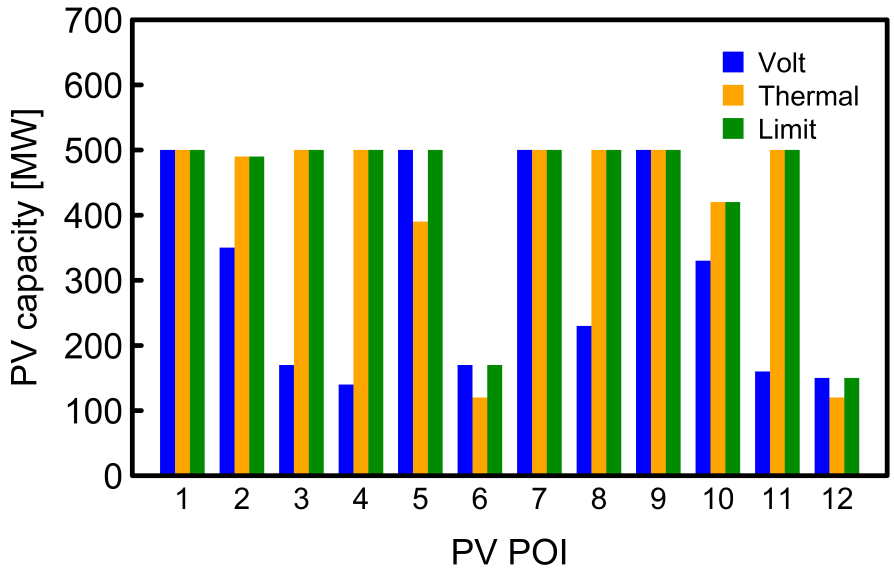

Figure 3.16: Maximum PV hosting capacity with respect to the circuit solution convergence(Conv), voltage violation and thermal limits at peak load level.

within 0.9-1.1pu, voltage differences with and without PV do not exceed 0.08pu for any bus, and the thermal loading for any of the transmission lines is below 100%. Study is primarily focused on PV penetrations without significant changes to existing infrastructure, therefore, supplementary devices such as voltage regulators, capacitor banks, and other complementary tools were not considered. This study demonstrates that the maximum PV capacity without any network violation depends on the PV POI (Fig. 3.16). Based on the maximum PV capacity for the analyzed cases without voltage or thermal violations, the preferred PV POI for the analyzed network are buses 1,7 and 9 which are close to the largest operating generator.

3.7 Battery energy storage system impact on transmission networks with large solar PV penetration

The desire for cleaner sources of energy is significantly increasing the penetration of inverter-based resources (IBR) such as solar PV, wind and BESS. These IBR pose multiple challenges to the traditional grid operation and substantial modeling and simulation efforts will be required to effectively capture their impact on both generation and transmission systems [1]. This study evaluates the impact of large solar PV and BESS impact on an example transmission network.

Recent studies have been focused on the steady state simulation and analysis of large solar PV and BESS [93, 94]. Energy storage systems when appropriately size is in principle are capable of mitigating most of the challenges related to solar PV

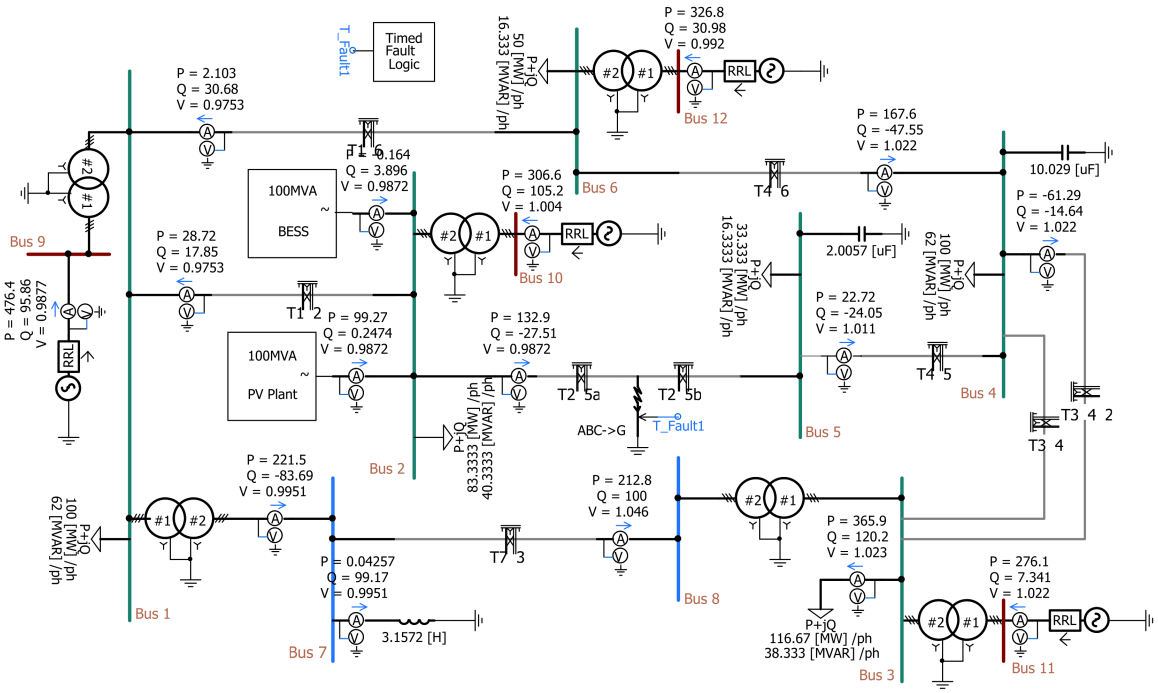

Figure 3.17: Single line diagram for the modified IEEE 12 bus system developed in PSCAD/EMTDC with solar PV plant and BESS connected to Bus 2. The BESS system may be configured to charge or discharge to mitigate the impact of PV system intermittency and regulate its reactive power output to support its terminal voltage.

integration. Multiple energy storage system applications including, frequency regulations and voltage support through Volt-VAr mode have been presented in literature [95].

This study evaluates through computer simulations the impact of BESS on transmission networks with relatively high solar PV penetration. In this approach, the IEEE 12 bus model proposed in [96] was modified to include a 100MW PV and BESS connected to Bus 2 (Fig. 3.17). Opposed to conventional approaches, where IBR module are either represented by average models which do not effectively capture the contributions of high frequency power electronics devices [97, 98], or detailed models which require significant computation power to simulate large solar PV farms [99], this study proposes a dynamic IBR module suitable for the comprehensive evaluation of its impact on the grid.

The proposed IBR module was modified to represent a BESS and solar PV plant connected to the example transmission network. The modules performance and response to changes in solar irradiance and transient fault conditions were evaluate through two PSCAD/EMTDC simulation case studies. The results from the simulation studies demonstrates how BESS may be used to supply deficit power from PV system and support the transmission system voltage. Furthermore, the results validated that adequately sized BESS when operated in Volt-VAr mode is capable of preventing substantial voltage drop during transient fault conditions.

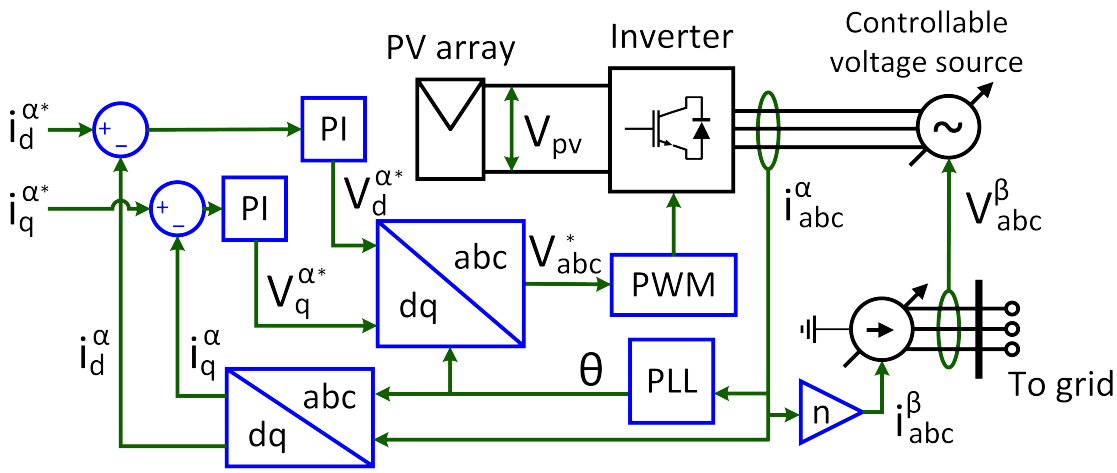

Figure 3.18: Proposed dynamic model for solar PV system. This module combines the benefits of both detailed and average models. The model can also be employed for other IBR such as BESS and wind.

3.8 Dynamic PV and battery module in PSCAD/EMTDC

Inverter-based resources such as PV systems have been traditional represented as controllable current sources whose output is mainly regulated by solar irradiance. The inverters from these models generate balances sinusoidal currents without harmonics at a fixed frequency and are not suitable for unbalanced fault studies such as single line-to-ground or line-to-line-to-ground. Detailed models including power electronic switches have been presented in literature. However, these models become complex and required significant computational power when simulating the performance of utility-scale systems which typically required multiple inverter modules.

This study proposes a dynamic IBR resource module with variable capacity which can be employed for multiple systems including solar PV, wind and battery system.

The proposed module may be regarded as hybrid system that combines the comprehensive benefits of detailed IBR models with the reduce computational requirement of the average models. Hence, simulations with the proposed IBR module have a limited number of electrical nodes when compared to the detailed models. In this approach, the output of a three-phase controllable current source is proportional to the output current of a representative detailed IBR model, which includes high frequency power electronic models and control as illustrated in Fig. 3.18.

The proposed dynamic model for the PV system in this study includes a detailed 1MW solar PV plant developed based on [44] and connected to a controllable voltage source, whose magnitude, phase and frequency is identical to the dynamic module point of interconnection. The output current of the detailed model is then used to regulate the output current of the three-phase current source used to represent the dynamic model.

For this example PV module in this study, the inverter control is used to maintain the PV array at maximum power point such that:

$$i_d^{\alpha *} = (V_{mt}^{\alpha} - V_{pv}^{\alpha}) \times \left(K_p + \frac{K_i}{s} \right), \tag{3.12}$$

$$i_q^{\alpha *} = (Q_{ref}^{\alpha} - Q^{\alpha}) \times \left(K_p + \frac{K_i}{s} \right), \tag{3.13}$$

where, $\mathrm{i}_{dref}^{\alpha}$ and $\mathrm{i}_{qref}^{\alpha}$ represent the d and q current components of the detailed PV systems, respectively; V_{mt}^{α} and V_{pv}^{α}, the MPP reference voltage and the PV array voltage, respectively; K_p and K_i, the PI controller proportional and integral constants, respectively; and $\mathrm{Q}_{ref}^{\alpha}$ and Q^{α}, the detailed PV system reference reactive power and

actual reactive powers, respectively. Since the terminal voltage of the detailed PV module is identical to the average system point of interconnection potential and the average IBR module output current is proportional to the detailed PV module current, the proposed IBR module real and reactive powers may be expressed as:

$$P^{\beta} = \frac{2}{3} \times \left(v_d^{\alpha} i_q^{\beta} + v_q^{\alpha} i_d^{\beta} + 2 v_0^{\alpha} i_0^{\beta} \right) = P^{\alpha} \times \frac{S^{\beta}}{S^{\alpha}}, \tag{3.14}$$

$$Q^{\beta} = \frac{2}{3} \times \left(v_q^{\alpha} i_d^{\beta} - v_d^{\alpha} i_q^{\beta} \right) = Q^{\alpha} \times \frac{S^{\beta}}{S^{\alpha}}, \tag{3.15}$$

where, P^{α}, P^{β}, Q^{α}, and Q^{β} represent the average and detailed module real and reactive powers, respectively; v_d^{α} and v_q^{α}, the d and q voltage components of the detailed PV systems; and S^{α}, and S^{β}, the MVA capacity for the detailed and average modules, respectively. The solar PV array of the presented dynamic IBR module may be replaced with a dc voltage source to represent a BESS.

3.9 PV and battery energy storage system transient response

Large solar PV penetration posses multiple threats to the stability of the traditional power system due to the high variation of its output power and the inability to accurately forecast its generation. Battery energy storage systems in principle may be employed to mitigate some of these challenges. The impact of transient irradiance variation on the solar PV plant operation and the response the BESS system was simulated and analyzed for the example transmission circuit presented in Fig. 3.17. In this case, the solar PV array irradiance suddenly falls from 1000W/m^2 to 200W/m^2

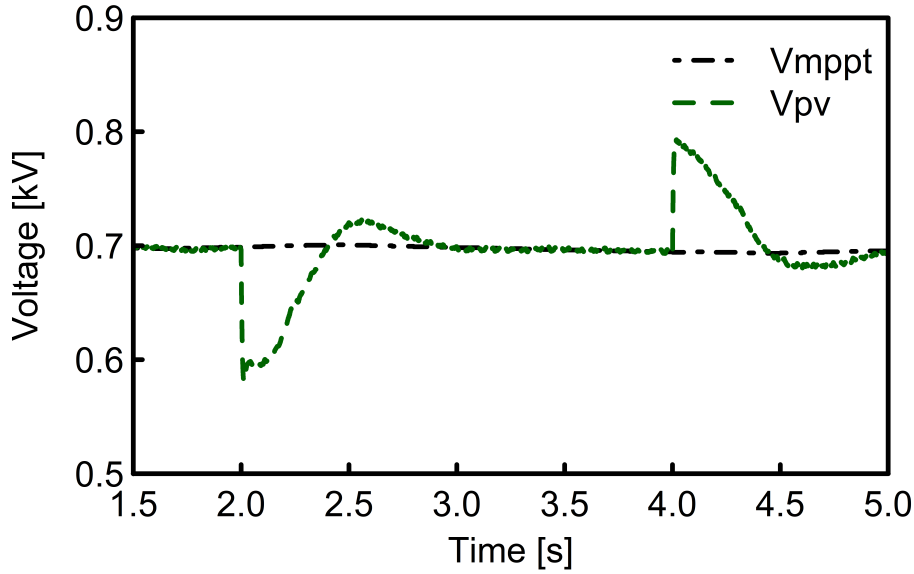

Figure 3.19: PV array terminal voltage (V_{pv}^{α}) and maximum power point reference (V_{mt}^{α}) for the representative detailed model. The inverter control system varies its real power output in order to maintain V_{pv}^{α} at reference value during PV shading from 2-4s simulation time.

for 2s at 2s simulation time. The detailed PV module the regulates its real power output in order to maintain the PV array voltage at its reference value (Fig. 3.19).

The sudden loss of power from solar PV systems due to its intermittency can lead to substantial power system challenges including voltage and frequency violations that may eventually extend to widespread outages [100]. For this study, the BESS was sized to be comparable with the PV systems and configured to supply deficit power during shading. Hence, the BESS real power output increases in response to the sudden PV shading to ensure the summation of the PV and BESS power is maintained at the system capacity (Fig. 3.20). The voltage for any bus within a transmission network is typically limit between 0.9-1.1pu and performance exceeding these limits may be recorded as a violation. For the modified IEEE 12 bus system employed, the voltage variation for Bus 2, which is the closest to the PV system

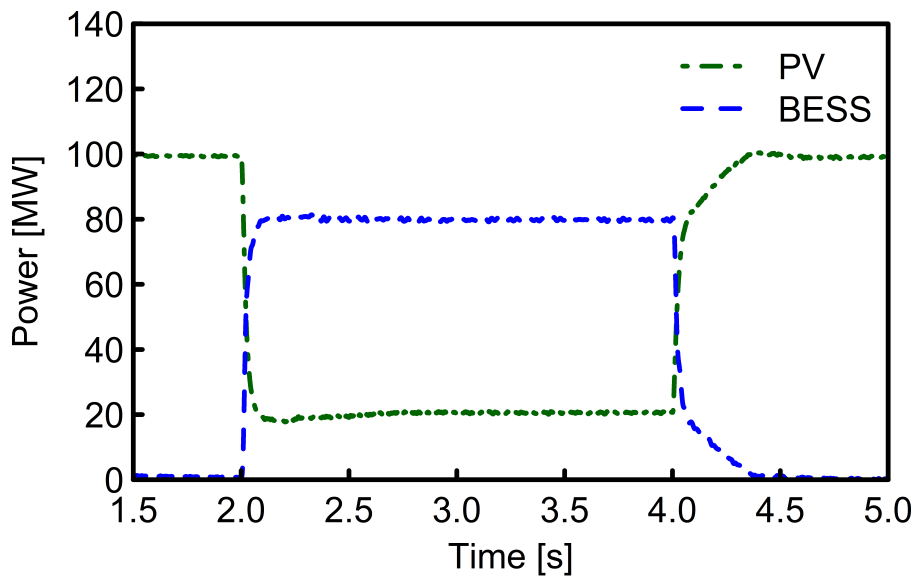

Figure 3.20: The real power output from the dynamic PV module, P^{pv}, and the BESS, P_{bs}. The BESS supplies the solar PV system deficit power in order to improve grid performance during PV transient conditions.

was evaluated for cases with and without the BESS. Based on the simulation results, by supplying the deficit power from the PV system, the BESS was able to mitigate approximately 0.07pu transient voltage drop at Bus 2 (Fig. 3.21).

3.10 Battery energy storage system Volt-VAr operation

Battery energy storage systems may be employed to regulate bus voltages during steady-state and transient conditions in order to accommodate increasing solar PV penetration without significantly impacting power quality and reliability of a transmission network. Hence, the BESS is configured to absorb reactive power when the bus voltage exceeds the tolerance setting and vice-versa. In this example study, the

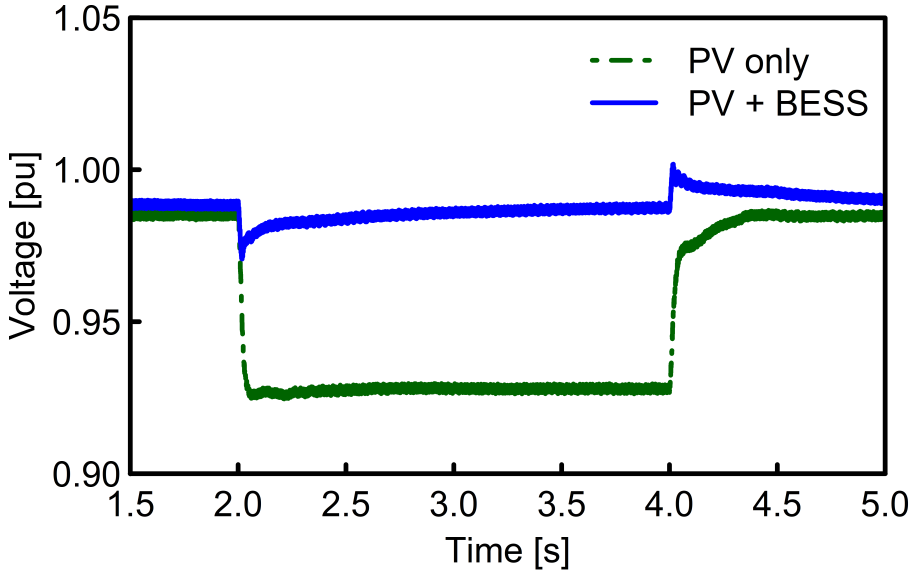

Figure 3.21: The voltage variation for Bus 2 with and without the BESS. For this example case study, the BESS was able to mitigate approximately 0.07pu drop in transient voltage drop.

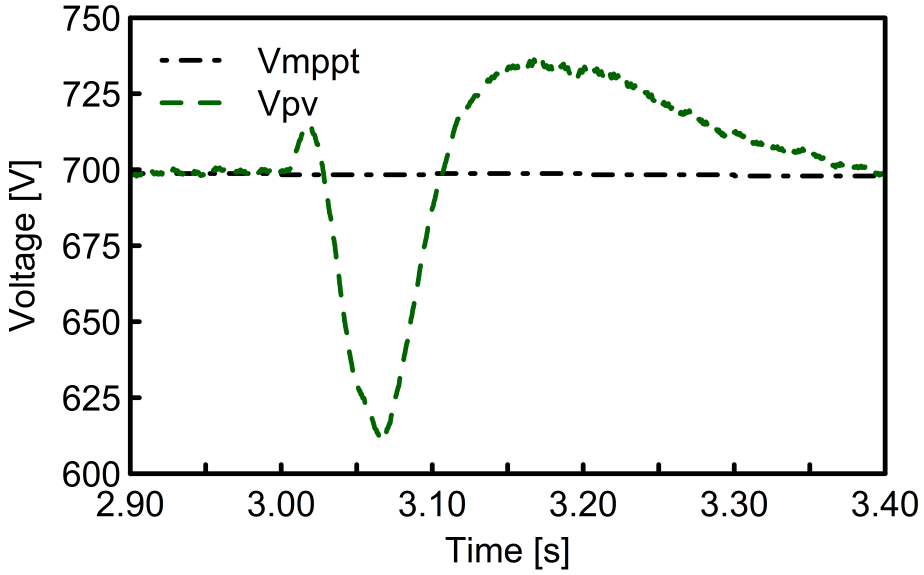

Figure 3.22: Detailed PV array terminal voltage and corresponding MPP reference during transient fault condition at 3s simulation time.

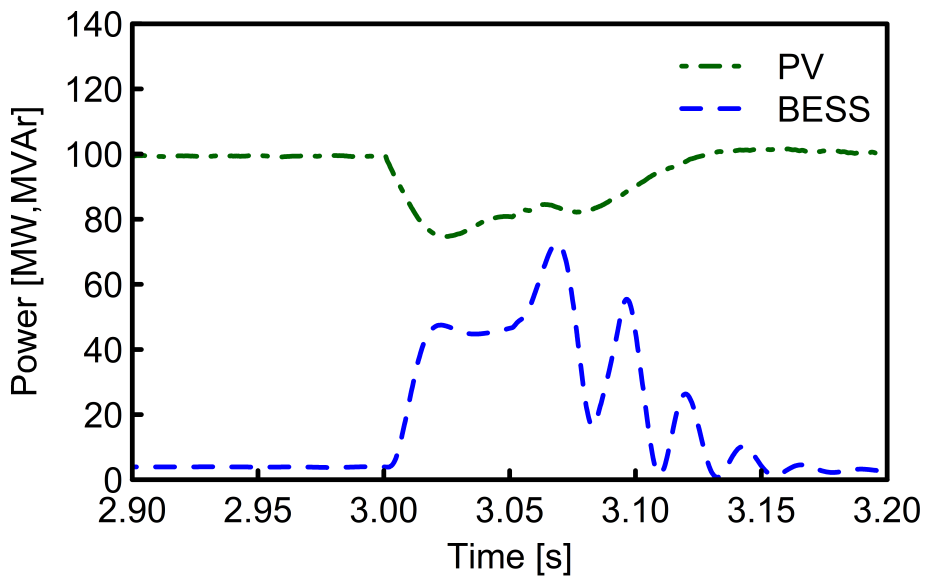

Figure 3.23: The PV and BESS response during transient fault for 0.05s duration. The BESS was regulated to supply or absorb reactive power in response to its terminal voltage variation.

BESS reactive power support is inactive when its terminal voltage is within 0.995-1.005pu and supplies or absorbs 50% of its reactive power capacity when its terminal voltage is below 0.9pu or above 1.1pu, respectively. The reactive power is linearly interpolated for voltage within 0.9 - 0.995pu and 1.005-1.1pu accordingly.

Furthermore, the response of the BESS connected to Bus 2 on the modified IEEE 12 bus was evaluated for a three-phase fault on line $T2\_5$ at 3s simulation time, which lasted for 0.05s. The fault condition in addition to the PV terminal transient voltage reduction led to a sudden drop in the system dc-link voltage before the inverter controller moves to maintain the PV array voltage at its MPP (Fig. 3.22). During the fault condition, the BESS increased its reactive power output in order to support the grid operation and minimize the voltage drop at its POI (Fig. 3.23). The results of the simulation indicate that the BESS was able to significantly reduce the voltage

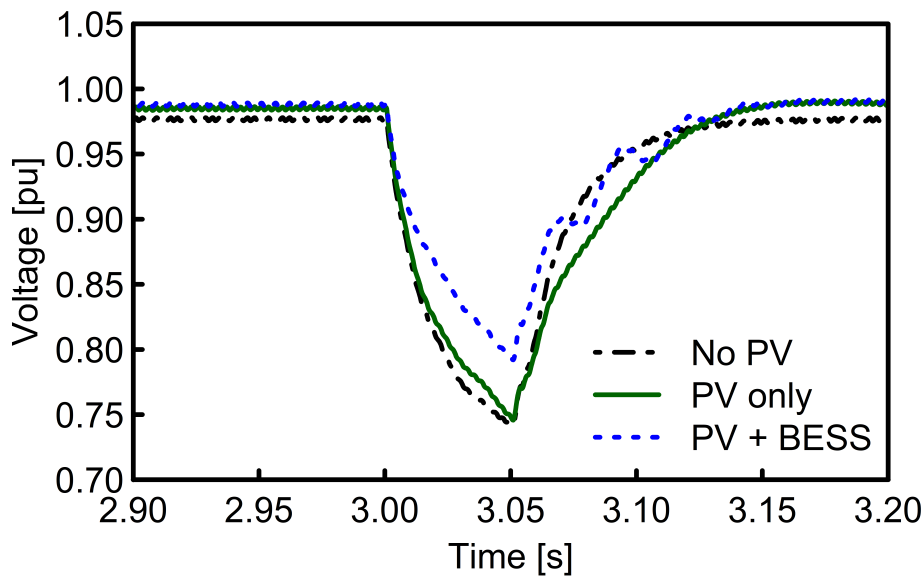

Figure 3.24: The voltage response for Bus 2 during fault condition. The reactive power response from the BESS led to substantial reduction in the bus voltage drop during fault.

drop due to the fault condition compared to the case studies with and without the PV (Fig. 3.24).

3.11 Summary

This chapter proposes an analytical framework, which includes a minute-to-minute economic dispatch model and a transmission network analyzing module for the evaluation of large solar PV impacts on both the generation and transmission systems. This framework can be employed for multiple applications including studies for estimating the maximum solar PV capacity a service area can support, the generation violations due to solar PV penetrations, the preferred location to connect solar PV plants, and the power system violations on the transmission network due to solar PV penetration. Furthermore, the proposed framework may be adopted for other

intermittent sources such as the wind power plants, and evaluate their effect on both the generation and transmission network system.

The detailed technical benefits for the proposed framework were demonstrated through the evaluation of the impact of increasing solar PV penetration on both the generation and transmission network for a modified IEEE 12 bus system with four conventional generators. Contrary to conventional approaches based on hourly dispatch models, the proposed technique employs a detailed minute-to-minute economic dispatch model to capture the impact of increasing PV penetration and identify periods of generation imbalance suitable for regulatory practices. Additionally, the framework was used to estimate the maximum PV hosting capacity for the transmission network with regards to the bus voltage and transmission line violations.

This chapter also presents a dynamic IBR module that may be used to analyze the performance and impact of large solar PV and BESS integration into the power system grid. The proposed dynamic IBR module may be employed for multiple applications including network performance assessments, solar PV hosting capacity estimation and new IBR regulations evaluation. Contrary to conventional approaches, this study presents a dynamic module that captures the impact of IBR power electronics and combines the benefit of corresponding detailed and average IBR modules.

The detailed technical benefits of the proposed module with respect to PV and BESS penetration impact on a modified IEEE 12 bus system was demonstrated through two case studies for BESS real and reactive power support. The simulation results demonstrate that BESS may be used to improve transmission network

PV hosting capacity and regulate the bus voltage variations due to solar PV intermittency and transmission line fault conditions.

Based on the results for the example transmission circuit and generators responses for the day evaluated, the maximum capacity of the solar PV plant a service area can sustain without needing significant upgrades to the existing infrastructure depends on, the available units specifications, the PV point of interconnections, and the voltage and thermal limits of the transmission network buses and lines, respectively. The results from the example 2,248 MW system evaluated indicate that up to 120MW PV plant can be connected to any of the buses in the transmission network without any voltage or thermal violation at peak load. The hosting capacity of the transmission network considering solar PV plants at multiple POI and the integration of battery energy storage systems to improve the acceptable PV capacity on the circuit are subjects of ongoing studies.

Chapter 4

Parameter Identification for Cells, Modules, Racks, and Battery for Utility-Scale Energy Storage Systems

4.1 Introduction

According to the EIA, utility-scale BESS in the U.S. account for more than 75% of the total energy storage capacity installed in 2018 [101]. The future electric grid may be able to take advantage of these predominantly Lithium-ion (Li-ion) based BESSs at the distribution, transmission and generation levels for multiple applications including voltage and frequency support, load leveling and peak power shaving, spinning reserve, and other ancillary services [102]. However, recent developments surrounding Li-ion based battery safety and thermal runaway have further emphasized the need for advanced battery monitoring systems to ensure safe operation[103, 104].

The terminal voltage of Li-ion battery energy storage varies with multiple parameters including state of charge (SOC) and mode of operation. Hence, utility-scale

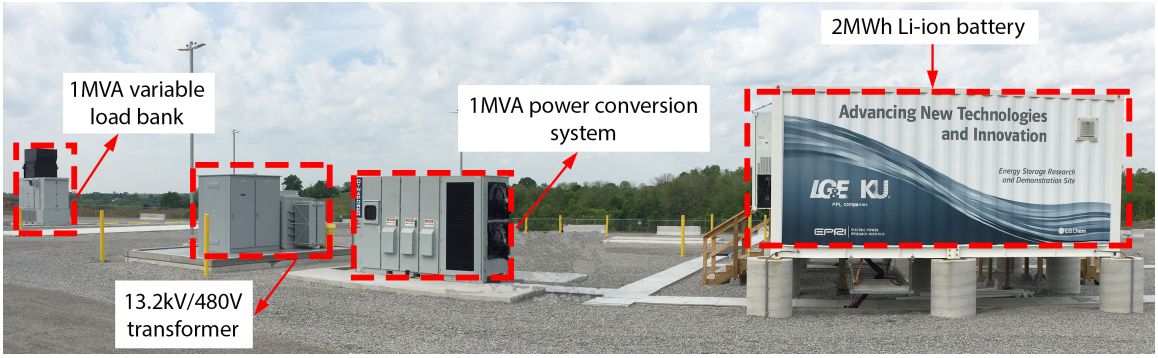

Figure 4.1: An example battery energy storage system (BESS) setup including a 1MVA bidirectional inverter, 2MWh battery system distributed in two containers(one obscured by the other), and an advanced SCADA facility, which is not shown. The 2MWh battery system incorporates 4,760 cells (20 racks or 340 modules) connected in series and parallel to meet power conditioning devices requirements.

BESS may see variations over 200V in their dc terminal voltage during regular operation [47]. Battery systems in some cases have been represented as constant voltage sources [105–107], or modeled as a controlled voltage source [108]. Furthermore, recent studies have focused on small-scale battery modeling with greater emphasis on single cell operations [109–111]. Other researchers have worked towards developing standardized procedures for the estimation of the parameters of a single cell. [112–115].

Contrary to conventional approaches, in which equivalent circuit parameters for battery cells were only extracted from laboratory setups and scaled to represent the parameters of a utility-scale battery system with multiple cells and BMS [116–118], the proposed approach accounts for the contributions of the BMS in cell voltage balancing and acknowledges the differences in the parameter of cells from the same manufacturer.

This chapter presents an approach for estimating the equivalent circuit parameters

of a utility-scale battery system and its sub-components using equipment typically available at installation sites. Additionally, the work emphasizes how the difference in parameters of cells within a battery system can lead to significant variations in terminal voltages and defines a metric for comparing the voltage performance of utility-scale battery models developed using select cell, module, or rack parameters.

Furthermore, this study introduces a multi-hour operation cycle that ensures battery voltage equilibrium for each charge or discharge procedure as opposed to the conventional quick pulse discharge cycles used for battery equivalent circuit parameter estimation [119, 120]. The proposed procedure benefits from measurements of the type recommended by the new Electric Power Research Institute (EPRI) BESS test manual [121], and may also serve as a possible extension to the initiative. This work builds upon the studies conducted in [46]. Additional contributions include sensitivity analyses to establish the impact of each parameter on the system performance, and comparison of the voltage variation of the battery system to equivalent circuit models from the parameters identified from specified racks, modules, and cells.

The technical details of the 1MW/2MWh battery system employed for this analysis are presented in this chapter. The battery operation cycles employed for the battery parameter identification and approach for validation are introduced. Also, the proposed test procedures adopted for the cell, modules, rack, and the battery system equivalent circuit parameter identification are also presented. The sensitivity analyses of the battery equivalent circuit components and the validation of the identified parameters are included in this chapter.

4.2 Field implementation setup

This study employs a utility-scale BESS, which includes a 2MWh battery system, a 1MVA bidirectional power conversion system (PCS), a 13.2kV/480V step-up transformer, and a 1MVA programmable load bank (Fig. 4.1). At the time of installation, this field system was one of the largest BESS testing facility in the US, whose capabilities have been highlighted through complex tests described in [121]. This unique setup includes advanced measurement devices capable of capturing voltage, current and power measurements at the dc-link, inverter ac terminal, and the point of common coupling, that are synchronized with the local time and logged at one-second intervals by the SCADA system.

In order to meet the ratings of the power conditioning device, the experimental battery system includes 20 racks, which are equally distributed between two identical containers. A rack includes 17 LG Chem M48126P3B1 battery modules, each with 14 Li-ion cells and rated for 126Ah at 51.8V nominal voltage. This battery system also employs a BMS, whose function includes the supervision of cell performance and balancing the SOC across all cells. The BMS provides additional details on the battery system and sub-component state including; the measured terminal voltage of all the cells, modules, and racks; the terminal current for each rack; and the calculated SOC of individual modules, racks, and entire battery system.

The PCS is a 1MVA Dynapower bidirectional two-level converter, which may be operated at 740-1150V dc-link voltage while maintaining a constant 480V three-phase voltage on the ac side. For the purpose of carrying out multiple discharge tests with

reduced grid disturbance and enable BESS operation in the isolated mode, the system is equipped with a 1MVA, 480V three-phase Simplex programmable large size load bank, which is capable of absorbing up to 1MW resistive power and sourcing/absorbing reactive power up to 600kVAr at 5kVA load steps (Fig. 4.1).

4.3 Review of EPRI battery test procedures

The Electric Power Research Institute (EPRI) recently released an energy storage test manual aimed to support improved understanding of large scale energy storage system technical characteristics relevant to utility requirements [121]. This manual defines consistent procedures and metrics to objectively compare and track the performance of a BESS. This study reviews the important tests described by the EPRI test manual for BESS, with detailed implementation of the prioritized procedures.

The BESS may be divided into two major sections; the energy storage unit and the power conditioning system. The energy storage unit consists of the battery unit, which is a connection of multiple cells in series and parallel; the battery management system, which includes the HVAC for temperature regulation and fire suppression system. The power conditioning device includes the bidirectional dc/ac converter, utility power transformer, ac and dc circuit breakers and the overall system management.

The energy storage integration council (ESIC) at EPRI proposed multiple charge and discharge test cycles for characterizing utility scale BESS. These cycles may be use to define the functionalities, performance and verify manufacturer specifications such as available energy, charge/discharge duration, round trip efficiency and self-discharge rate. For the purpose of improving accuracy during tests, it is recommended that the

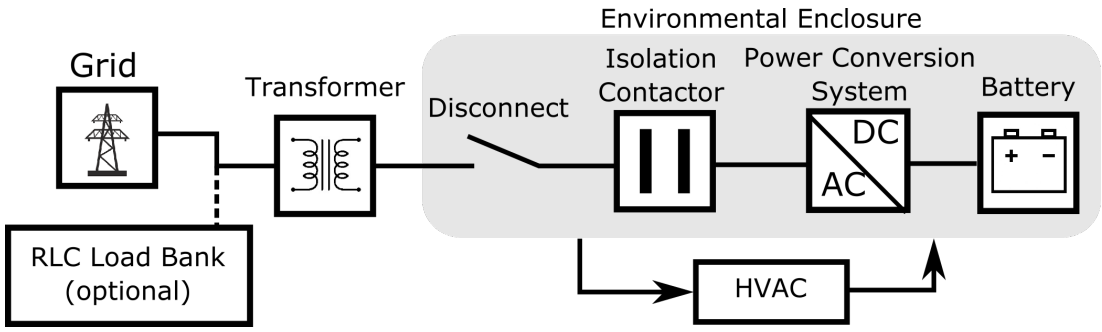

Figure 4.2: An example battery energy storage system (BESS) setup with the battery unit directly connected to the dc-link of the bidirectional converter. The BESS may be isolated from the utility grid and connected to the available programmable load bank during the discharge tests

BESS environmental enclosure is maintained at 23°C or manufacturer's recommended operating temperature and a minimum of 10 minutes rest time is allowed between charge and discharge cycles.

In this approach, the BESS may be disconnected from the grid during battery tests and directly coupled to a variable load bank capable of absorbing up to 1MVA energy at 5kVA steps. This configuration with an optional load bank allows effective testing of the BESS without disrupting the operation of the power grid.

4.3.1 Available BESS energy

The amount of energy a BESS can provide or absorb is dependent on the energy rating of the battery unit and each component of the system for adequate operation. For the purpose of defining the available energy for large BESS, the EPRI test manual recommends charging and discharging it between the maximum and minimum SOC limits at different power ratings, while ensuring a maximum of one complete test cycle

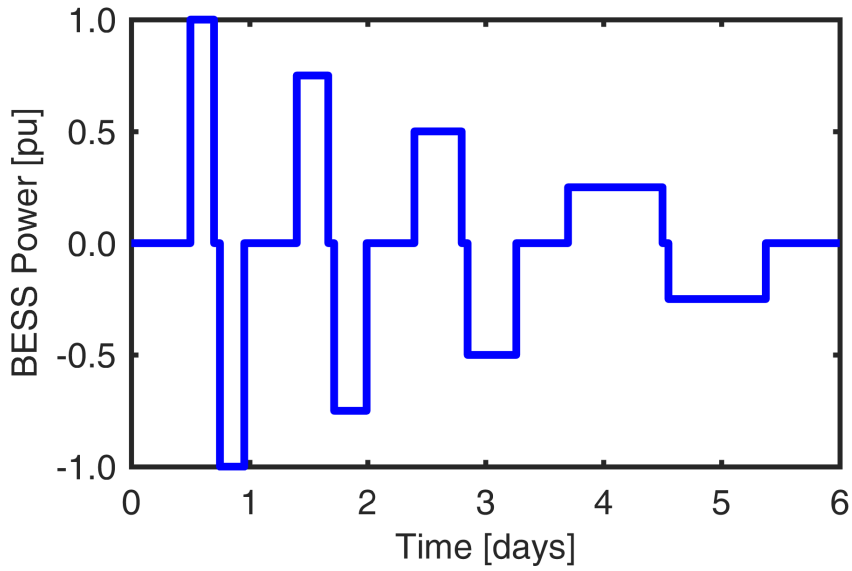

Figure 4.3: The schematic representation of the BESS real power duty cycle for determining operational and performance characteristics recommended by the EPRI test manual for large BESS. The BESS was charged/discharged at 100%, 75%, 50%, and 25% of its rated power in other to verify manufacturer specifications.

per day (Fig. 4.3). The available charge/discharge energy may be computed as:

$$E_{chg(dchg)} = \frac{1}{n}\sum_{1}^{n}(E_{Cn(Dn)} \pm E_{ACn(ADn)}), \tag{4.1}$$

where, E_{chg} and E_{dchg}, are the available charge and discharge energy, respectively; n is the number of complete cycles considered; E_{Dn} and E_{Cn}, is the energy at the point of common coupling (PCC) calculated as an integral of the metered power for n discharge and charge cycle, excluding energy for auxiliary loads, respectively; E_{ADn} and E_{ACn}, is the summation of energy from all auxiliary devices required to maintain BESS operation during n discharge and charge cycles, respectively.

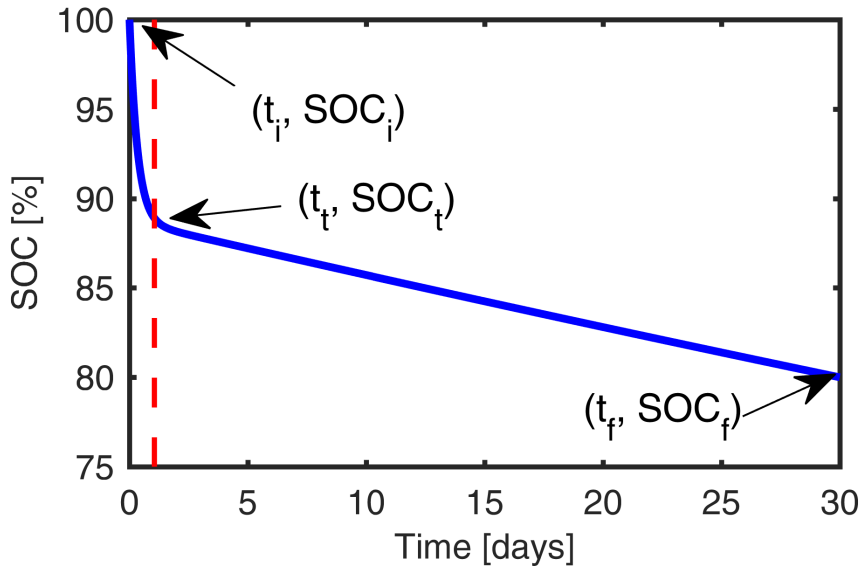

Figure 4.4: The schematic representation for an example SOC variation due to self discharge based on concept described in the EPRI test manual. The self discharge rate is highest at the first 24h after full charge and then tapers off to a lower somewhat constant rate.

4.3.2 Charge/discharge duration

The rated continuous charge duration for large BESS described by the EPRI test manual is the amount of time required to charge it from minimum SOC to maximum at rated power and vice versa for discharge duration. The real power schematic in Fig. 4.3 at unity power factor may be used to determine the battery charge duration, considering only the duration, where the charge/discharge power is within ±2% of the rated power.

4.3.3 BESS round trip efficiency

The round trip efficiency (RTE) of an energy storage is the fraction of the energy used to charge the BESS that is available for dispatch. Apart from providing information concerning the energy available, knowledge of the RTE can also be used

to monitor the performance of the BESS as well as its individual components. The percentage RTE may be computed as:

$$RTE(\%) = \frac{1}{n}\sum_{1}^{n}\frac{E_{Dn} - E_{ADn}}{E_{Cn} + E_{ACn}} \cdot 100. \tag{4.2}$$

When calculating the system RTE at the dc bus, E_{ACn} and E_{ADn} should be represented as the summation of energy from all auxiliary devices on the battery unit alone required for effective BESS operation during charge and discharge, respectively.

4.3.4 Self-discharge rate

The phenomenon, where the internal chemical reactions within a battery unit causes a reduction in its stored charge without any connection between its terminals is know as self-discharge. The knowledge of the self-discharge rate (SDR) for large scale BESS will provide the utility companies information regarding the amount of charge energy available in the battery and the ability to schedule charge/discharge cycle for maximum RTE.

The SDR for large BESS may be classified into transient (SDR_t) and long-term (SDR_{LT}) SDRs. In order to estimate these values, the EPRI test manual recommends charging the BESS to maximum SOC and leaving it in shutdown mode for at least 7 days while monitoring its SOC (Fig. 4.4). The transient period refers to the partly exponential decay period in the battery SOC at the beginning of the test, where the SDR is maximum. The BESS SDR may also be computed by discharging it to its minimum SOC after the transient and long-term SDR period and recording the Watt-hour (Wh) discharge at the dc link. The expression for the transient SDR using

the both methods is given as:

$$SDR_t = \frac{SOC_i - SOC_t}{t_t - t_i} = \frac{Wh_i - Wh_t}{Wh_i * t_t}, \tag{4.3}$$

where t_i and t_t, are the test start time and intermediate transient time, respectively; SOC_i and SOC_t, are the battery SOC corresponding to times t_i and t_t, respectively; Wh_i and Wh_t, represent the watt-hours discharge before the test and after the transient discharge, respectively. The value for SDR_{LT} is computed over the t_t and the end of analysis time, t_f. It is recommended to repeat the test for variations of SOC_i for the battery full characterization.

4.4 Proposed test procedures and measurements for the battery system

The parameters of a battery cell vary with different factors including, temperature, state of health, state of life, depth of discharge, and SOC. Cells within a large battery system have unique characteristics and parameters even if they are identical models from the same manufacturer. Furthermore, in large multi-MW BESS, the cells are subjected to different operational conditions and load due to the presence of the BMS, which is employed for protection, monitoring, and SOC balance across all the cells. Hence, for the purpose of modeling a large battery, simply scaling the equivalent circuit parameters of a single cell may not be sufficient to represent the system accurately.

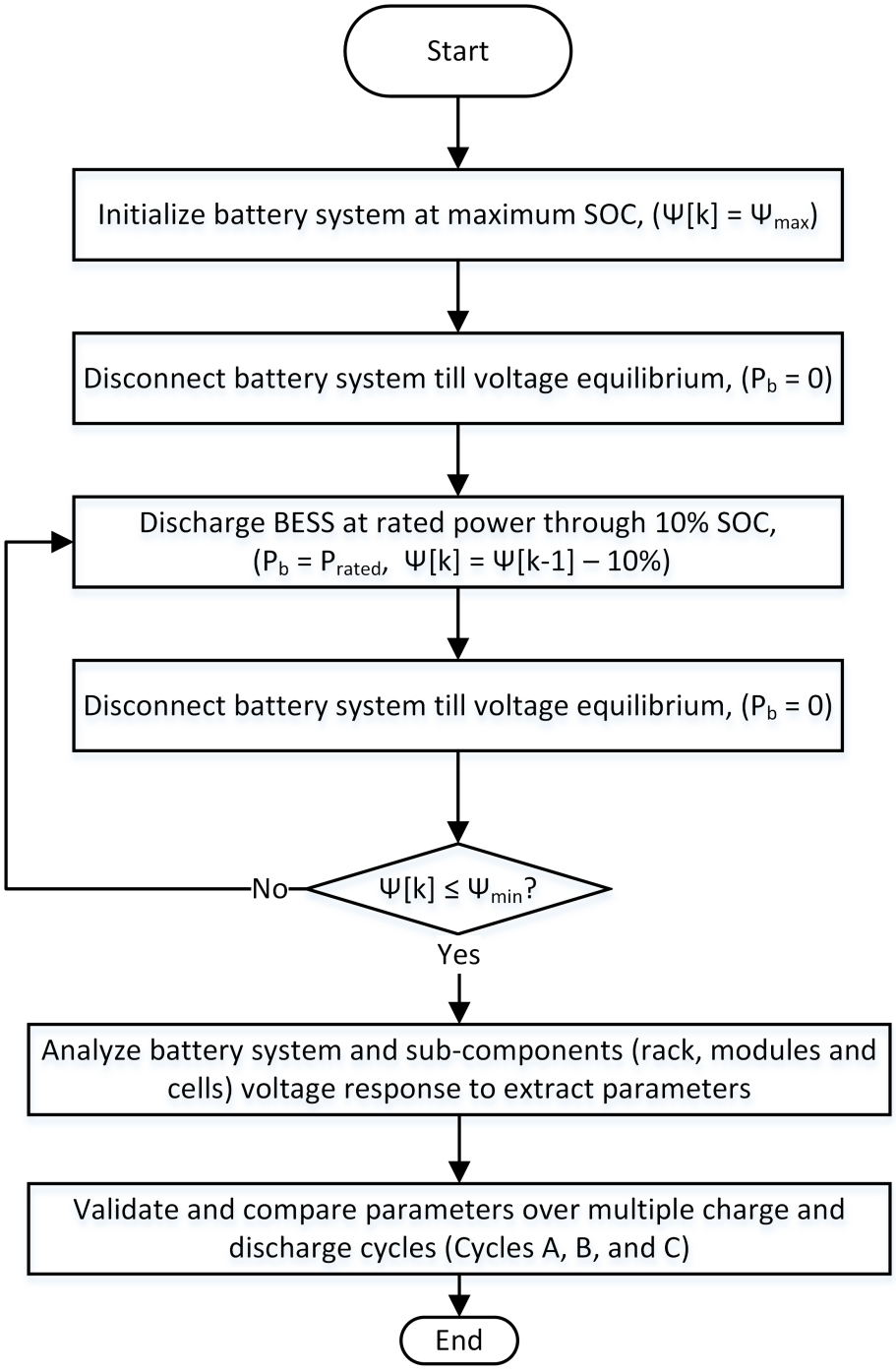

Figure 4.5: Flowchart for the experimental procedures employed in the proposed parameter extraction. The battery system is open-circuited or kept in the "float mode" in between tests in order to ensure voltage and chemical equilibrium among all cells.

The experimental setup includes multiple advanced measuring and protection devices capable of capturing and recording high-resolution voltage, current, and SOC measurements from each cell, module, rack, and the entire BESS. This approach assumes the battery system and its components can be subjected to similar charge and discharge cycles to estimate their individual equivalent circuit parameters.

The sequence of testing begins with the initialization of the battery system at its manufacturer recommended maximum SOC, and afterward open-circuited for a long period to ensure chemical and voltage equilibrium (Fig. 4.5). The experimental BESS setup was subjected to multiple charge and discharge cycles and its responses including the measured battery system and sub-component terminal voltage and current, the BMS computed SOC, and the PCS real and reactive power were recorded. The battery system enclosed chamber was regulated at 23°C throughout all tests to ensure minimum temperature variation between system cycles and battery sub-components.

For this example utility-scale battery system, the recommended minimum and maximum SOC limits from the manufacturer are 5% and 95%, respectively. At the time of this research, the standard time for a utility-scale battery system to reach equilibrium had not been described. Hence, a rest period of 8h before tests and 2h after each pulse operation is proposed for the battery system based on voltage response observations. The BESS operation and voltage response were analyzed and validated over three charge/discharge cycles described as follows.

Cycle A: This cycle is used for the main parameter extraction and validation. From the system reported maximum SOC, the BESS was continuously discharged at rated power through 10% SOC and operated in the float mode for 2 hours in order

to allow the battery system to approach equilibrium [121]. The float mode operation enables the battery system to approach chemical equilibrium while maintaining it at reference SOC by trickle charging at a rate equal to its self-discharge. This pulse discharge procedure was repeated until the system SOC reached the minimum. Conventional approaches require pulse discharging the battery cell at constant current. The proposed procedure is adapted to the equipment typically available at a utility-scale BESS, and therefore, the PCS is controlled for pulse discharging the battery based on a power command. In this approach, Cycles B and C are proposed for validation of the parameters identified through Cycle A.

Cycle B: This cycle is based on the exemplary performance and functionality test cycle described in [121] for characterizing the energy storage system. In this cycle, the BESS was initialized to the manufacturer recommended maximum SOC and left in the float mode till the battery system is presumed to have reached chemical and voltage equilibrium. The battery is then continuously discharged at rated power till minimum SOC, and promptly charged back to maximum SOC before being discharged once again at rated power till 50% SOC. The BESS is then left in float mode for approximately 2 hours before the next cycle at 75% capacity of rated power. The procedure is repeated for 50% rated power and all relevant system component parameters were measured and recorded.

Cycle C: The field implemented BESS setup is co-located with multiple generation resources including solar, natural gas combustion turbines, hydropower plants, and coal-fired units with over 1GW of combined net-generation capacity. In this cycle, the BESS is operated in the autonomous frequency response mode, in which

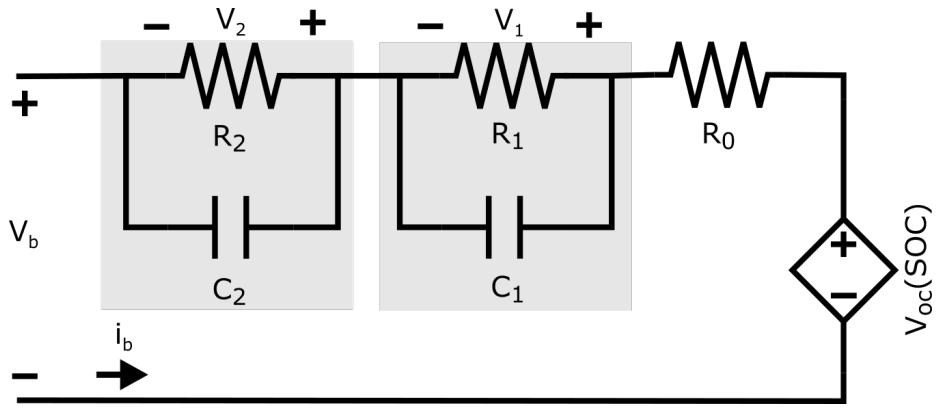

Figure 4.6: Equivalent circuit model for the battery system and its sub-components (racks, modules and cells) used for the study. Each parameter corresponds to the combination of cells connected in series and parallel.

the battery charges when the frequency exceeds the reference value and discharges otherwise. Due to the reduced frequency variation near the grid-connected BESS, the response sensitivity was increased such that the battery addresses deviations greater than 0.005Hz and supports the grid at rated power for deviations above 0.05Hz based on the specified droop control.

4.5 Battery system, racks modules and cells parameter extraction

A battery cell may be represented as a controllable voltage source (v_{oc}) connected in series to a resistance (R_0) and multiple RC branches (R_1, R_2, C_1 and C_2). In this approach, it is assumed that the same type of equivalent circuit can be used to represent the battery system, rack, module, and cell, with the parameters modified accordingly (Fig. 4.13). The impact of parameters such as the number of charge/discharge cycles, depth of discharge, state of health, and temperature are beyond the scope of this study. Hence, the voltage response of the battery system and its sub-components are

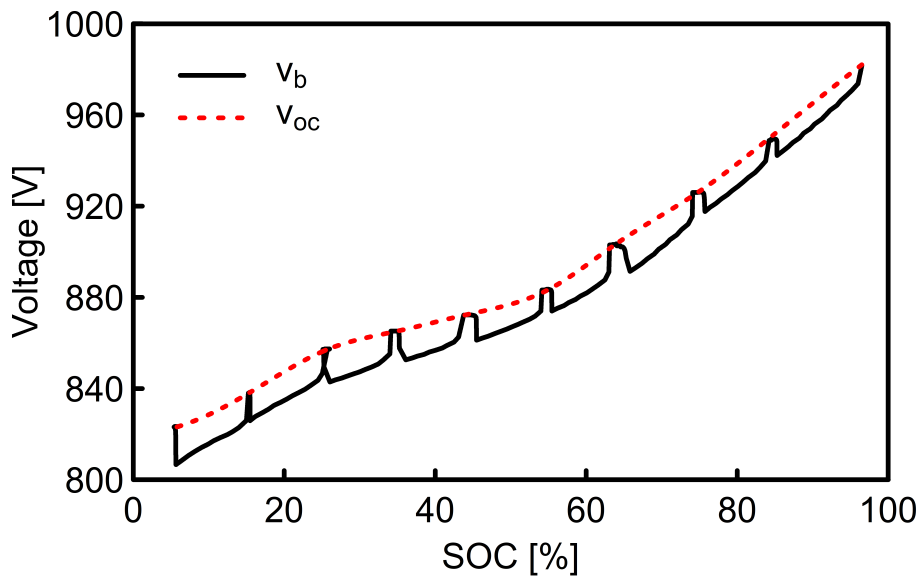

Figure 4.7: Battery system open circuit voltage. The BESS was pulse discharged (Cycle A), and the maximum dc terminal voltage (v_b) for defined SOC ranges when the output current approaches zero were used to estimate its open-circuit voltage (v_{oc}).

represented as functions of SOC. It may be noted that the parameter value has been demonstrated to be minimally impacted by the SOC when the battery is operated between 5-95% [122–124].

The battery system terminal voltage, v_b during discharge may be described as:

$$v_b(t) = v_{oc} - i_b\, R_0 + i_b\, R_1\, e^{-\frac{\Delta t}{R_1 C_1}} + i_b\, R_2\, e^{-\frac{\Delta t}{R_2 C_2}}. \tag{4.4}$$

$$v_b(t) = v_{oc} - i_b\, R_0 - v_1(t) - v_2(t), \tag{4.5}$$

where, v_{oc}, is the battery open-circuit voltage; i_b, the battery dc output current; v_1 and v_2 , the voltages across the RC branches 1 and 2, respectively and t, the discharge duration. The voltage response of the battery system and its sub-components during BESS pulse discharge operation (Cycle A) were analyzed and used to estimate

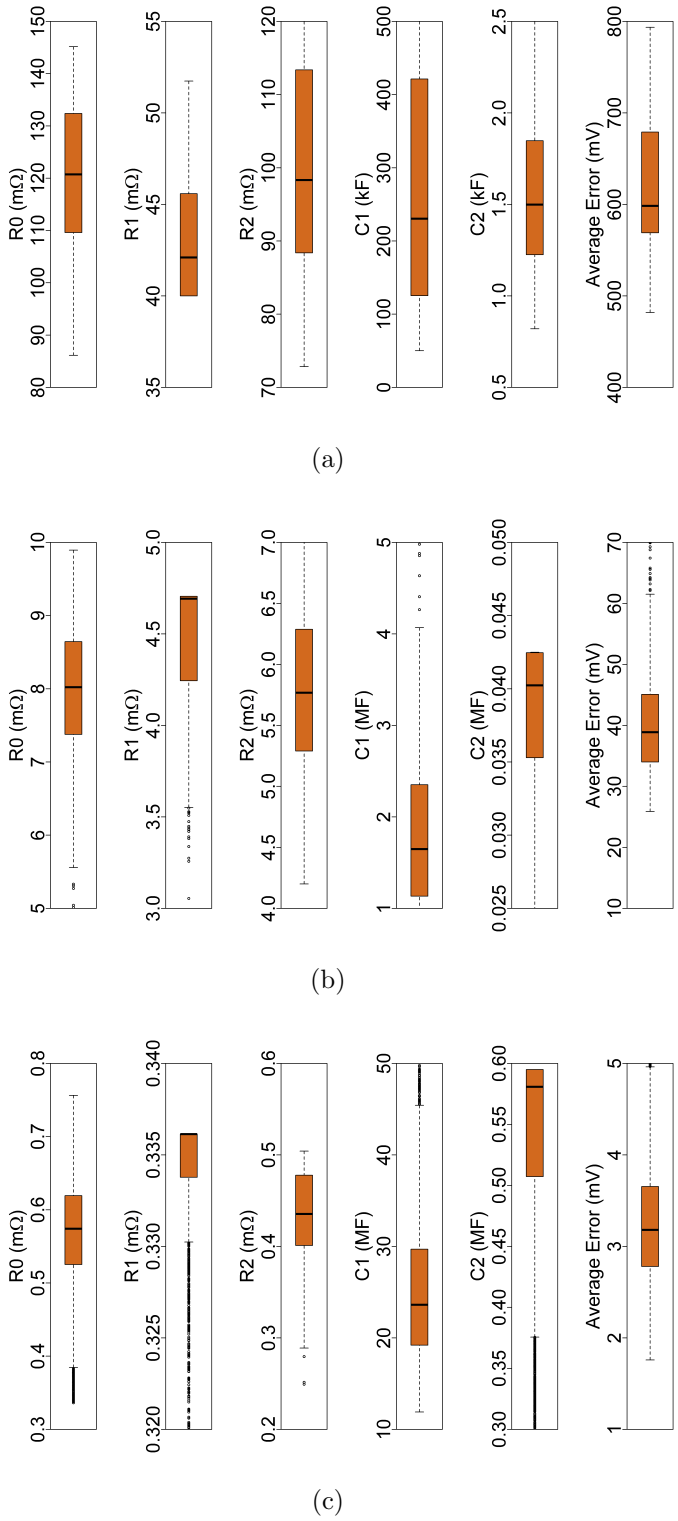

Figure 4.8: The variation of the equivalent circuit parameters for the battery systems component extracted through measurements for all (a) 20 racks, (b) 340 modules, and (c) 4,760 cells. The results illustrate typical variations within battery system sub-components from the same manufacturer.

the corresponding equivalent circuit parameters. From (4.15), the battery terminal voltage approaches its open-circuit value as the output current tends to zero and is expressed as:

$$v_{oc}(t) = \lim_{\substack{i_b \to 0 \\ \Delta t \to \infty}} v_b(t). \tag{4.6}$$

In this approach, the battery and sub-components dc terminal voltages, v_b, when the current is nearly zero during Cycle A were isolated and divided into 20 SOC class intervals of the same range. Due to the influence of external parameters such as self-discharge rate and battery trickle charge, terminal voltage reduction may also be observed during open-circuit conditions. The maximum dc voltage for each bin when the output current is zero is identified as the open-circuit voltage for the reported SOC and termed as:

$$v_{oc}(\psi_i) = \max_{i_b=0}[v_b(\psi_l), v_b(\psi_u)], \qquad \psi_l \leq \psi_i \leq \psi_u \tag{4.7}$$

where, ψ_i represents the SOC corresponding to the reported class interval maximum voltage, ψ_l and ψ_u the lower and upper boundary of the select class interval, respectively. For Cycle A evaluation, only bins where the battery output current is zero were analyzed. The defined points were fit to establish the battery system open-circuit voltage relationship with SOC and a similar procedure was employed for all its racks, modules, and cells (Fig. 4.7).

This approach employs an artificial computation intelligence program to estimate the best values of the resistance and capacitance that can be applied to (4.13) for an accurate estimation of the battery terminal voltage. The fitness function is defined as the absolute value of the difference between the reported battery terminal voltage

and the corresponding calculated value at each data point of Cycle A. Hence, the particle swarm optimization problem is formulated as follows:

$$\min_{x} F(x) = \min_{x} \sum_{k=1}^{M} |v_b^*(k) - v_b(k)| \quad x \in X \tag{4.8}$$

$$x = (R_0, R_1, R_2, C_1, C_2) \tag{4.9}$$

where $F(x)$ is the objective function extracted from (4.13); k, the index of the data sample; $v_b^*(k)$, the measured battery voltage at the kth data sample; $v_b(k)$, the calculated battery voltage at the kth data sample; M, the number of data samples; x, is the vector with all the battery parameters; and X, is the space of solutions.

A satisfactory average voltage error less than one-percent was reported for Cycle A when the battery models developed using a combination of the established open-circuit voltage and SOC relationship with parameters retrieved from the optimization process for the battery system all its sub-components were compared to the reported values. Even though all the cells that make up individual modules, racks, and the entire battery system are from the same manufacturer, a significant disparity can be observed in their estimated parameters (Fig. 4.8).

4.6 Parameters sensitivity analysis

In order to identify the most influential parameters affecting the accuracy of the battery equivalent circuit model presented in Fig. 4.13, a sensitivity analysis was conducted. A regression model was employed to relate the identified battery system

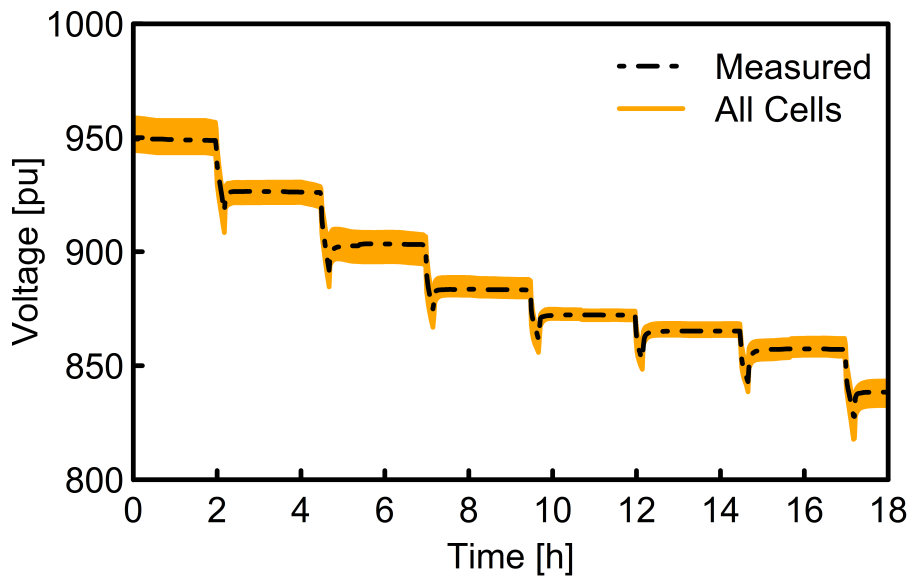

Figure 4.9: Voltage response for multiple battery system models developed as a scaled version of each individual cell.

parameters. The 2nd order polynomial function used is expressed as follows:

$$Y = \beta_0 + \sum_{i=1}^{d_\nu} \beta_i X_{Ci} + \sum_{i=1}^{d_\nu} \beta_{ii} X_{Ci}^2 + \sum_{i=1}^{d_\nu} \sum_{j=i+1}^{d_\nu} \beta_{ij} X_{Ci} X_{Cj} \ , \tag{4.10}$$

$$X_{Ci} = \frac{x_i - (x_{i,max} + x_{i,min})/2}{(x_{i,max} - x_{i,min})/2} \ ; \ i = 1, 2, ..., d_\nu, \tag{4.11}$$

where Y is the response parameter; β, the regression coefficient; d_ν, the number of factors, x_i, the ith input factor; and X_{Ci}, the normalized (coded) value of the ith factor. Factors may be normalized as shown in (4.10). $X_{Ci} = 0$ represents the specified values of the factors with the reference response, and β_0 is a representation of response parameter in this reference situation. β_{ii} and β_{ij} illustrate second order effects and interaction between the factors.

In this approach, the voltage responses of 15,625 equivalent circuit models for the

Table 4.1: Sensitivity analysis regression co-coefficients

Parameters	Average Error [pu] $\times 10^{-3}$	Max Error [pu] $\times 10^{-2}$
R_0	-0.09	1.10
R_1	0.07	-0.02
R_2	-0.04	-0.08
C_1	0.02	0.02
C_2	0.01	-0.36
v_{oc}	3.85	4.46

battery system with each parameter varying between ±10% of the extracted value were analyzed over Cycle A. The results of the sensitivity analysis with regards to the average and peak voltage error of the battery system are presented in Table 4.1. The main takeaways from the study are as follows:

1) The open-circuit voltage of the battery is the main parameter that influences the voltage response of the system

2) Depending on the cycle analyzed the RC branch parameters are the least significant

3) The battery series resistance, R_0 has an observable effect on the maximum voltage error recorded.

4.7 Battery system parameter validation and comparison

The sequence of validation was initiated with a comparison of the multiple battery system models developed as a scaled version of all 4,760 cells in the considered 1MW/2MWh setup. For validation purposes, this approach assumes that battery

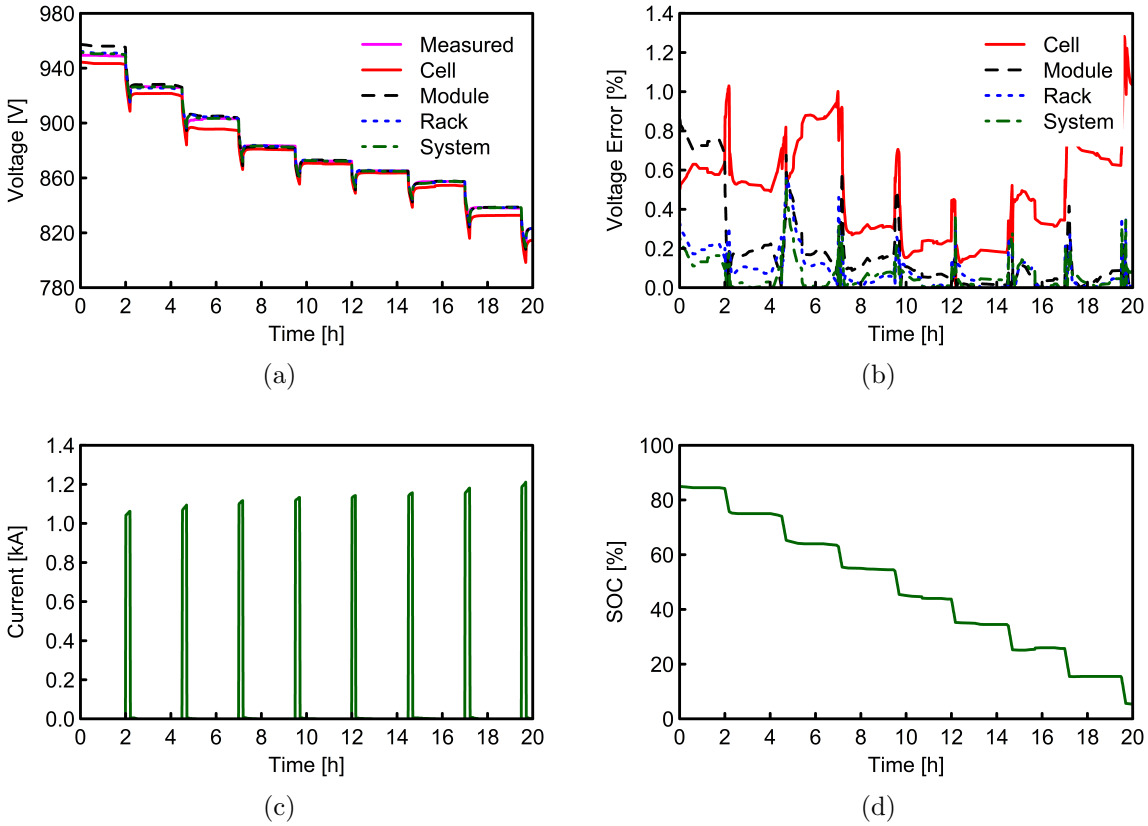

Figure 4.10: The BESS during rated power pulse discharge from maximum to minimum SOC showing: (a) The experimental and simulated battery system terminal voltage variation for the system and sub-components, (b) the percentage voltage error, (c) the discharge current, (d) and the SOC variation. The battery discharge current increases to maintain constant pulse discharge power as voltage decreases with SOC.

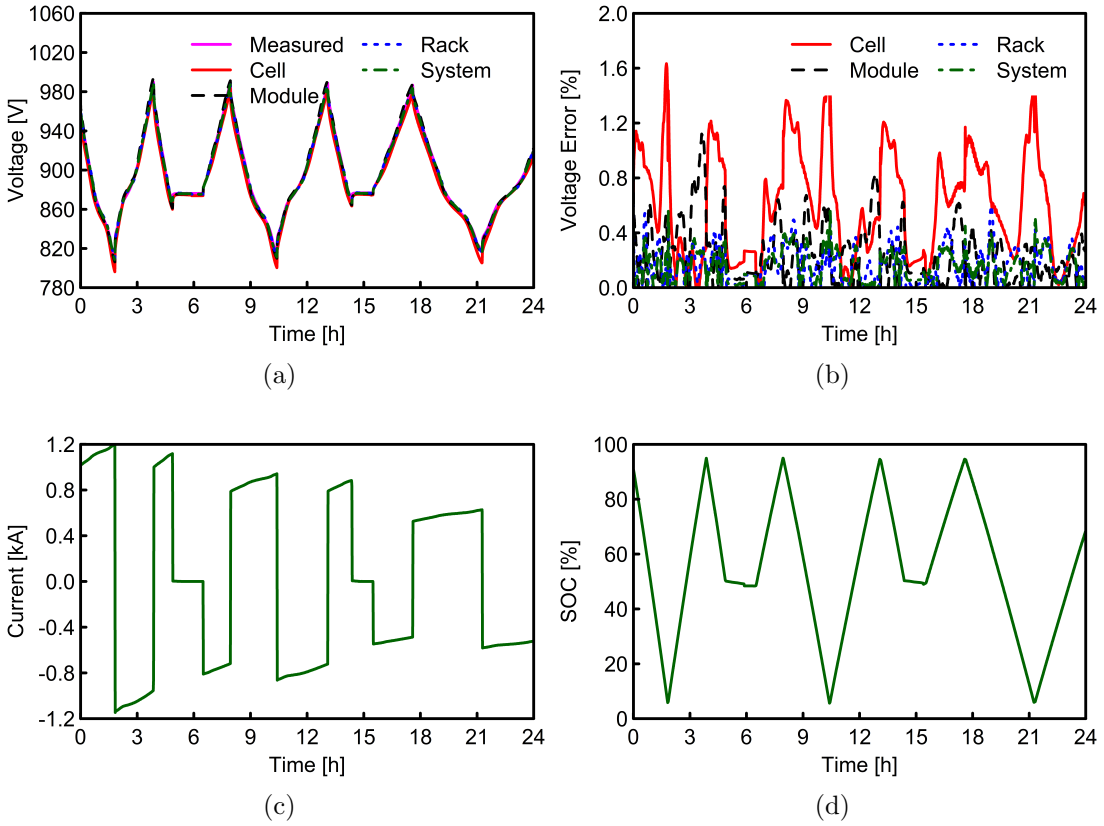

Figure 4.11: The BESS during dynamic charge and discharge between multiple SOC levels at 100%, 75% and 50% power rating ($CycleB$) showing: (a) The experimental and simulated battery system terminal voltage variation, (b) the percentage voltage error, (c) the discharge current, (d) and the SOC variation. The average error for the system and selected sub-components were considered to be within acceptable limits and the maximum percentage error was reported for the representative cell.

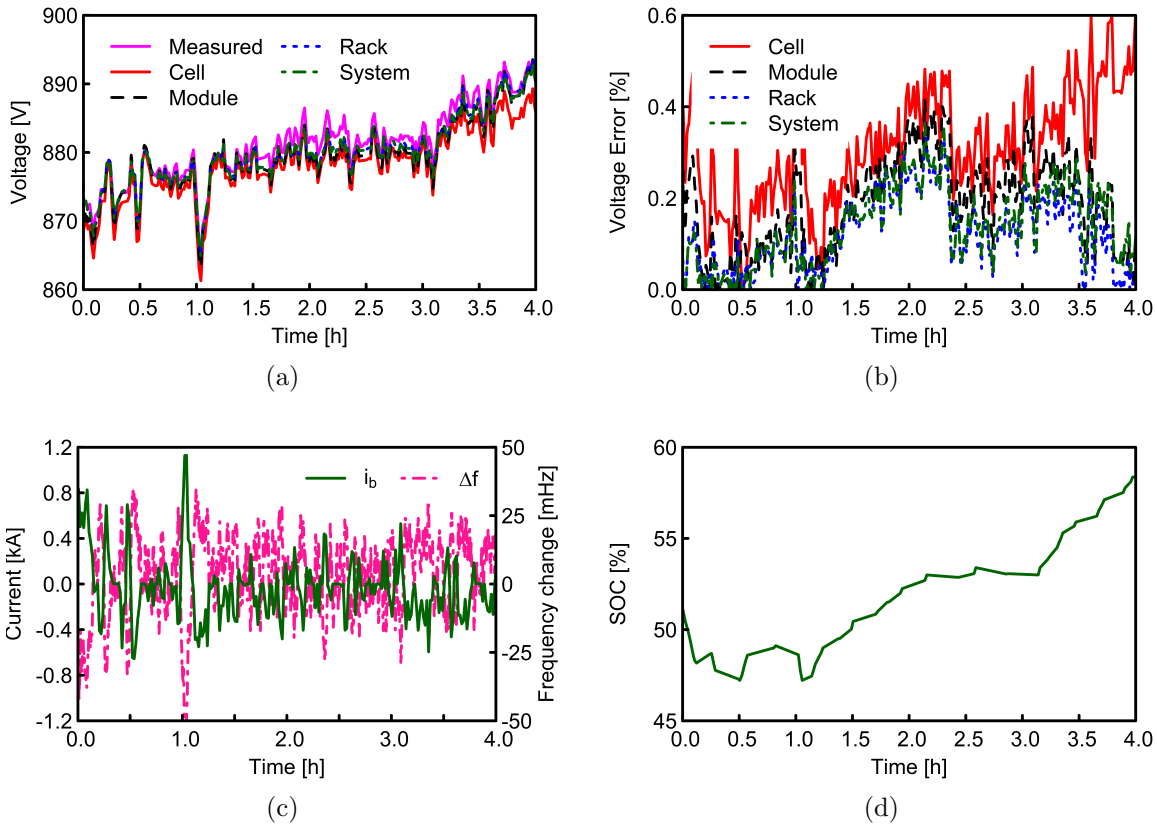

Figure 4.12: The BESS during automated grid frequency response, showing: (a) The experimental and simulated battery system terminal voltage variation for the battery system and sub-components, (b) the percentage voltage error, (c) the discharge current(i_b) and grid frequency deviation (Δf), (d) and the SOC variation. The BESS sensitivity was modified such that the system responds to frequency deviations about 5mHz.

sub-components contribute equal currents and voltages to represent the entire battery system. Hence, each sub-component current is defined as a fraction of the total battery system current and the total amount of component strings in parallel, while the corresponding sub-component voltage represents a fraction of the total number of components in series per string(Table 4.2). The analysis showed that for the example setup considered, the average voltage error of a battery system modeled can vary up to 10V depending on the reference cell selected (Fig. 4.9). Also, the performance evaluation reported higher disparities in the simulated voltages at SOC greater than 50%.

The accuracy of a battery equivalent circuit for utility-scale systems does not only depend on the reference member of the sub-component but also the sub-level analyzed. In order to demonstrate this, the battery terminal voltage was derived using three scaling approaches: scaling the voltage from a) the cell; b) the module, and c) the rack levels, and compared with the terminal voltage predicted by the proposed method based on tests conducted at the battery level.

The terminal voltage predicted by the battery models developed using scaled parameters of the select combination of cell, module, and rack sub-components with the highest average error was evaluated through Cycle A (Fig. 4.10). It can be observed that the simulated voltage responses of these models developed using sub-component parameters were within acceptable limits, which may be attributed to the presence of the BMS ensuring that all measured cell voltages are typically within

3mV variation. In this approach, the percentage voltage error was calculated as:

$$\% \text{ Error} = \frac{|V_{exp} - V_{sim}|}{V_{exp}} \times 100 \tag{4.12}$$

where V_{exp} and V_{sim} represent the measured and simulated battery system voltage responses, respectively. It can be observed that the recorded voltage variation of the battery system model developed from scaling the cell parameters has lower accuracy compared to the system alternative, which had less than 0.1% average error for the cycle (Table 4.3).

The performance of the developed battery models is validated for steady-state operation, as well as grid frequency regulation. For the steady-state case, the simulated voltage variations of the battery sub-component models were compared with the measured BESS dc-link terminal voltage when subjected to Cycle B power variation (Fig. 4.11). In this operation cycle, the influence of the RC branch parameters is minimal, and the recorded voltage error is primarily due to the open-circuit voltage and resistances. For this validation cycle, the equivalent circuit model developed as a function of the system parameters has the minimum mean voltage error.

Battery energy storage systems may be employed for grid frequency regulation, during which active power is provided in response to changes in frequency. The variations in terminal voltage predictions for the developed equivalent circuit models were further evaluated through the frequency response operation described in Cycle C. The fast charge and discharge operations through this cycle resulted in minimal SOC variation and increased voltage error for the system and rack models, which can be observed at SOC ranges between 53-54% (Fig. 4.12). It is however important

Table 4.2: Sub-components configuration for field implemented 1MW/2MWh battery system

Sub-components	Springs in parallel	String length
Cells	20	238
Modules	20	17
Racks	20	1

Table 4.3: The battery system percentage voltage errors using equivalent circuit parameters at different sub-component levels.

		Mean [%]	Max [%]
Cycle A	System	0.06	0.55
	Rack	0.09	0.58
	Module	0.18	0.87
	Cells	0.49	1.28
Cycle B	System	0.16	0.98
	Rack	0.17	1.11
	Module	0.25	1.53
	Cells	0.60	1.71
Cycle C	System	0.14	0.51
	Rack	0.12	0.52
	Module	0.18	0.45
	Cells	0.31	0.61

to recognize that average voltage error for the system equivalent model and sub-components are all less than 0.4% and within an acceptable range.

4.8 Battery bank model in PSCAD/EMTDC

A battery cell is generally modeled as a controllable voltage source connected in series with a variable resistor and multiple RC branches (Fig. 4.13). The characteristics of a battery vary with its chemical and physical parameters such as temperature, state of charge (SOC), state of health and the number of cycles. For simplicity, only the variation due to the battery SOC is being considered in this approach. The

battery SOC may be represented as:

$$\gamma(\%) = \gamma_i(\%) - \frac{100}{C_{Ah} \cdot 3600} \int_0^t i_b dt, \tag{4.13}$$

where γ and γ_i represents the percentage final and initial battery SOC, respectively; C_{Ah}, the battery rated capacity in Ampere-hour; i_b, battery output current and t is the time. C_{Ah} is multiplied by 3600 in order to convert it to Ampere-second. The terminal voltage of the battery bank may be represented as:

$$v_b(t) = v_{oc} - i_b(t)R_0 - v_{RC1}(t) - v_{RC2}(t), \tag{4.14}$$

and the RC branch voltages, $v_{RC1}(t)$ and $v_{RC2}(t)$ may be found from their first derivatives, $\dot{v_{RC1}}(t)$ and $\dot{v_{RC2}}(t)$ from the following,

$$\dot{v_{RCn}}(t) = \frac{1}{C_n}\left(i_b(t) - \frac{v_{RCn}(t)}{R_n}\right), \qquad \text{for n = 1 and 2,} \tag{4.15}$$

where v_b represents the battery terminal voltage; V_{oc}, the battery open-circuit voltage; R_0, the series resistance, and R_n and C_n, the resistances and capacitances for the nth battery RC branch.

An equivalent battery bank model was developed in PSCAD/EMTDC based on (4.13)-(4.15). This model mathematically calculates the voltage across R_0 and the RC branches, which is then subtracted from open-circuit voltage to obtain the battery terminal voltage. The terminal voltage is used to regulate a controllable dc source, in order to model the voltage response of the battery and capture its dynamic behavior (Fig. 4.14). The estimated single-variable functions for each of the battery equivalent

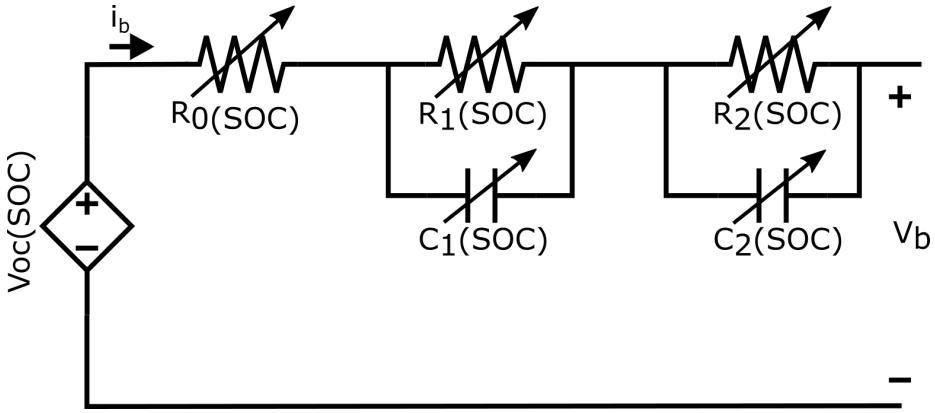

Figure 4.13: An equivalent circuit diagram for a single battery cell. In this approach, for simplicity, parameters such as cell temperature, number of charge and discharge cycles, self-discharge and cell state of health are neglected.

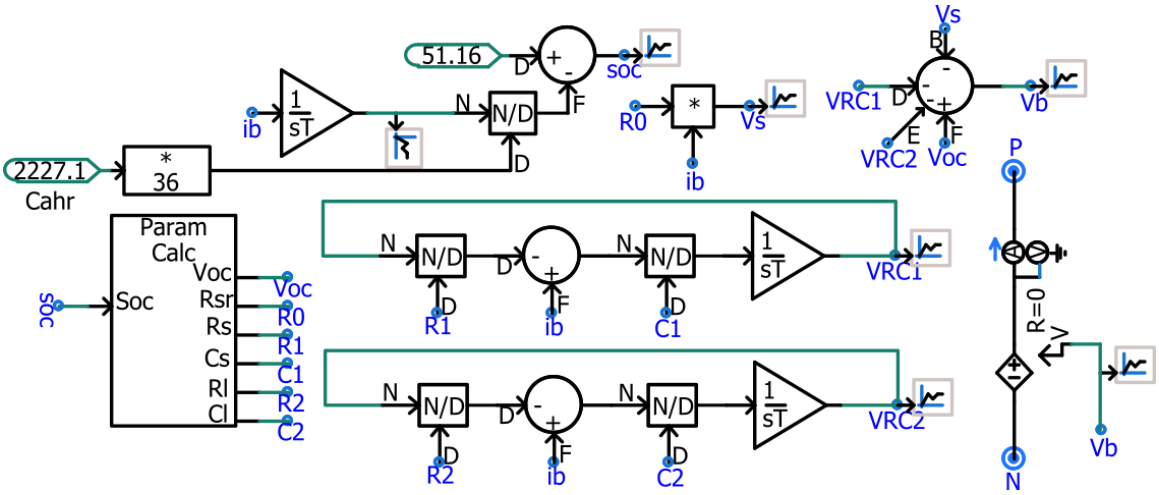

Figure 4.14: The developed runtime equivalent circuit for a utility scale 1MW/2MWh battery bank in PSCAD/EMTDC software.

circuit parameters were thus retrieved from the experimental test and described as:

$$v_{oc}(\gamma) = 10.16 \cdot \exp^{-3.389 \cdot \gamma} 0.002081 \cdot \gamma^3 - 0.02149 \cdot \gamma^2 + 1.918 \cdot \gamma + 814.5, \quad (4.16)$$

$$R_0(\gamma) = 0.00584 \cdot \exp^{-0.088 \cdot \gamma} + 0.00558, \quad (4.17)$$

$$R_1(\gamma) = 30.9068 \cdot \exp^{-1.72223 \cdot \gamma} + 0.003434, \quad (4.18)$$

$$C_1(\gamma) = 8.66 \times 10^7 \cdot \exp^{-0.2416 \cdot \gamma} + 1.007 \times 10^6, \quad (4.19)$$

$$R_2(\gamma) = -4.23731 \cdot \exp^{-1.4753 \cdot \gamma} + 0.0015, \quad (4.20)$$

$$C_2(\gamma) = -6.68 \times 10^5 \cdot \exp^{-0.8311 \cdot \gamma} + 30379. \quad (4.21)$$

The *Param Calc* block in Fig. 4.14 is used to calculate the open-circuit voltage, resistor and capacitor values of the battery bank as a function of the SOC. This subsystem is modeled in PSCAD/EMTDC environment using arithmetic blocks that describes the mathematical relations presented in (4.16)-(4.21) (Fig 4.15).

In order to verify the proposed model, it was tested under the same conditions as the experimental measurements. The model is fed from a current source, whose output is identical to the measured dc current of the experimental unit. For the purpose of reducing the simulation time, the battery model was simulated on an

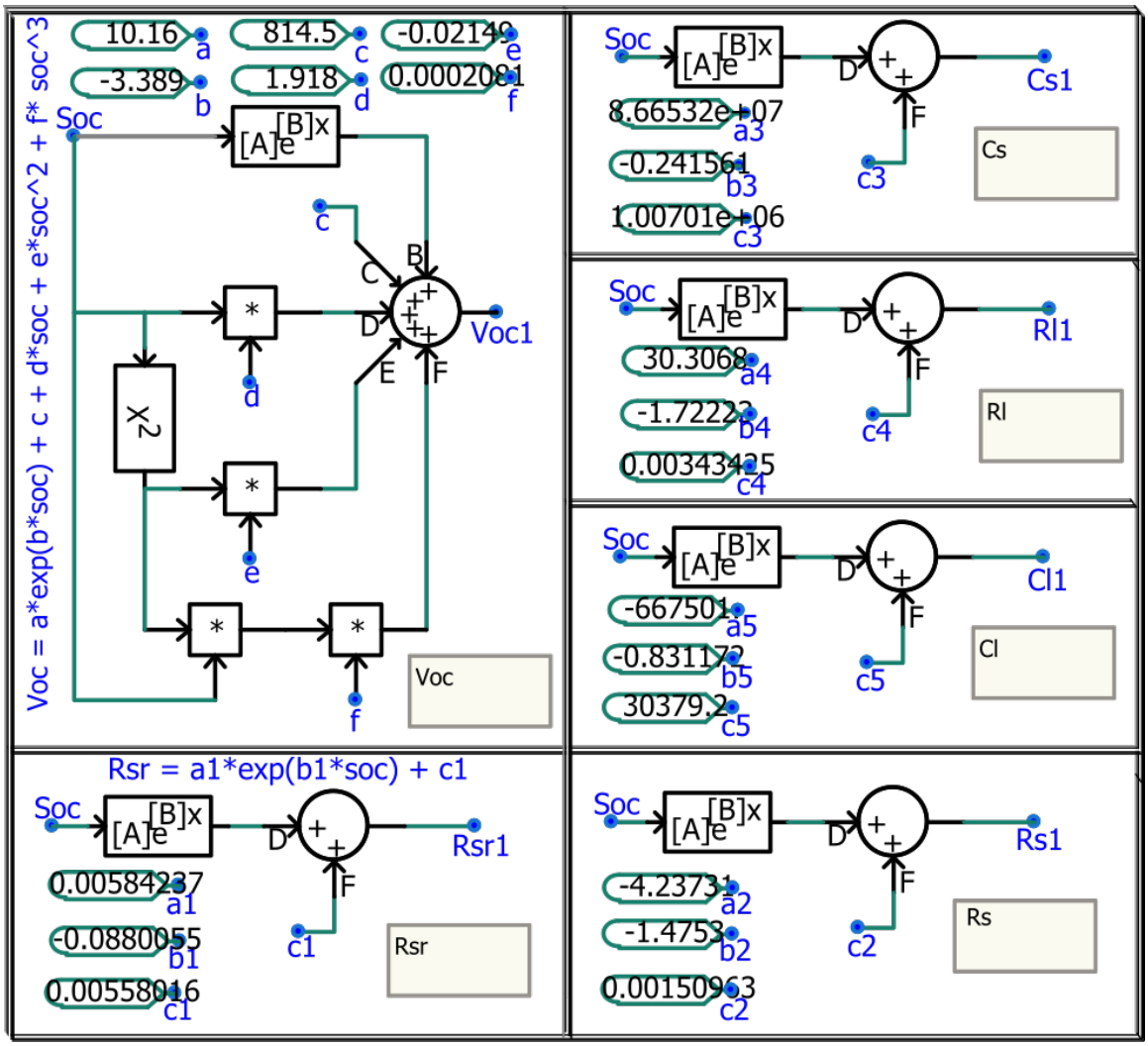

Figure 4.15: The estimation of equivalent circuit parameters in the PSCAD/EMTDC software. Best fit models relating the electric equivalent circuit parameters to the battery SOC were derived from experimental measurements on the LG&E and KU battery.

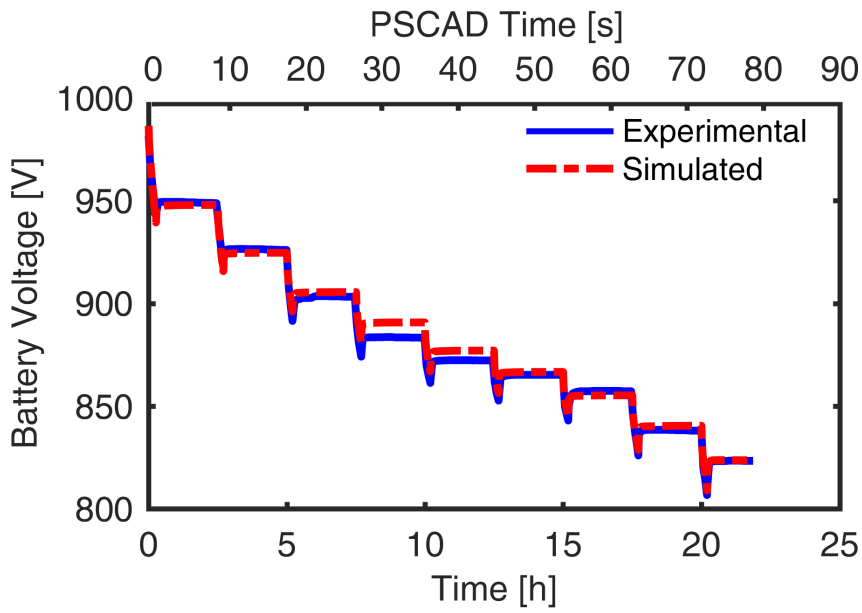

Figure 4.16: The battery terminal voltage variation during pulse discharge.

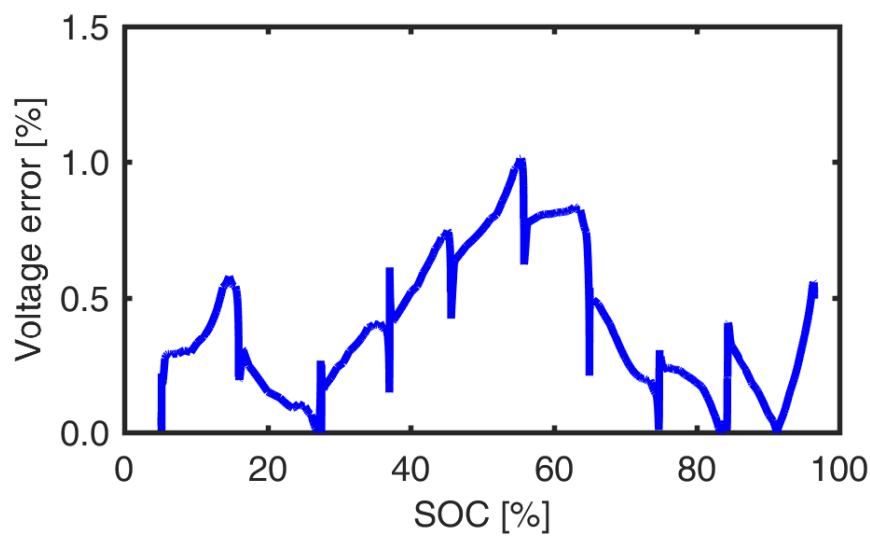

Figure 4.17: The variation of percentage error between the estimated and measured battery terminal voltages with the SOC. Based on the defined parameters, up to 99% accuracy in the estimated voltage is achievable.

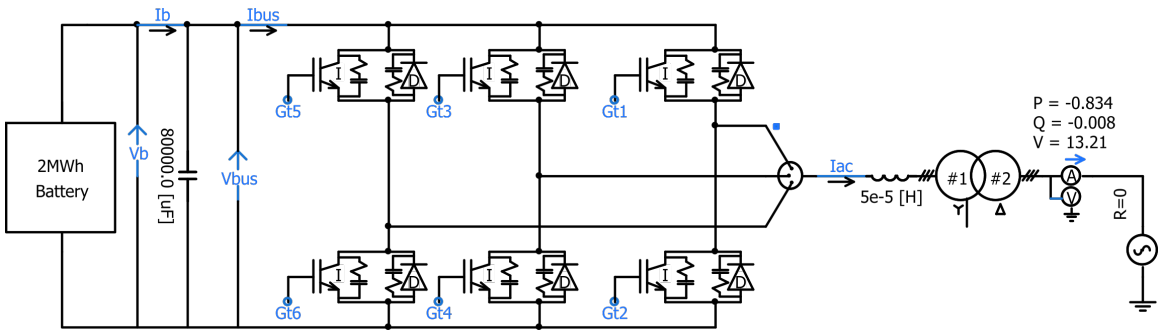

Figure 4.18: Schematic representation of battery energy storage system in PSCAD/EMTDC software. The system includes a 1MW/2MWh battery bank connected to the grid through a bidirectional power conditioning system and a 1MVA transformer.

accelerated time scale, α. Hence, the RC branch voltage expressions in (4.15) may be rewritten as:

$$v_{RCn}(\alpha) = \frac{1}{KC_n} \int \left(i_b(\alpha) - \frac{v_{RCn}(\alpha)}{R_n} \right) \cdot d\alpha, \text{ for n = 1 and 2,} \tag{4.22}$$

where $\alpha = Kt$, is the accelerated time, which is a multiple of the experimental time. For this approach, K was selected to be equal to 0.001. Also, (4.13) and (4.14) may be rewritten in terms of α. The terminal voltage of the equivalent battery bank model in PSCAD/EMTDC was compared with the experimental result for a pulse discharge of the battery from the maximum to minimum SOC, and an agreement between the results was established (Fig. 4.16). The developed battery bank model demonstrated an accuracy up to 99%, with the maximum error occurring around 50% SOC (Fig. 4.17).

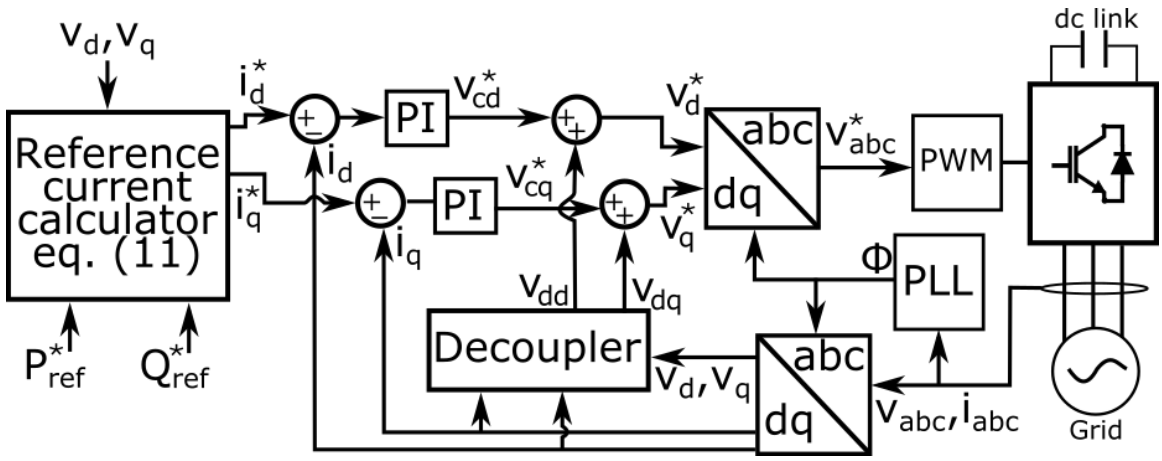

Figure 4.19: An example inverter control scheme, allowing independent control over the active and reactive power. P_{ref}^* and Q_{ref}^* represent the real and reactive reference powers, respectively.

4.9 Power electronics control

The BESS is modeled in PSCAD/EMTDC as the proposed equivalent battery connected to a two level bidirectional inverter. The BESS is connected to the grid, which is represented as a 13.2kV three-phase voltage source, via a wye-delta 480V/13.2kV transformer (Fig. 4.18). For this inverter, a decoupled scheme identical to [125], which allows the independent control of real and reactive powers is employed (Fig. 4.19). The $dq-$ rotating reference frame is aligned with the grid voltage using the transformation angle, ϕ, obtained from a phase locked loop. The inverter active (P_{ref}^*) and reactive (Q_{ref}^*) power references, may be set at the desired values, depending upon the operating mode, for example, frequency regulation, power smoothing and voltage compensation. These are used find the $dq-$ current commands using the following,

$$i_d^* = \frac{2}{3}\frac{P_{ref}^*}{v_d}, \qquad i_q^* = \frac{2}{3}\frac{Q_{ref}^*}{v_q}, \tag{4.23}$$

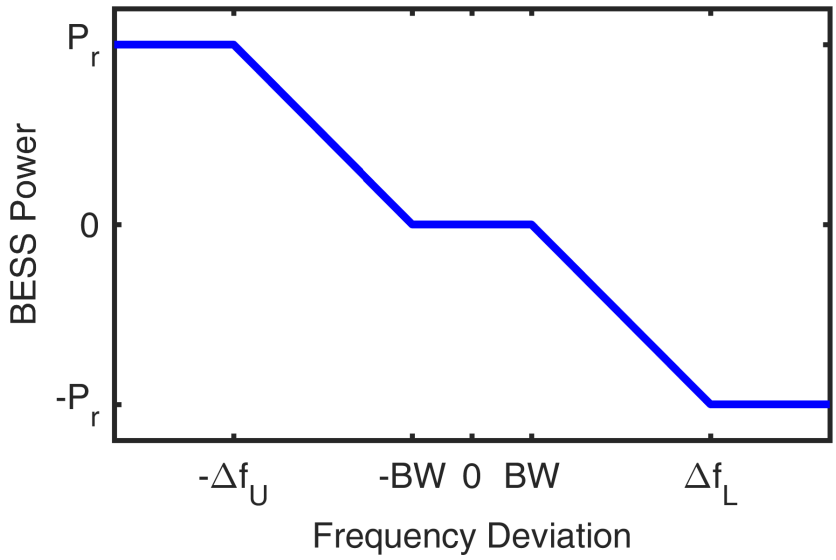

Figure 4.20: An example BESS droop characteristic for frequency response. The BESS is inactive when the frequency deviation is within the dead-band(± BW) and charges or discharges at rated power, P_r at frequencies exceeding the lower and upper frequency deviation control bounds (Δf_L and Δf_U), respectively.

where v_d, v_q and i_d^*, i_q^*, are d-q reference frame voltage and currents, respectively. In the case of the frequency response operation studied here, the reference active power is derived from the frequency variation, while the reactive power reference is maintained at zero.

4.10 Autonomous frequency response

In the conventional grid dominated by synchronous generators, an imbalance between the generation and demand may lead to deviation in the system frequency. The grid frequency tends to increase when the generation is in surplus, and falls when the load exceeds the generation. In this regard, typically, utilities install additional high-ramping generators in the form of spinning reserves which respond to maintain system

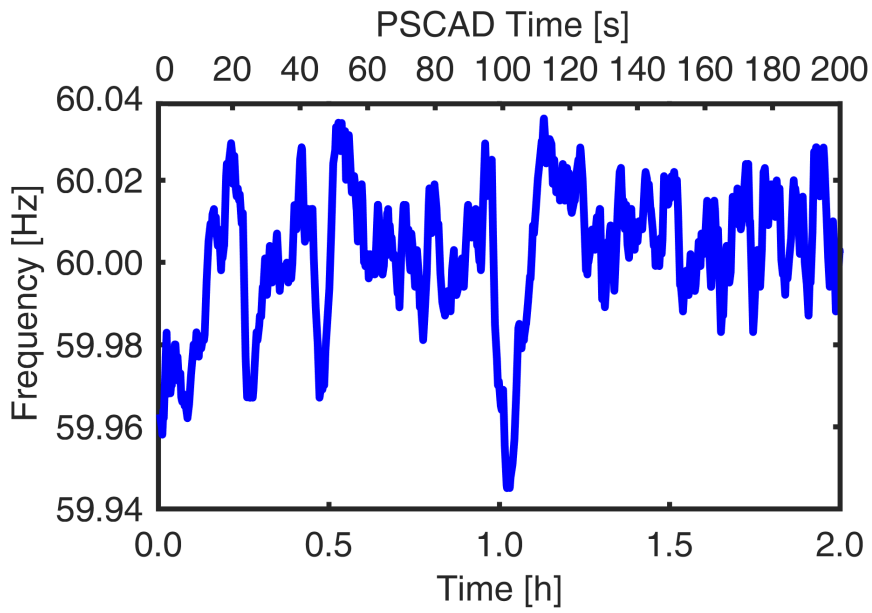

Figure 4.21: The experimental grid frequency variation. Imbalance between electric power generation and consumption typically leads frequency variation. Hence, utilities typically take measures to limit frequency variations by instantaneously meeting load demands.

frequency. These are expensive and also have power gradient limitations. In principle, BESS with extremely high ramping capabilities may be explored for frequency regulation by charging when the system frequency is above the desired value and discharging when it is low. It may be noted that this a function that requires the BESS to supply short bursts of power, and is therefore dependent on its power rating, rather than energy capacity.

In order to test and validate the developed BESS model and its controls under different operating conditions, its response to frequency variation was analyzed through a PSCAD - based study. In this analysis, the battery bank, connected to a bidirectional PCS is interfaced with the 13.2kV grid via a two winding 480V/13.2kV transformer. The BESS was then operated in its autonomous frequency mode, where it charges/discharges with respect to the observed frequency variation. For this study,

a droop control described in Fig. 4.20 was adopted for both experimental and simulation setups. The BESS is inactive when the frequency variation, Δf is within $\pm$ 0.005Hz, and discharges/charges at 1MW rated power when the Δf exceeds $\pm$ 0.05Hz.

PSCAD simulations as well as experiments were conducted with similar grid frequency variations as described in Fig. 4.21, and the output power and battery terminal voltage variations were compared. The simulated BESS output power closely follows the reference BESS real power calculated based on droop control, which demonstrates the efficacy of the control scheme. Furthermore, experimental measurements of real power output from the BESS are comparable with the simulation results (Fig. 5.3). The simulated battery terminal voltage variation under this operating mode also has close agreement with the measured value (Fig. 4.23). It may be noticed that the simulation results contain high switching frequency components, absent in the experimental results due to the smaller sampling frequency employed during measurement. The agreement between the simulation and experimental under different operating conditions results attests to the accuracy and versatility of the developed model.

4.11 Summary

This chapter reports on the variation in the equivalent circuit parameters for the racks, modules, and cells for a utility-scale battery system and presents an approach for identifying battery level parameters using equipment typically available at installation sites. A multi-hour discharge cycle for the BESS that can identify its equivalent

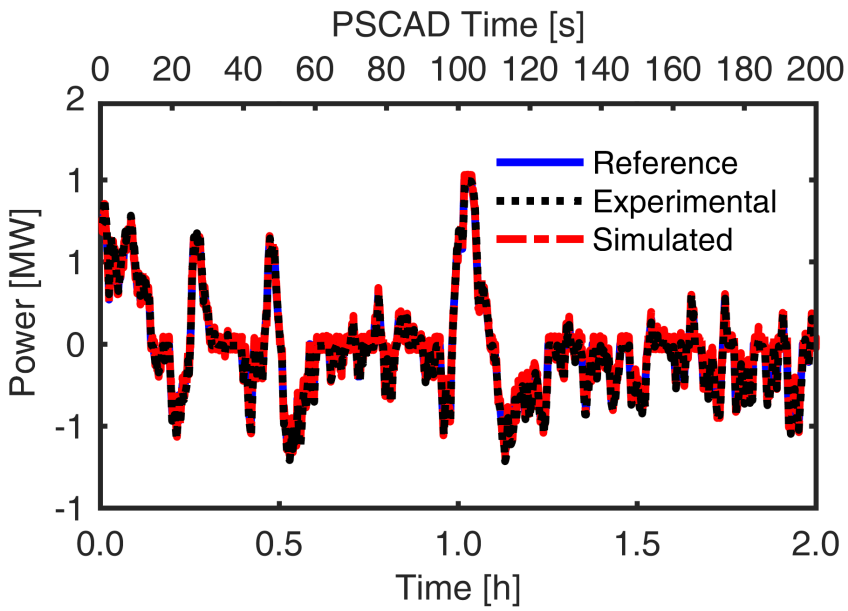

Figure 4.22: The BESS real power output. A reduction in grid frequency indicates insufficient electric generation, hence, the BESS supplies power to the grid to compensate for the deficit.

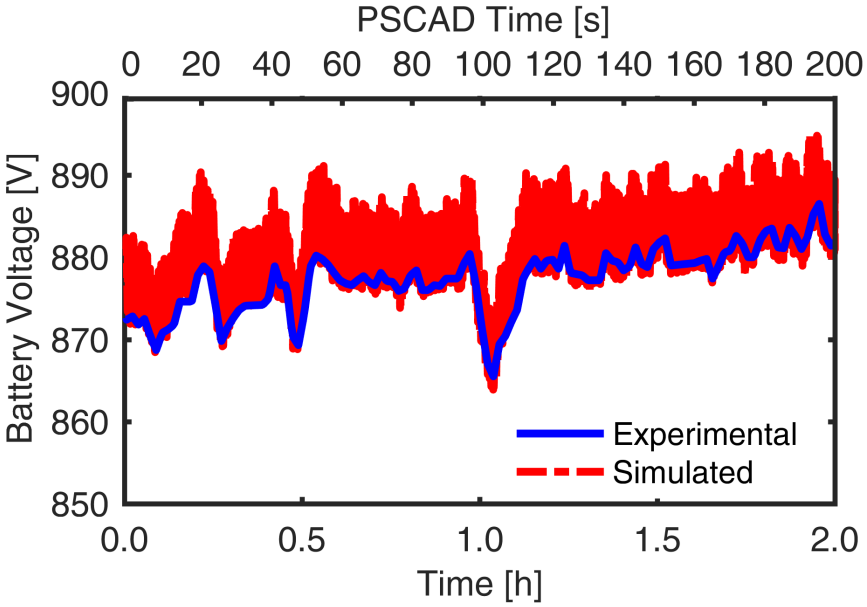

Figure 4.23: Battery terminal voltage during autonomous frequency response. High frequency variation is observed in the simulation battery voltage due to the switching of the power electronics devices, and a small sampling time.

circuit parameters while ensuring that the battery system terminal voltage stabilizes after transient discharge operations is proposed. A comparison of the performance of the equivalent circuit models derived from this approach with those obtained scaling up the parameters for battery sub-components (i.e. cells, modules, and racks) is performed, and it is found that the scaling approach can be used to represent the entire system provided that the BMS is operational. The BESS operator can adopt these models to monitor the operation of the BMS in addition to other safety and simulation applications.

The accuracy of the developed model was verified from simulation and experimental measurements conducted under similar conditions. Both simulated and experimental battery system were operated in autonomous grid frequency response mode, and the obtained battery output power and terminal voltage were found to be comparable. The results show that for the examples considered, up to 99% accuracy in the estimated battery voltage accuracy is achievable.

In order to validate the performances of the scaled equivalent circuit models and the effectiveness of the proposed approach, the simulated voltage responses of the battery system models were compared with experimental data retrieved from a 1MW/2MWh BESS, and satisfactory accuracy was observed. This work also demonstrates that the accuracy of the battery system models increases with the number of cells considered. For the example field implementation considered, average and peak voltage errors as low as 0.06% and 1.71% , respectively, were calculated with the model developed from scaling up the parameters of a single cell. This indicates that while modeling a multi-MW battery at the sub-component level may be sufficient for

all practical purposes, the accuracy of models can be improved when the parameters at the battery level are determined

Chapter 5

The Design and Analysis of Large Solar PV Farm Configurations with DC Connected Battery Systems

5.1 Introduction

The photovoltaic (PV) energy installations are fast-growing both for residential applications, as well as for utility-sized power plants [126]. Solar PV generation is intermittent in nature, and much of the associated research focuses on employing battery energy storage systems (BESS) in order to mitigate this inherent limitation. Power electronic devices play major roles in PV and BESS integration, fulfilling multiple functions including ac-dc transformation, PV maximum power point tracking (MPPT), and battery charge control[1].

Analyses have shown substantial benefits of single-stage grid-connected PV systems over two-stage PV systems, some of which include: lower cost, smaller system size, and higher efficiency [38, 39, 127]. Configurations with PV systems incorporating BESS typically introduce two additional dc-dc converters, with losses in the supplementary components [40, 50, 128, 129]. Compared to hybrid PV and battery

systems presented in [130–132], the proposed configuration, which requires only one dc-dc converter in addition to the grid connected inverter, constitutes a simple and potentially cost effective solution for integrating BESS with conventional PV systems.

Other configurations for battery integrated PV systems using a single dc-dc converter have been presented in literature. In [41], the battery is directly connected to the dc-link of a two-stage converter, which ensures simplicity, but leads to additional losses in the dc-dc converter when the battery is not operational, further affecting the battery over-voltage protection and the effectiveness of the control for the battery charge and discharge operations.

This chapter introduces a configuration for integrating BESS with multi-MW grid-connected PV systems, in which the battery is connected to the dc-link of the PV inverter via a dc-dc converter, which simultaneously serves as a charge controller and MPPT device. An approach for determining the ratings of a BESS connected to the dc-bus of an experimental PV system is proposed. This work build upon the study presented in [49]. Additional contributions include detailed calculations of curtailed solar energy due to inverter rating limitations, the development of a sizing approach for the battery to maximize solar energy utilization based on annual solar PV generation data from the LG&E and KU site.

The proposed configuration is compared with other established setups including the LG&E and KU E.W. Brown universal solar facility system, wherein the PV array and BESS are connected to the grid through individual inverters, as described in the later sections of this chapter. The modeling of a simplified BESS integrated PV system and a general approach for battery sizing is also presented in this chapter.

The proposed system components and control in addition to a comprehensive examination of the proposed configuration and controls for variable power generation and PV output power smoothing, which was simulated on a sped-up timescale using the PSCAD^{TM}/EMTDC^{TM} software are included in this chapter.

5.2 Battery integrated PV systems

Battery energy storage systems may be connected to either the ac or dc terminals of a grid-tied PV system. The ac connected battery units, which require their inverter, introduce the possibility of having an independent operation of the BESS and PV systems as well as the ease of integrating BESS into an existing PV system [133, 134]. However, the configuration is less efficient, since power needs to flow through two converters when charging the battery with the PV power.

The dc rating for utility-scale PV is typically higher than its ac-rated capacity for multiple reasons including, meeting the minimum inverter dc-bus voltage for MPPT when irradiance is limited, and to maximize the inverter utilization factor as well as system capacity factor. Hence, power is curtailed during periods of surplus irradiance, resulting in poor solar utilization and substantial energy loss, especially in sites with high solar potential [135].

The conventional PV system integrated with a dc-connected BESS includes a PV array connected to a dc-ac inverter via a dc-dc converter for maximum power point tracking (MPPT) and a battery unit connected to the inverter dc-bus via another dc-dc converter operating as a charge controller [136–138] (Fig. 5.1a). Alternatively, the E.W. Brown solar demonstration site by LG&E and KU houses multiple PV array

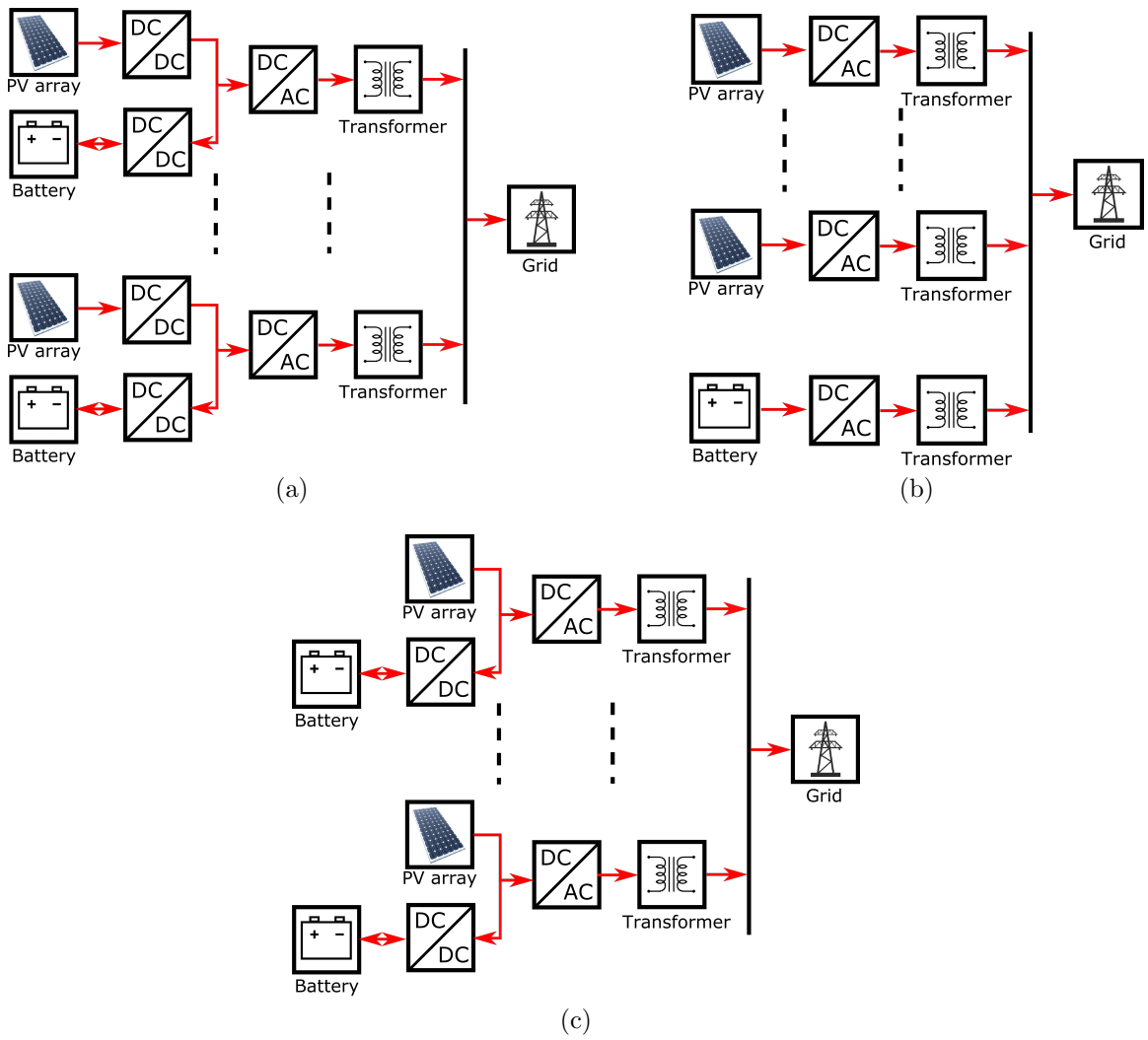

Figure 5.1: Example configurations of multi-MW PV system with BESS: (a) Conventional system with multiple dc-dc converters for MPPT and charge control, (b) field implemented system with BESS connected to the grid via independent inverter, (c) proposed system with single dc-dc converter for MPPT and charge control. These systems may also be connected to the grid without a transformer.

sections, each connected to the grid via individual dc-ac converters and a battery unit connected to the grid via an independent bidirectional dc-ac converter (Fig. 5.1b). This experimental facility PV system is divided into 10 sections with each rated for 1MW with a 1.4:1 dc to ac ratio, hence, totally, up to 4MW of power is curtailed at rated irradiance.

The multi-MW PV system configuration proposed in this chapter is divided into multiple modular sections, where each includes a PV array, battery unit, bidirectional dc-dc converter, two-level grid-connected inverter and transformer (Fig. 5.1c). The dc-dc converter operates simultaneously as a charge and as an MPPT controller by varying the charge/discharge power of the battery bank to maintain the PV array at the voltage corresponding to its MPP. This configuration allows the battery integrated PV system to operate as a single-stage PV system during periods when the battery is not operational. Also, the proposed configuration can be used to improve the overall system stability of the PV system by constantly maintaining the PV array at its MPP reference voltage during periods of excess irradiance.

5.3 Methodology for sizing the BESS

The PV system dc output power is represented as a function of its irradiance and cell temperature. The calculated dc power is expressed as

$$P_{dcS} = \left(\frac{\gamma}{1000} \cdot P_{r1}\right) \times \left(-\frac{0.41}{100} T_{cell} + 1.1025\right), \tag{5.1}$$

where P_{dcS}, represents the available PV array dc power; P_{r1}, the rated PV array dc power; γ, the system irradiance calculated as the average plane of array (POA) irradiance from two weather stations located on the PV farm; T_{cell}, the cell temperature estimated as the average temperature from 40 thermometers located at back of selected PV modules distributed across the PV farm (Fig. 5.2). The expression for P_{dcS} also accounts for the PV modules -0.41%/^oC maximum power temperature coefficient.

The amount of power supplied to the grid from the PV system is limited by the ac rating of its inverter. Hence, the power supplied to the grid (P_{gS}) is expressed as:

$$P_{gS} = \begin{cases} P_{dcS} & P_{dcS} < P_{r2} \\ P_{r2} & \text{otherwise} \end{cases}, \tag{5.2}$$

where P_{r2} is the inverter rated power. In contrast, for systems with dc connected BESS, additional power from the PV array that will otherwise be curtailed during periods of excess irradiance due to inverter ac specifications may be stored in the BESS. A simplified expression for the power flow in the BESS is described as

$$P_{battS} = \begin{cases} P_{r2} - P_{dcS} & 0 < P_{r2} - P_{dcS} < P_{rb} \\ P_{rb} & P_{r2} - P_{dcS} \geq P_{rb} \\ 0 & \text{otherwise} \end{cases}, \tag{5.3}$$

where, P_{battS}, is the battery output power and P_{rb}, is the BESS rated power. It may be noted that (3) only describes battery charging operations. The PV system ac output power retrieved from the 10MW$_{ac}$ experimental facility (P_{gE}) was compared with the calculated P_{gS} for two consecutive sample days with and without excess irradiance, respectively (Fig. 5.3). The battery is controlled to stop charging when its state of charge (SOC) reaches the maximum specified value. For simplicity, factors

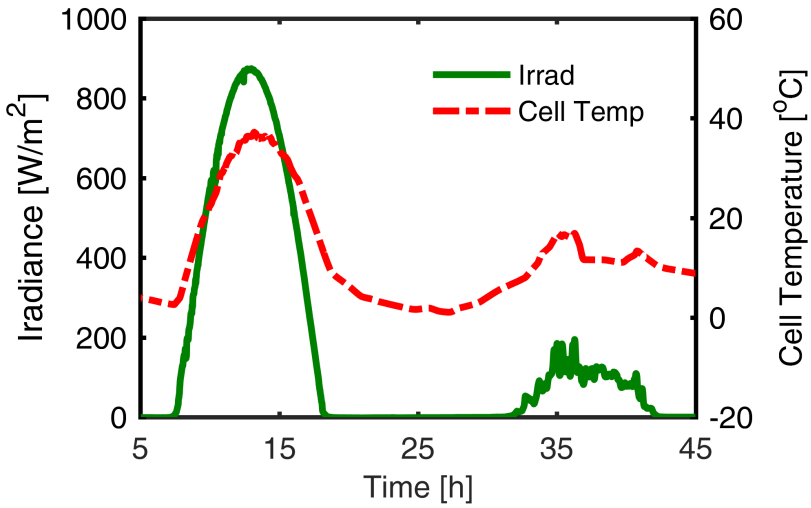

Figure 5.2: PV system irradiance and cell temperature retrieved from the experimental facility for two example consecutive days. The cell temperature is measured as the average from the back of 40 solar modules distributed across the 45acres PV farm and the irradiance is measured as the average from two weather stations.

such as power electronics and battery round trip efficiency are not considered in this study.

The amount of PV energy curtailed daily varies with different seasons of the year. The daily curtailed PV energy in the absence of dc connected storage is calculated as:

$$\lambda_f = \int_{t0}^{t1} (P_{dcS} - P_{gS}) dt, \tag{5.4}$$

where, λ_f, is the PV energy curtailed on day f; t, is time; $t0$ and $t1$, are PV curtailment start and end times of the day, respectively. λ_f was evaluated for the example year with the experimental data retrieved from the LG&E and KU 10MW$_{ac}$ PV system and the peak curtailed PV energy was observed during the spring period between April and May (Fig. 5.4). The distribution of the daily PV system energy curtailed was evaluated, in order to establish the size and need for energy storage connected to its dc-bus. It was observed that on most days, the curtailed energy was less than

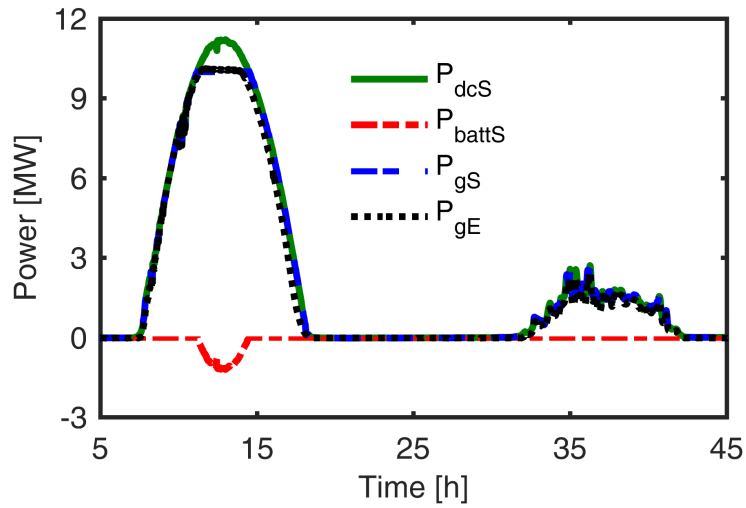

Figure 5.3: Experimental (P_{gE}) and simulated (P_{gS}) PV system output power for two example days validating the simplified PV system model and estimating the curtailed power. P_{dcS} represents the available dc power and P_{battS} represents the power available for storage. A negative sign indicates power flow into the battery.

2MWh (Fig. 5.5). This indicates that the PV curtailed energy can be reduced significantly by using a relatively small scale BESS rated for 2MWh.

Battery energy storage systems are typically sized in terms of power rating and energy storage capacity. A large battery would lead to a reduction in curtailed energy, but become prohibitively expensive. Therefore the minimum battery size which reduces annual curtailed energy is determined. For simplicity, it is assumed that the battery was discharged to its minimum state of charge (SOC) at the start of each day and charges during periods of excess irradiance provided that its cumulative stored energy is less than the rated energy capacity and the SOC is below the specified maximum limit. The annual PV energy curtailed is computed as:

$$C_{yr} = \sum_{f=1}^{365} (\lambda_f - E_{bf}), \qquad \text{where} \quad E_{bf} \leq E_{rb}, \tag{5.5}$$

C_{yr}, represents the annual curtailed energy; E_{bf}, the total energy stored in the battery

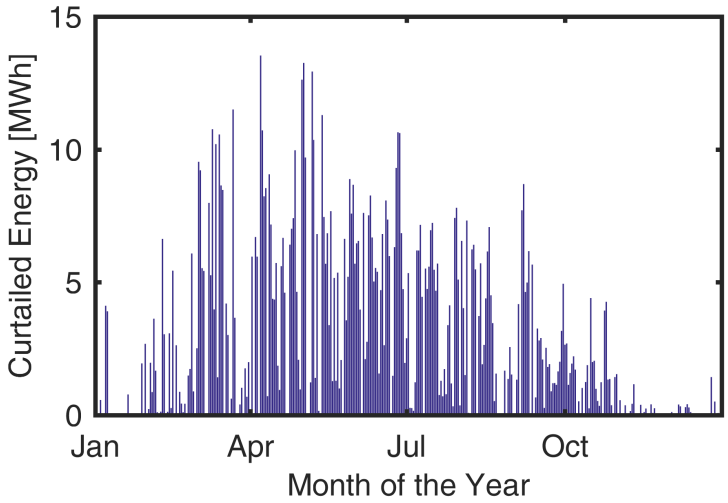

Figure 5.4: Daily curtailed energy comparison over one year. The solar panels are oriented to peak over the summer, hence, the maximum curtailed energy occurs between April and May.

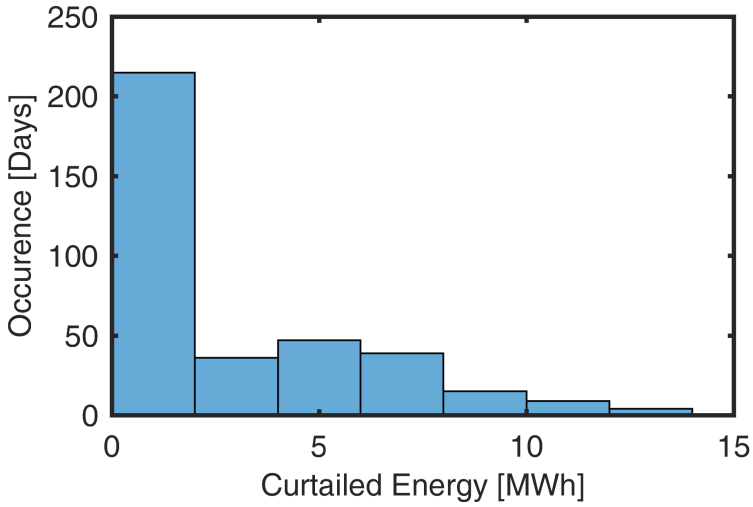

Figure 5.5: Daily curtailed power distribution over one year. The daily curtailed energy is less than 2MWh for most of the year and greater than 8MWh for less than 40 days.

on day f; and E_{rb}, the battery energy capacity. The value of C_{yr} was computed for multiple P_{rb} and E_{rb} combinations at 20kW and 60kWh intervals, respectively, and the results are plotted (Fig. 5.6).

For the analyzed example year and case study considered, it can be observed that the desired energy curtailment can be achieved with different battery rating combinations and approximately 1:3 BESS power to energy ratio is the minimum rating combination for a specified C_{yr}. Also, it is observed that increasing the BESS size above 2MW/6MWh, does not lead to a significant reduction in the amount of energy curtailed (Fig. 5.6).

In the case of the field implemented $14\text{MW}_{dc}/10\text{MW}_{ac}$ PV system and example year considered, up to 360MWh of energy curtailed may be retrieved if a 1MW BESS capable of storing up to 2MWh were connected and distributed across the dc-buses of all PV sections. Since BESS typically have a limited SOC operation range, the recommended battery energy capacity may need to be oversized accordingly. Although, the BESS is primarily sized to reduce the annual curtailed PV energy, it should be noted that its rating is still sufficient for satisfactory grid ancillary services such as, PV power smoothing, frequency regulation, constant power production, and energy arbitrage, some of which are demonstrated in the subsequent sections.

5.4 System configuration and components

Battery energy storage system(s) are expected to play a significant role in the integration of renewable energy sources into the future electric grid. Typical field implementation of Multi-MW PV systems exists as single-stage systems, which includes

Table 5.1: Main specification for 10MW PV power plant

	Experimental	**Proposed**
AC rated power (MW)	10.00	10.00
Clear day capacity factor (%)	38.91	44.50
Clear day PV energy (MWh/section)	9.34	10.68
PV smoothing Battery usage (MWh/section)	0.40	-0.74
Annual energy output (GWh)	19.32	20.32
Annual capacity factor (%)	22.05	23.19
Max. PV array dc power	inverter rating	PV rating
Battery charge efficiency	$\eta_{inv} \times \eta_{inv}$	η_{dcdc}

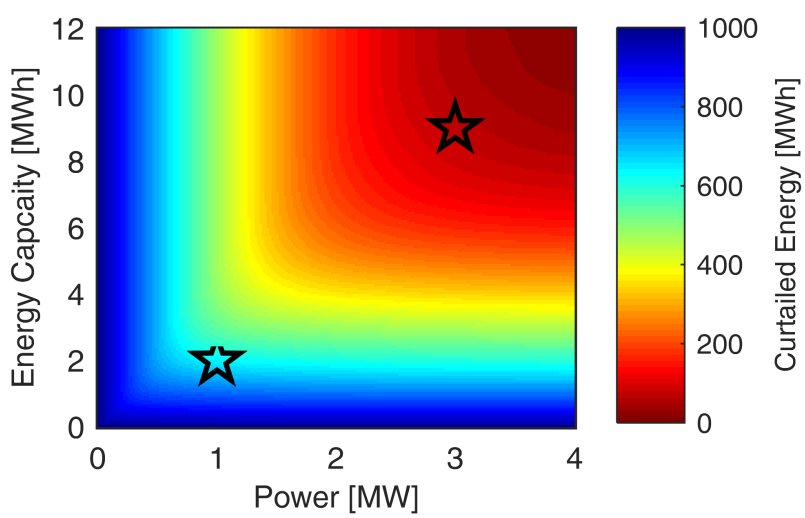

Figure 5.6: Annual PV energy curtailed for multiple dc connected battery power and energy ratings. For the example considered, up to 1GWh energy may be curtailed without a dc connected battery.

Figure 5.7: The LG&E and KU E.W. Brown universal solar facility, which houses a 14MW_{dc} 10MW_{ac} PV system. The PV system is divided into ten sections with each rated 1MW_{ac}.

multiple sections of PV arrays interfaced with the grid via a dc-ac converter capable of performing MPPT. The proposed configuration may be used to enhance the operation of these existing systems by connecting a battery pack via a bidirectional dc-dc converter to the existing inverter dc link. Depending on the power and energy rating of the integrated BESS, the proposed system may be used to perform operations such as PV output power smoothing, PV constant power production, and peak shifting.

The field implemented PV system consist of ten PV arrays, each made up of 19 Jinko JKM315P-72 PV modules connected in series and an average of 236 module strings in parallel. An equivalent PV array was modeled in PSCAD^{TM}/EMTDC^{TM} with each 315W PV panel rated at 46.75V open circuit voltage and 9.02A short circuit

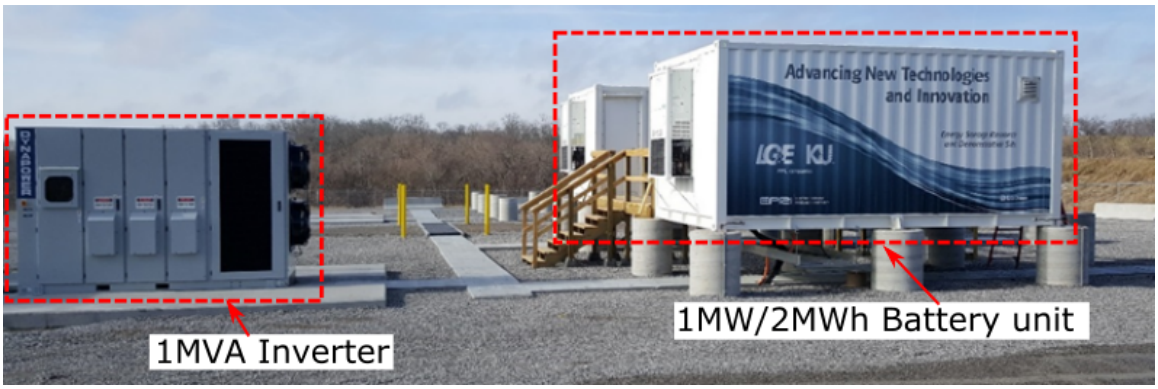

(a)

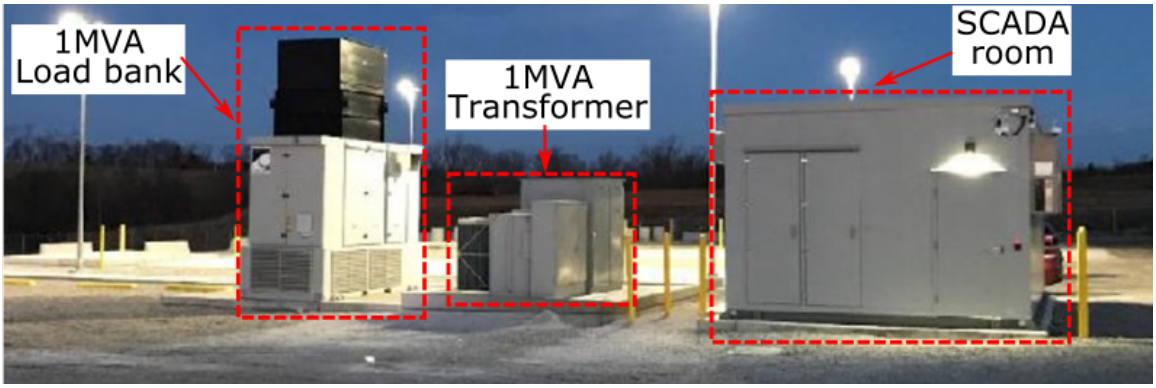

(b)

Figure 5.8: The battery energy storage system (BESS) setup at E.W Brown LG&E KU facility rated 1MW/2MWh. (a) Two parallel battery container units are connected to the grid through a bidirectional dc-ac converter, (b) SCADA room for high resolution data management and system control. The experimental facility may be operated in the islanded mode with a 1MVA load bank connected to the secondary side of the transformer.

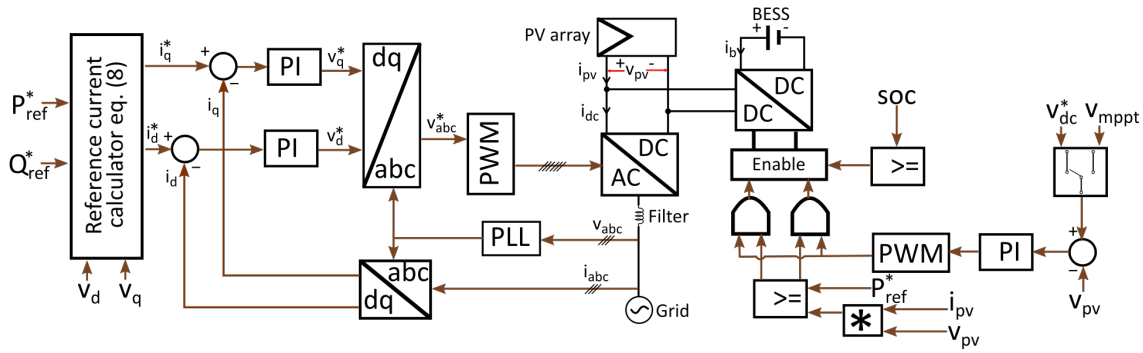

Figure 5.9: Proposed system schematic and configuration control scheme. The BESS controller charges when P^*_{ref} is lower than the PV output power ($i_{pv} \times v_{pv}$). The BESS control is disabled or discharge based on the BESS converter control so that battery supplies or absorbs the amount of power required to maintain the PV array voltage (V_{pv}) at the voltage corresponding to its MPP (V_{MPPT}).

current. The equivalent circuit of the PV cell was modeled based on

$$i = i_g - i_o \left[\exp\left(\frac{v + iR_{sr}}{n\mathrm{K}T_c/q} \right) - 1 \right] - \left(\frac{v + iR_{sr}}{R_{sh}} \right), \tag{5.6}$$

where, i represents the cell output current; i_g, the component of cell current due to photons; i_o, the saturation current; K, the Boltzmann constant (K = 1.38x$10^{-23} j/K$); q, the electron charge (q = 1.6x10^{-19}C); v, the output voltage; T_c, the cell temperature; R_{sh}, the shunt resistance and R_{sr}, the series resistance.

The field implemented energy storage site consists of two shipping containers (Fig. 5.8) with multiple Li-ion LG Chem battery modules, each rated for 51.8V/126Ah connected in series and parallel to make up a 1MW/2MWh battery pack connected to the grid through an independent inverter. This approach assumes an active battery management system for balancing voltage and SOC across series and parallel cell combinations is included in the battery pack. Hence, a representative cell is scaled to represent a battery pack with 0.35kV nominal voltage.

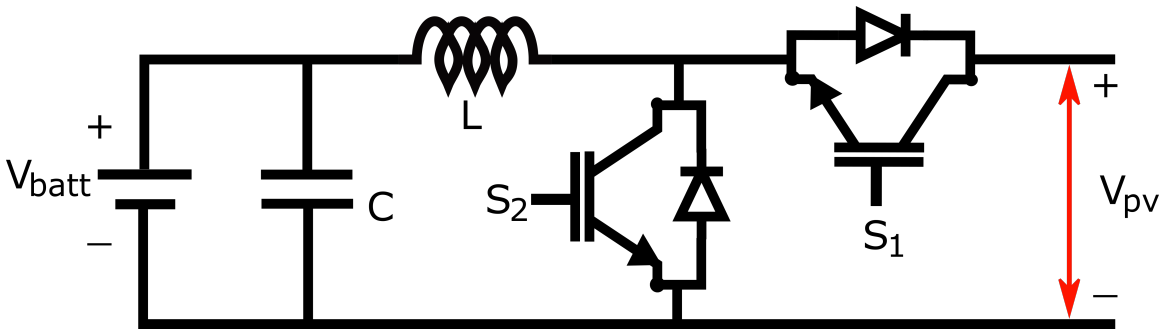

Figure 5.10: The battery unit connected to the PV array and inverter dc-link through a bidirectional converter, where switch S_1 and S_2 are used to regulate the battery charge and discharge current, respectively.

5.5 Power electronics and controls

The proposed system requires a dc-dc converter for the battery power flow control in addition to the inverter which interfaces the PV system with the ac grid. In this study, a bidirectional Buck/Boost converter topology (Fig. 5.9), which typically includes two switches, inductor, and capacitors is employed as a charge controller capable of regulating power flow with the battery. The PV system is connected to the grid through a two-level inverter, a widely available technology that is relatively low-priced with well-established controls and has been demonstrated to be reliable for small inverters below 1MW [139]. The BESS and dc-dc converter offer a means for capturing PV energy that would otherwise be curtailed. This stored energy can be used potentially for PV smoothing and grid ancillary functions.

The system is capable of operating in different modes, which are based on the battery power flow direction or its availability. Also, the proposed configuration allows the power sources to operate effectively and independently of one another. The inverter employs a voltage oriented control scheme in which its active and reactive

current components are calculated as a function of P^*_{ref} and the reference reactive power of the system (Q^*_{ref}) as follows:

$$i^*_d = \frac{2}{3}\frac{P^*_{ref}}{v_d}, \qquad i^*_q = \frac{2}{3}\frac{Q^*_{ref}}{v_q}, \tag{5.7}$$

where, v_d, v_q and i^*_d, i^*_q, are d-q reference frame voltage and currents, respectively.

Mode I: This is the preferred mode of operation, in which the battery charges with the surplus available power. In this operation mode, the ac set power, P^*_{ref} may be calculated as a function of the available PV energy, in which the PV system is expected to operate at its MPP at all times. During periods of excess irradiance or conditions when the ac system rating is less than the available PV power, the battery dc-dc converter is operated in Buck (charging) mode, where it ensures MPPT stability by maintaining the PV array terminal voltage at its MPPT reference. In buck mode, pulses to switch S_1 are modulated to charge the battery with the excess power required to maintain the PV array terminal voltage at MPP when greater than the MPP reference. Hence, the converter current during charge is given as:

$$i_{b(c)} = \frac{(i_{pv} - i_{dc})}{(V_{MPPT} - V_{pv})\left(K_{ps} + \frac{K_{is}}{s}\right)}, \tag{5.8}$$

where $i_{b(c)}$ is the battery charging current; V_{MPPT}, the reference MPP voltage; V_{pv}, PV array terminal voltage; i_{dc}, inverter dc current P^*_{ref}; K_{ps} and K_{is}, PI controller constants. The battery may also be operated in this mode during period of PV unavailability, in which P^*_{ref} is calculated as the amount of ac power from the grid and the dc-dc charges with corresponding current required to regulate the dc-link voltage at specified value.

Mode II: During periods when P^*_{ref} is greater than the available PV power, due

to shading for example, the battery can be used to supply the power deficit. In this case, the dc-dc converter is operated in boost mode, and the duty cycle for switch S_2 is regulated to ensure the PV array is operating at MPP, while the battery supplies the deficit power. The dc-dc converter current during discharge is expressed as:

$$i_{b(d)} = \frac{(i_{dc} - i_{pv})}{\left[1 - (V_{MPPT} - V_{pv})\left(K_{ps} + \frac{K_{is}}{s}\right)\right]}, \tag{5.9}$$

where, $i_{b(d)}$ is the battery discharge current.

The battery may also be operated as an independent BESS storage system capable of directly interacting with the grid. During discharge, while the battery is above its minimum SOC, the dc-dc converter switches to constant voltage mode, in which it discharges in order to maintain the dc-link voltage at its reference value (V_{dc}^*). The reference dc-link voltage should be greater than the peak ac voltage during discharge and expressed as:

$$V_{dc}^* > \sqrt{V_d^2 + V_q^2}. \tag{5.10}$$

Hence, the battery discharges when the dc-link voltage is less than V_{dc}^* and switch modes to charge when otherwise.

Mode III: The system operates in this mode when the battery SOC is beyond operation range or unavailable. The setup is operated as a single stage PV system, in which the BESS is disconnected from the dc-link and the inverter maintains the PV array at its MPP reference as long as the available PV power is smaller than the ac rating. In this mode, P_{ref}^* is expressed as:

$$P_{ref}^* = (V_{MPPT} - V_{pv})\left(K_{pi} + \frac{K_{ii}}{s}\right), \tag{5.11}$$

and the inverter reference active current components as:

$$i_d^* = \frac{2}{3}\frac{(V_{MPPT} - V_{pv})}{v_d}\left(K_{pi} + \frac{K_{ii}}{s}\right), \tag{5.12}$$

where, K_{pi} and K_{ii} are the PI controller constants for the dc-ac converter. It may be noted that in this case, as the inverter capacity is less than the PV dc rating, excess power, otherwise stored in the battery, will need be curtailed during periods of excess irradiance.

Detailed calculations on the filter inductor, and capacitor sizing for this configuration are beyond the scope of this study. Hence, the capacitors connected across the battery terminal and the inverter dc-link, and the dc-dc inductors were sized to be large enough to absorb the ripple currents and ensure minimum voltage variation based on a simplified systematic analysis.

Typical Multi-MW inverters are divided into identical modular power blocks, which are cascaded and connected in parallel to the ac grid. The field implemented system includes central inverters, which are based on automatic redundant modular multi-master systems, where each module is rated for 200kVA to 240kVA [140]. While switch selection is not the focus of this research, the proposed configuration may be developed with IGBT switches rated for power less than 1MVA. This configuration leads to an increase in system efficiency when charging the battery with PV power, compared to the conventional approach with losses in two dc-dc converters and the experimental setup with losses in the PV and BESS inverters. When operated in mode 2, there is a slight reduction in the proposed system battery round trip efficiency due to the losses in the dc-dc converter, compared to the experimental setup,

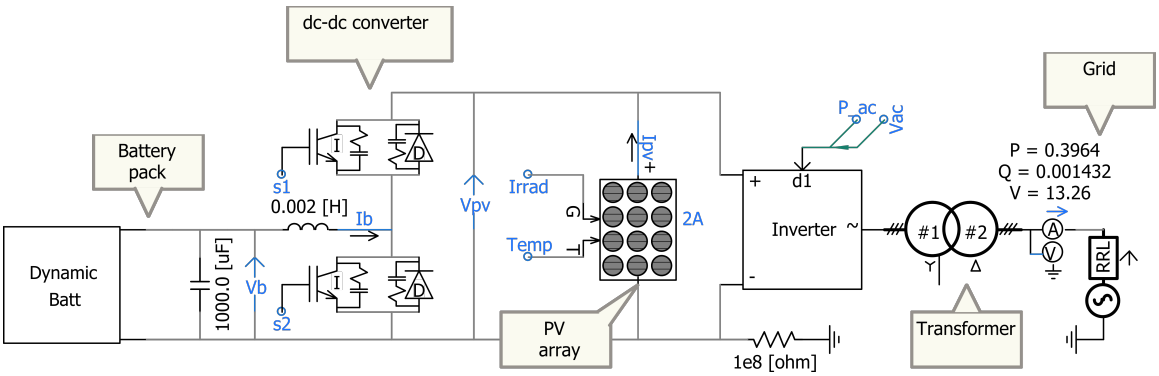

Figure 5.11: The power circuit diagram in the PSCAD^{TM}/EMTDC^{TM} software environment for a single unit of the proposed system in Fig. 5.1c, where a constant voltage source is used to represent the grid.

where the PV and BESS have independent inverters. Generally, due to the reduced amount of switching devices, dc-dc converters have higher efficiencies when compared to dc-ac converters [141].

5.6 Validation of proposed system

The performance of the proposed and field implemented systems were compared via simulation studies, where the irradiance data used was calculated as the average of the data from two weather stations on the LG&E and KU 10MW universal solar facility on a clear day. The PV cell temperature was estimated as a function of the measured ambient temperature. The field implemented system PV array is rated 14MW$_{dc}$ with 10MW$_{ac}$ inverters which are operated for maximum power transfer from the PV array. However, during periods of surplus irradiance, when the inverter power rating is insufficient to transmit the available PV power, the system switches to the constant power mode, where excess power is curtailed For the example day considered, the field implemented system switches from the MPPT mode to constant

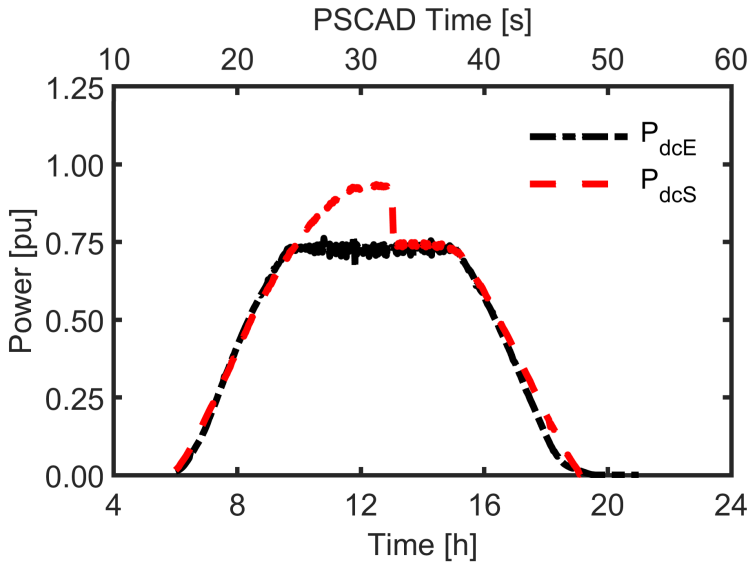

Figure 5.12: PV array dc output power for the proposed (P_{dcS}) and field implemented (P_{dcE}) setups. Due to BESS unavailability at approximately 13h, the proposed system also curtails excess power during periods of surplus irradiance. P_{base}=1.4MW.

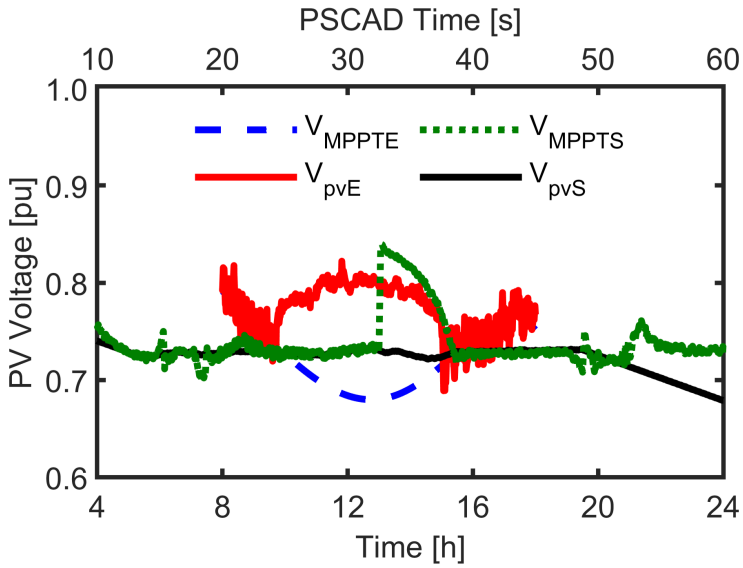

Figure 5.13: The PV array terminal voltages and MPPT references. The field implemented setup deviates from its MPPT reference during periods of excess irradiance, while the proposed setup switches to power curtailment mode only at 13h due to BESS unavailability. Where, V_{pvE}, V_{MPPTE}, V_{pvS}, and V_{MPPTS} represents the PV array voltage and MPPT reference for the experimental and proposed setup at V_{base}= 0.89kV, respectively.

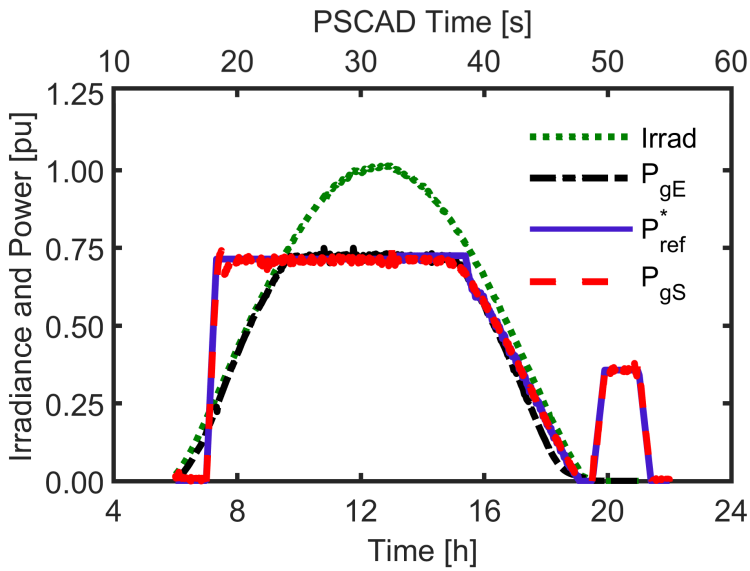

Figure 5.14: The system ac output power and experimental irradiance data ($irrad$) for the proposed (P_{gS}) and field implemented systems (P_{gE}). At approximately 19h when PV power is unavailable, the BESS discharges independently to the grid. The $irrad_{base}$=1000W/m^2, P_{base}= 1.4MW.

power operation at approximately 10h, forcing the PV array voltage to deviate towards open circuit and away from its MPP reference, leading potentially to unstable operating points [142].

A single section of the multi-MW PV system is simulated in PSCAD/EMTDC under multiple operation modes for the same example day, in order to evaluate the expected transients during transitions and validate the model operation(Fig. 5.11). The P^*_{ref} was calculated to illustrate diverse operation modes of the proposed system. Also, the BESS was set to be unavailable between 13h-19.5h to validate the system performance and transient stability (Fig. 5.12) . The PSCAD/EMTDC simulation was accelerated such that the 1s PSCAD time represents 24min real-time.

The reference active power was controlled for constant power with a ramp rate of 10%/min. In order to maintain the PV array at the MPP, the BESS charges during

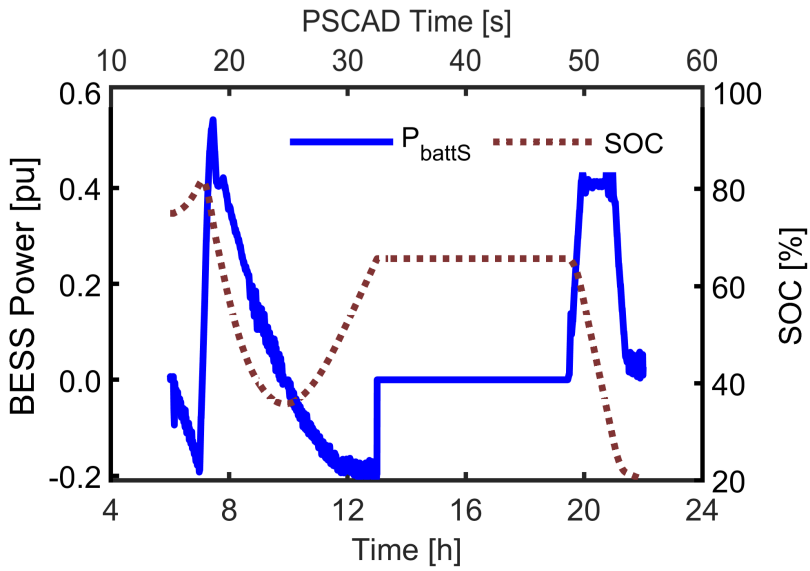

Figure 5.15: Battery net power flow and state of charge (SOC). The BESS charges and discharges in other to maintain the system ac output at the reference value. The BESS was unavailable between 13h and 19.5h, and later discharges to the grid till 20% SOC.

the periods when P^*_{ref} is less than the available PV power and discharges otherwise, such that the inverter output corresponds to its reference.

At approximately 13h, the BESS system is fully charged, and therefore considered to become unavailable, and the system transitions into a different operation mode, where the dc-dc converter is inactive and the inverter switches to MPPT mode. Similar to the field implemented system, the simulated system operates at constant power mode during periods of excess irradiance, in which it curtails the additional power that would otherwise be stored in the BESS. Therefore, the PV array terminal voltage can be observed to deviate from its MPP reference during periods of surplus power availability and returns when the irradiance is below 714W/m^2 (fig. 5.13. It may be noted that the fully charged BESS can be used to supply the power deficit when the power available from the PV system is lower than the inverter ac rating.

During the late hours of the day when the irradiance is nearly zero and BESS is available, the system was operated to discharge independently, and reference active power calculated for the BESS to provide grid ancillary services (Fig. 5.14). Close to 19.5h, the BESS was operated to supply power to the grid to support the evening peak power demand. For simplicity, during this period, the battery dc-dc converter was regulated to maintain the dc-link voltage at 0.65kV, while the inverter maintained the real power output at the reference value (Fig. 5.15).

As an example, following the experimental study previously presented, the available 1MW/2MWh battery unit with a larger PV array of 1.54MW per section for the best weather condition is capable of producing 11.75MWh with the 1MW inverter, hence increasing the system capacity factor by 20.4%. It may be noted that the increase in the system capacity factor may vary from site to site, and is expected to be higher for areas with high natural solar resources.

5.7 PV power smoothing

Battery energy storage systems may be employed on a cloudy day, to smooth the PV output power variation, in order to improve the delivered power quality, meet grid ramp rate limitations and limit potential frequency deviations. In the case of multi-MW PV systems, sudden changes in the output power due to cloud movement can potentially induce severe voltage fluctuations leading to grid stability issues [142]. Utility companies with high renewable energy penetration often limit their maximum allowable ramp rate to 10% per minute, based on the system's rated capacity [143]. Different methods of curtailing the PV system real power output ramp rate through

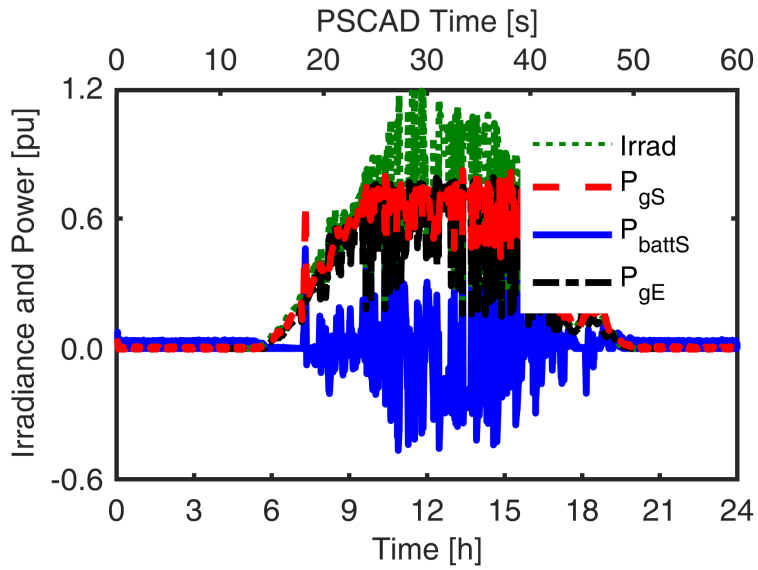

Figure 5.16: PV output power smoothing over a cloudy day; Per unit ac output power and experimental irradiance data ($irrad$) for the proposed (P_{gS}) and field implemented systems (P_{gE}), where P_{battS} represents the battery dc output power. $irrad_{base}$=1000W/m^2 and P_{base}=1.4MW.

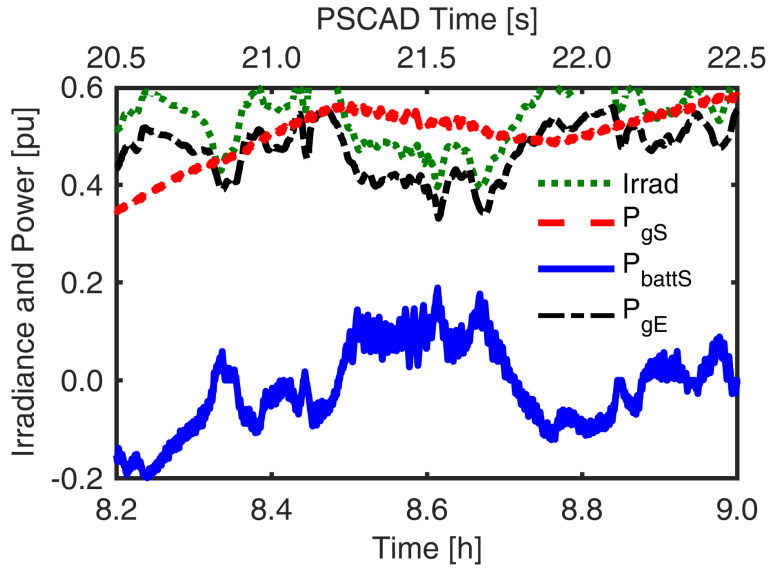

Figure 5.17: A zoomed-in representation of cloudy day power variation for experimental and simulated results. Battery charges and discharge at high frequency in order to reduce PV ramp rate while maintaining PV array voltage at MPP reference.

modified MPPT algorithms have been proposed [144, 145]. These methods lead to increased computational burdens, reduction in energy produced by the PV system and also require accurate weather forecasting devices. For this approach, the reference real power output of the PV inverter (P_{ref}^{MA}) is computed using a moving average (MA) technique to determine the sample mean of the saturated PV output estimated as:

$$P_{ref}^{MA}(t) = \frac{P_{dcE}(t) + P_{dcE}(t-1) + ... + P_{dcE}(t-\Delta+1)}{\Delta}, \tag{5.13}$$

where, P_{ref}^{MA} is the smooth PV power output; P_{dcE}, the PV system dc output power; t, the time and Δ, the number of considered points. For this study, the proposed system operation over a cloudy day was analyzed using irradiance data retrieved from two weather stations on the LG&E and KU 10MW universal solar facility and simulated on a PSCAD^{TM}/EMTDC^{TM} accelerated time scale. The moving average sample data was computed over 1000s, which reduced the maximum PV system ramp rate from 56.31%/min to 4.15%/min maximum (Fig. 5.16).

The BESS is controlled to supply the power difference between the available PV power and the computed moving average power of the PV system (Fig. 5.17). The field implemented 1MW/2MWh BESS requires 0.40MWh energy in order to smooth the output power of the PV system while the proposed configuration smooths the PV output power, maintains the PV array at its MPP and provides additional storage energy of 0.74MWh to the battery which may be supplied to the grid at later hours.

5.8 Summary

The detailed technical benefits of the proposed configuration with respect to PV output power smoothing and variable power generation were illustrated through PSCAD^{TM}/EMTDC^{TM} simulations of two case studies with irradiance variation for a clear and cloudy day. Furthermore, the performance and steady operation of the proposed dc-dc converter and transition into multiple operation modes was verified. In order to validate the capabilities and effectiveness of the proposed system and controls, its simulated performance was compared with computed and experimental data from the LG&E and KU E.W. Brown universal solar facility, which houses a 10MW PV farm and a 1MW/2MWh BESS. The results show that for PV installations in an area with good solar PV resources and a lot of clear days, an increase in the annual capacity factor of up to 20% is possible with a dc-bus connected battery. At the other end, a negligible increase in the capacity factor for areas with limited solar availability is expected.

Chapter 6

Conclusions

6.1 Summary

In this dissertation, several frameworks and simulation efforts for evaluating the impact of integrating large solar PV plants and approaches for using battery energy storage systems (BESS) to mitigate some of its adverse effects were proposed. In chapter 2, a detailed utility-scale solar PV plant with 10 modular sections and ac connected with a BESS was developed. It was demonstrated that the output power of PV systems with and without dc-dc converters for maximum power point controller is virtually the same and maximum power point tracking is achievable for all irradiance levels without a dc-dc converter. In the same chapter, multiple applications of BESS for addressing the impact of solar PV penetration and improving the overall grid performance were presented. An electromagnetic transient simulation study analyzing the effect of these inverter-based resources operation on conventional generators and example transmission network was presented.

In chapter 3, a framework for estimating the maximum solar PV penetration a generation and transmission system can sustain without significant upgrades to existing

infrastructure was proposed. The approach envisions a system with large amounts of variable renewable penetration and includes information required for the system planner to reliably operate the generation portfolio in a least-cost manner in both present and future scenarios. This framework also includes a detailed minute-to-minute (M-M) economic dispatch model capable of capturing the intermittent impact of solar PV plants and identifying the minute-based periods of generation imbalanced required for performance regulations. The minute-to-minute economic dispatch model was also employed for evaluating the impact of PV penetration on an example transmission system and used to estimated the maximum PV power plant that can be connected to any of its buses without violating its bus voltage and branch thermal limits.

A dynamic module for inverter-based resources such as solar PV, wind, and BESS was also proposed in Chapter 3. Opposed to conventional approaches, where dynamic IBRs were modeled as controllable current sources generating sinusoidal currents without harmonics and incapable of modeling unbalanced fault conditions. This study includes a dynamic IBR module which may be regarded as a hybrid system that combines the comprehensive benefits of detailed the IBR models with the reduced computational requirement of the average models. The results from the study indicate that the maximum PV system that may be connected to a transmission network depends on multiple factors including its point of interconnection, transmission system voltage and thermal limits, and the combination of generators operating on the system.

One of the main contributions of this dissertation is included in Chapter 4, which proposes new procedure and software framework for estimating the equivalent circuit

model (ECM) parameters for utility-scale BESS. Contrary to the rapid pulse discharge cycles employed in conventional cell parameter estimation approaches, the study proposes a new charge/discharge cycle for identifying the equivalent circuit parameters for utility-scale battery systems using equipment readily available at installation sites without the need for laboratory setups. The results of this study demonstrate that the ECM for a reference cell, module, or rack of a BESS can be scaled to represent the entire battery system provided that the battery management system is active and functional.

A mathematical runtime equivalent circuit model suitable for electromagnetic transient studies over an accelerated time scale was also proposed in Chapter 4. The performance of the developed module was compared with an operational BESS with identical specification over multiple working methods including the autonomous frequency response mode. The results show that for the examples considered, up to 99% accuracy in the estimated battery voltage accuracy is achievable with the proposed model.

A method for integrating battery storage into multi-MW grid-connected PV systems through the use of a dc-dc converter, capable of simultaneously operating as a charge controller and MPPT device is proposed in Chapter 5. Advantages of such configuration were explored and a general approach for sizing dc-bus connected batteries to reduce the annual curtailed energy from utility-scale PV farms is developed. This approach evaluates the minimum battery size which can achieve substantial reductions in the annual solar energy curtailed. It was found that at the LG&E and KU site, a BESS power to energy capacity ratio of approximately 1:3 leads to substantial

savings.

6.2 Original contributions

The main contributions of this dissertation can best be summarized as follows:

1. The impact of utility-scale solar PV and BESS represented by several detailed modular units connected in parallel on the operation of traditional generation and transmission systems. It was demonstrated that the integration of adequately sized BESS can mitigate a significant amount of challenges related to solar PV intermittency. A sizing exercise for dispatchable solar PV and BESS was proposed. (Chapter 2)

2. A framework for estimating the PV penetration a service area can sustain without needing significant upgrades to its existing infrastructure. The framework analyzes the impact of increasing PV penetration on generation and transmission networks while considering the responses of conventional generators to changes in solar PV output power (Chapter 3)

3. A detailed minute-to-minute (M-M) economic dispatch model capable of capturing the impact of renewable intermittency and estimating the over- and under-generation dispatch scenarios due to PV volatility and surplus generation. (Chapter 3)

4. A dynamic IBR resource module with a variable capacity that can be employed for multiple systems including solar PV, wind, and battery system. The

proposed module may be regarded as hybrid system that combines the comprehensive benefits of detailed IBR models with the reduced computational requirement of the average models. (Chapter 3)

5. An approach for developing the equivalent circuit model of a utility-scale battery system capable of estimating the voltage response of the entire unit with up to 99% accuracy, using equipment typically available at the installation site. A multi-hour discharge cycle for the BESS that can identify its equivalent circuit parameters while ensuring that the battery system terminal voltage stabilizes after transient discharge operations was also proposed (Chapter 4)

6. Evaluation and comparison of the performance of utility-scale equivalent circuit models developed at multiple sub-component levels, i.e. at the rack, module, and cell levels. The results of the study indicated that for a battery system with an active battery management system, the equivalent circuit model of either the cell, module or rack can be scaled to represent the entire battery system with less than 1% average error. (Chapter 4)

7. A new configuration and control for PV and battery system to share a dc-dc converter, increase PV capacity factor as well as inverter utilization factor. The setup provides the utility the capability of integrating energy storage into existing PV systems at a minimal cost. (Chapter 5)

6.3 Recommendations for future work

Based on the results of this dissertation and earlier research conducted by others, possible further research may include the following:

1. The battery sizing technique presented in chapter 2 does not consider the usable capacity of the BESS, its round trip efficiency, and self-discharge rate. As the next step to this work, considering these parameters and employing advanced optimization such as differential evolution and genetic algorithm can appropriately establish a relationship between the ac to dc ratio of a solar PV and the BESS power energy capacity required to make it dispatchable.

2. The proposed minute-to-minute dispatch model in chapter 3 may even be further improved upon the integration of additional cost parameters such as generator start-up cost, shut down cost, days and hour ahead forecasts that will enable the proposed dispatch model to exist independently of the other model. This approach will expand the combination of generators dispatch to meet demand and increase the solar PV hosting capacity by committing fewer thermal generator units during periods of high solar irradiance.

3. The methodology presented in chapter 4 for estimating utility-scale battery system parameters is based on the manufacturer reported state of charge (SOC). The accuracy of the equivalent circuit model can be further improved by estimating the SOC of each cell through its performance evaluation and terminal voltage variation. Another step to improve the accuracy can be to include parameters such as self-discharge rate, state of health, and degradation rate in its

equivalent circuit model.

4. The detailed economical benefits, electrical losses and equipment degradation associated with the PV and BESS configuration proposed in chapter 5 can provide additional insight into its feasibility. Furthermore, the understanding of the proposed control stability during the transition between multiple operation modes may be used to develop safety limitations on the battery operation. Additionally, an improved battery sizing methodology, that takes into account the system's physical limitations and losses may be employed.

References

[1] F. Blaabjerg and D. M. Ionel, *Renewable Energy Devices and Systems with Simulations in MATLAB® and ANSYS®*. CRC Press, 2017.

[2] "IEEE standard for interconnection and interoperability of distributed energy resources with associated electric power systems interfaces," *IEEE Std 1547-2018 (Revision of IEEE Std 1547-2003)*, pp. 1–138, April 2018.

[3] F. Katiraei and J. R. Aguero, "Solar pv integration challenges," *IEEE Power and Energy Magazine*, vol. 9, no. 3, pp. 62–71, 2011.

[4] J. Johnson, "Collaborative development of automated advanced interoperability certification test protocols for pv smart grid integration." Sandia National Lab.(SNL-NM), Albuquerque, NM (United States), Tech. Rep., 2014.

[5] A. Marinopoulos, F. Papandrea, M. Reza, S. Norrga, F. Spertino, and R. Napoli, "Grid integration aspects of large solar pv installations: Lvrt capability and reactive power/voltage support requirements," in *2011 IEEE Trondheim PowerTech*. IEEE, 2011, pp. 1–8.

[6] Á. Molina-García, R. A. Mastromauro, T. García-Sánchez, S. Pugliese, M. Liserre, and S. Stasi, "Reactive power flow control for pv inverters voltage support in lv distribution networks," *IEEE Transactions on Smart Grid*, vol. 8, no. 1, pp. 447–456, 2016.

[7] L. Wang, R. Yan, and T. K. Saha, "Voltage regulation challenges with unbalanced pv integration in low voltage distribution systems and the corresponding solution," *Applied Energy*, vol. 256, p. 113927, 2019.

[8] C. Opathella, B. N. Singh, D. Cheng, and B. Venkatesh, "Intelligent wind generator models for power flow studies in pss® e and pss® sincal," *IEEE Transactions on Power Systems*, vol. 28, no. 2, pp. 1149–1159, 2012.

[9] M. Das and V. Agarwal, "Novel high-performance stand-alone solar pv system with high-gain high-efficiency dc–dc converter power stages," *IEEE Transactions on Industry Applications*, vol. 51, no. 6, pp. 4718–4728, 2015.

[10] J. He, T. Zhao, X. Jing, and N. A. Demerdash, "Application of wide bandgap devices in renewable energy systems-benefits and challenges," in *2014 International Conference on Renewable Energy Research and Application (ICRERA)*. IEEE, 2014, pp. 749–754.

[11] X. Guo, X. Zhang, H. Guan, T. Kerekes, and F. Blaabjerg, "Three-phase zvr topology and modulation strategy for transformerless pv system," *Ieee Transactions on Power Electronics*, vol. 34, no. 2, pp. 1017–1021, 2018.

[12] Y. Yang, S. Bremner, C. Menictas, and M. Kay, "Battery energy storage system size determination in renewable energy systems: A review," *Renewable and Sustainable Energy Reviews*, vol. 91, pp. 109–125, 2018.

[13] X. Xu, M. Bishop, D. G. Oikarinen, and C. Hao, "Application and modeling of battery energy storage in power systems," *CSEE Journal of Power and Energy Systems*, vol. 2, no. 3, pp. 82–90, 2016.

[14] D. S. Mallapragada, N. A. Sepulveda, and J. D. Jenkins, "Long-run system value of battery energy storage in future grids with increasing wind and solar generation," *Applied Energy*, vol. 275, p. 115390, 2020.

[15] D. Chathurangi, U. Jayatunga, S. Perera, and A. Agalgaonkar, "Evaluation of maximum solar pv penetration: Deterministic approach for over voltage curtailments," in *2019 IEEE PES Innovative Smart Grid Technologies Europe (ISGT-Europe)*. IEEE, 2019, pp. 1–5.

[16] H. Dai, D. S. Herran, S. Fujimori, and T. Masui, "Key factors affecting long-term penetration of global onshore wind energy integrating top-down and bottom-up approaches," *Renewable energy*, vol. 85, pp. 19–30, 2016.

[17] S. Lumbreras, A. Ramos, and F. Banez-Chicharro, "Optimal transmission network expansion planning in real-sized power systems with high renewable penetration," *Electric Power Systems Research*, vol. 149, pp. 76–88, 2017.

[18] I. S. Bayram, "Demand-side management for pv grid integration," in *Solar Resources Mapping*. Springer, 2019, pp. 313–325.

[19] H. M. Sultan, A. A. Z. Diab, O. N. Kuznetsov, Z. M. Ali, and O. Abdalla, "Evaluation of the impact of high penetration levels of pv power plants on the capacity, frequency and voltage stability of egypt's unified grid," *Energies*, vol. 12, no. 3, p. 552, 2019.

[20] L. Wen, K. Zhou, S. Yang, and X. Lu, "Optimal load dispatch of community microgrid with deep learning based solar power and load forecasting," *Energy*, vol. 171, pp. 1053–1065, 2019.

[21] Q. Li and S. Abhyankar, "Evaluation of high solar penetration impact on bulk system stability through a transmission-distribution dynamics co-simulation," in *2019 IEEE 3rd Conference on Energy Internet and Energy System Integration (EI2)*. IEEE, 2019, pp. 1–5.

[22] N. Naval, R. Sánchez, and J. M. Yusta, "A virtual power plant optimal dispatch model with large and small-scale distributed renewable generation," *Renewable Energy*, vol. 151, pp. 57–69, 2020.

[23] X. Yao, B. Yi, Y. Yu, Y. Fan, and L. Zhu, "Economic analysis of grid integration of variable solar and wind power with conventional power system," *Applied Energy*, vol. 264, p. 114706, 2020.

[24] M. Urbina and Z. Li, "A fuzzy optimization approach to PV/battery scheduling with uncertainty in pv generation," in *2006 38th North American Power Symposium*. IEEE, 2006, pp. 561–566.

[25] R. Bhat, M. Begovic, I. Kim, and J. Crittenden, "Effects of PV on conventional generation," in *2014 47th Hawaii International Conference on System Sciences*. IEEE, 2014, pp. 2380–2387.

[26] S. Wang, Y. Dong, L. Wu, and B. Yan, "Interval overvoltage risk based pv hosting capacity evaluation considering pv and load uncertainties," *IEEE Transactions on Smart Grid*, vol. 11, no. 3, pp. 2709–2721, 2019.

[27] V. Telukunta, J. Pradhan, A. Agrawal, M. Singh, and S. G. Srivani, "Protection challenges under bulk penetration of renewable energy resources in power systems: A review," *CSEE journal of power and energy systems*, vol. 3, no. 4, pp. 365–379, 2017.

[28] D. Flynn, Z. Rather, A. Ardal, S. D'Arco, A. D. Hansen, N. A. Cutululis, P. Sorensen, A. Estanquiero, E. Gomez, N. Menemenlis *et al.*, "Technical impacts of high penetration levels of wind power on power system stability," *Wiley Interdisciplinary Reviews: Energy and Environment*, vol. 6, no. 2, p. e216, 2017.

[29] H. He, R. Xiong, and J. Fan, "Evaluation of lithium-ion battery equivalent circuit models for state of charge estimation by an experimental approach," *energies*, vol. 4, no. 4, pp. 582–598, 2011.

[30] T. Feng, L. Yang, X. Zhao, H. Zhang, and J. Qiang, "Online identification of lithium-ion battery parameters based on an improved equivalent-circuit model and its implementation on battery state-of-power prediction," *Journal of Power Sources*, vol. 281, pp. 192–203, 2015.

[31] F. Zhong, H. Li, S. Zhong, Q. Zhong, and C. Yin, "An SOC estimation approach based on adaptive sliding mode observer and fractional order equivalent circuit model for lithium-ion batteries," *Communications in Nonlinear Science and Numerical Simulation*, vol. 24, no. 1-3, pp. 127–144, 2015.

[32] E. Muljadi, M. Singh, R. Bravo, and V. Gevorgian, "Dynamic model validation of pv inverters under short-circuit conditions," in *2013 IEEE Green Technologies Conference (GreenTech)*. IEEE, 2013, pp. 98–104.

[33] E. Muljadi, M. Singh, and V. Gevorgian, "User guide for pv dynamic model simulation written on pscad platform," National Renewable Energy Lab.(NREL), Golden, CO (United States), Tech. Rep., 2014.

[34] X. Hu, F. Sun, Y. Zou, and H. Peng, "Online estimation of an electric vehicle lithium-ion battery using recursive least squares with forgetting," in *Proceedings of the 2011 American Control Conference*. IEEE, 2011, pp. 935–940.

[35] X. Guo, L. Kang, Y. Yao, Z. Huang, and W. Li, "Joint estimation of the electric vehicle power battery state of charge based on the least squares method and the kalman filter algorithm," *Energies*, vol. 9, no. 2, p. 100, 2016.

[36] F. Sun, X. Hu, Y. Zou, and S. Li, "Adaptive unscented kalman filtering for state of charge estimation of a lithium-ion battery for electric vehicles," *Energy*, vol. 36, no. 5, pp. 3531–3540, 2011.

[37] X. Tang, X. Mao, J. Lin, and B. Koch, "Li-ion battery parameter estimation for state of charge," in *Proceedings of the 2011 American control conference*. IEEE, 2011, pp. 941–946.

[38] T. F. Wu, C. H. Chang, L. C. Lin, and C. L. Kuo, "Power loss comparison of single- and two-stage grid-connected photovoltaic systems," vol. 26, no. 2, June 2011, pp. 707–715.

[39] Y. Zhu, J. Yao, and D. Wu, "Comparative study of two stages and single stage topologies for grid-tie photovoltaic generation by PSCAD/EMTDC," in *2011 International Conference on Advanced Power System Automation and Protection*, vol. 2, Oct 2011, pp. 1304–1309.

[40] A. Merabet, K. T. Ahmed, H. Ibrahim, R. Beguenane, and A. M. Y. M. Ghias, "Energy management and control system for laboratory scale microgrid based

wind-pv-battery," *IEEE Transactions on Sustainable Energy*, vol. 8, no. 1, pp. 145–154, Jan 2017.

[41] M. Rezkallah, A. Hamadi, A. Chandra, and B. Singh, "Real-time HIL implementation of sliding mode control for standalone system based on pv array without using dumpload," *IEEE Transactions on Sustainable Energy*, vol. 6, no. 4, pp. 1389–1398, Oct 2015.

[42] O. M. Akeyo, V. Rallabandi, N. J. A. Patrick, and D. M. Ionel, "Parameter identification for cells, modules, racks, and battery for utility-scale energy storage systems," *IEEE Transactions on Industry Applications*, 2020.

[43] O. M. Akeyo, V. Rallabandi, N. Jewell, and D. M. Ionel, "The design and analysis of large solar pv farm configurations with dc-connected battery systems," *IEEE Transactions on Industry Applications*, vol. 56, no. 3, pp. 2903–2912, 2020.

[44] V. Rallabandi, O. M. Akeyo, N. Jewell, and D. M. Ionel, "Incorporating battery energy storage systems into multi-mw grid connected pv systems," *IEEE Transactions on Industry Applications*, vol. 55, no. 1, pp. 638–647, 2018.

[45] O. Akeyo, A. Patrick, and D. M. Ionel, "Impact of high renewable energy penetration on a benchmark transmission system," in *2020 IEEE Power Energy Society General Meeting (PESGM)*, 2020, pp. 1–5.

[46] O. M. Akeyo, V. Rallabandi, N. Jewell, and D. M. Ionel, "Measurement and estimation of the equivalent circuit parameters for multi-mw battery systems," in *2019 IEEE Energy Conversion Congress and Exposition (ECCE)*. IEEE, pp. 2499–2504.

[47] O. Akeyo, V. Rallabandi, N. Jewell, and D. M. Ionel, "Modeling and simulation of a utility-scale battery energy storage system," in *2019 IEEE Power Energy Society General Meeting (PESGM)*, 2019, pp. 1–5.

[48] O. Akeyo, H. Gong, V. Rallabandi, N. Jewell, and D. M. Ionel, "Power utility tests for multi-mw high energy batteries," in *2018 7th International Conference on Renewable Energy Research and Applications (ICRERA)*, 2018, pp. 1396–1399.

[49] O. Akeyo, V. Rallabandi, N. Jewell, and D. M. Ionel, "Improving the capacity factor and stability of multi-mw grid connected pv systems with results from a 1mw/2mwh battery demonstrator," in *2018 IEEE Energy Conversion Congress and Exposition (ECCE)*, Sep. 2018, pp. 2504–2509.

[50] O. M. Akeyo, V. Rallabandi, and D. M. Ionel, "Multi-MW solar PV pumping system with capacity modulation and battery voltage support," in *2017 IEEE 6th International Conference on Renewable Energy Research and Applications (ICRERA)*, Nov 2017, pp. 423–428.

[51] V. Rallabandi, O. M. Akeyo, and D. M. Ionel, "Modeling of a multi-megawatt grid connected PV system with integrated batteries," in *2016 IEEE International Conference on Renewable Energy Research and Applications (ICRERA)*, Nov, pp. 1146–1151.

[52] A. S. Aziz, M. F. N. Tajuddin, M. R. Adzman, M. F. Mohammed, and M. A. Ramli, "Feasibility analysis of grid-connected and islanded operation of a solar pv microgrid system: A case study of iraq," *Energy*, vol. 191, p. 116591, 2020.

[53] B. Malakondareddy, S. S. Kumar, N. A. Gounden, and I. Anand, "An adaptive pi control scheme to balance the neutral-point voltage in a solar pv fed grid connected neutral point clamped inverter," *International Journal of Electrical Power & Energy Systems*, vol. 110, pp. 318–331, 2019.

[54] S. Sheik Mohammed, D. Devaraj, and T. P. Imthias Ahamed, "Maximum power point tracking system for stand alone solar pv power system using adaptive neuro-fuzzy inference system," in *2016 Biennial International Conference on Power and Energy Systems: Towards Sustainable Energy (PESTSE)*, 2016, pp. 1–4.

[55] A. Sangwongwanich and F. Blaabjerg, "Mitigation of interharmonics in pv systems with maximum power point tracking modification," *IEEE Transactions on Power Electronics*, vol. 34, no. 9, pp. 8279–8282, 2019.

[56] S. K. Chattopadhyay and C. Chakraborty, "A new asymmetric multilevel inverter topology suitable for solar pv applications with varying irradiance," *IEEE Transactions on Sustainable Energy*, vol. 8, no. 4, pp. 1496–1506, 2017.

[57] S. Bandyopadhyay, G. R. C. Mouli, Z. Qin, L. R. Elizondo, and P. Bauer, "Techno-economical model based optimal sizing of pv-battery systems for microgrids," *IEEE Transactions on Sustainable Energy*, vol. 11, no. 3, pp. 1657–1668, 2020.

[58] B. Mirafzal and A. Adib, "On grid-interactive smart inverters: Features and advancements," *IEEE Access*, vol. 8, pp. 160 526–160 536, 2020.

[59] D. P. Hohm and M. E. Ropp, "Comparative study of maximum power point tracking algorithms using an experimental, programmable, maximum power point tracking test bed," in *Photovoltaic Specialists Conference, 2000. Conference Record of the Twenty-Eighth IEEE*, pp. 1699–1702.

[60] A. Sangwongwanich, Y. Yang, and F. Blaabjerg, "High-performance constant power generation in grid-connected pv systems," *IEEE Transactions on Power Electronics*, vol. 31, no. 3, pp. 1822–1825, March 2016.

[61] K. A. Corzine, S. D. Sudhoff, and C. A. Whitcomb, "Performance characteristics of a cascaded two-level converter," *IEEE Transactions on Energy Conversion*, vol. 14, no. 3, pp. 433–439, Sep 1999.

[62] Power systems test case archive. [Online]. Available: https://www2.ee.washington.edu/research/pstca/

[63] "Ieee 14 bus knowledge base," https://hvdc.ca/, accessed: 2016-08-03.

[64] D. Greenwood, K. Lim, C. Patsios, P. Lyons, Y. Lim, and P. Taylor, "Frequency response services designed for energy storage," *Applied Energy*, vol. 203, pp. 115 – 127, 2017.

[65] E. Thorbergsson, V. Knap, M. Swierczynski, D. Stroe, and R. Teodorescu, "Primary frequency regulation with Li-ion battery based energy storage system-evaluation and comparison of different control strategies," in *Telecommunications Energy Conference'Smart Power and Efficiency'(INTELEC), Proceedings of 2013 35th International*. VDE, 2013, pp. 1–6.

[66] Y. Yang, F. Blaabjerg, and H. Wang, "Constant power generation of photovoltaic systems considering the distributed grid capacity," in *IEEE Applied Power Electronics Conference and Exposition - APEC*, March 2014, pp. 379–385.

[67] D. Cusick, "Scientific American: Battery storage poised to expand rapidly," https://www.scientificamerican.com/article/battery-storage-poised-to-expand-rapidly/, accessed: 2017-12-27.

[68] "Gravity Power Grid Scale Energy Storage," www.gravitypower.net, accessed: 2017-12-27.

[69] J. Nelson, S. Kasina, J. Stevens, J. Moore, A. Olson, M. Morjaria, J. Smolenski, and J. Aponte, "Investigating the economic value of flexible solar power plant operation," *Energy and Environmental Economics, Inc*, 2018.

[70] M. Basu, "Multi-region dynamic economic dispatch of solar–wind–hydro–thermal power system incorporating pumped hydro energy storage," *Engineering Applications of Artificial Intelligence*, vol. 86, pp. 182–196, 2019.

[71] J. Bai, T. Ding, Z. Wang, and J. Chen, "Day-ahead robust economic dispatch considering renewable energy and concentrated solar power plants," *Energies*, vol. 12, no. 20, p. 3832, 2019.

[72] A. Tavakoli, S. Saha, M. T. Arif, M. E. Haque, N. Mendis, and A. M. T. Oo, "Impacts of grid integration of solar pv and electric vehicle on grid stability, power quality and energy economics: a review," *IET Energy Systems Integration*, vol. 2, no. 3, pp. 243–260, 2020.

[73] V. Singhvi and D. Ramasubramanian, "Renewable generation hosting capacity screening tool for a transmission network," Electric Power Research Institute (EPRI), Knoxville, TN, Tech. Rep., 2018.

[74] V. K. Jadoun, V. C. Pandey, N. Gupta, K. R. Niazi, and A. Swarnkar, "Integration of renewable energy sources in dynamic economic load dispatch problem using an improved fireworks algorithm," *IET Renewable Power Generation*, vol. 12, no. 9, pp. 1004–1011, 2018.

[75] S. Singh and D. W. Gao, "Noiseless consensus based algorithm for economic dispatch problem in grid-connected microgrids to enhance stability among distributed generators," in *2019 North American Power Symposium (NAPS)*. IEEE, 2019, pp. 1–5.

[76] T.-Y. Kim, G.-H. Won, and Y. Chung, "Optimal dispatch and unit commitment strategies for multiple diesel generators in shipboard power system using dynamic programming," in *2018 21st International Conference on Electrical Machines and Systems (ICEMS)*. IEEE, 2018, pp. 2754–2757.

[77] P. H. Divshali and L. Söder, "Improving pv dynamic hosting capacity using adaptive controller for statcoms," *IEEE Transactions on Energy Conversion*, vol. 34, no. 1, pp. 415–425, 2019.

[78] R. Mahroo-Bakhtiari, M. Izadi, A. Safdarian, and M. Lehtonen, "Distributed load management scheme to increase pv hosting capacity in lv feeders," *IET Renewable Power Generation*, vol. 14, no. 1, pp. 125–133, 2020.

[79] D. Diaz, A. Kumar, J. Deboever, S. Grijalva, J. Peppanen, M. Rylander, and

J. Smith, "Scenario-selection for hosting capacity analysis of distribution feeders with voltage regulation equipment," in *2019 IEEE Power Energy Society Innovative Smart Grid Technologies Conference (ISGT)*, Feb 2019, pp. 1–5.

[80] D. J. Feldman and R. M. Margolis, "Q4 2018/q1 2019 solar industry update," National Renewable Energy Lab.(NREL), Golden, CO (United States), Tech. Rep., 2019.

[81] B. Crăciun, T. Kerekes, D. Séra, R. Teodorescu, and A. Timbus, "Benchmark networks for grid integration impact studies of large pv plants," in *2013 IEEE Grenoble Conference*, June 2013, pp. 1–6.

[82] N. A. Khan, G. A. S. Sidhu, and F. Gao, "Optimizing combined emission economic dispatch for solar integrated power systems," *IEEE Access*, vol. 4, pp. 3340–3348, 2016.

[83] V. K. Jadoun, V. C. Pandey, N. Gupta, K. R. Niazi, and A. Swarnkar, "Integration of renewable energy sources in dynamic economic load dispatch problem using an improved fireworks algorithm," *IET Renewable Power Generation*, vol. 12, no. 9, pp. 1004–1011, 2018.

[84] A. Adamczyk, M. Altin, . Göksu, R. Teodorescu, and F. Iov, "Generic 12-bus test system for wind power integration studies," in *2013 15th European Conference on Power Electronics and Applications (EPE)*, Sep. 2013, pp. 1–6.

[85] "Live solar generation data." [Online]. Available: https://lge-ku.com/live-solar-generation

[86] "Standard BAL-001-1 - real power balancing control performance," *North American Electric Reliability Corporation (NERC)*.

[87] "Standard BAL-002-1 - real power balancing control performance," *North American Electric Reliability Corporation (NERC)*.

[88] J. D. Glover, M. S. Sarma, and T. Overbye, *Power system analysis & design, SI version*. Cengage Learning, 2012.

[89] P. Kokopeli, J. Schreifels, and R. Forte, "Assessment of startup period at coal-fired electric generating units," *US Environmental Protection Agency, Office of Air and Radiation, technical report, Document ID: EPA-HQ-OAR-2009-0234-20378 [online] http://www. epa. gov/airquality/powerplanttoxics/pdfs/matsstartstsd. pdf (accessed 20 November 2013)*, 2013.

[90] T. O. Olowu, A. Sundararajan, M. Moghaddami, and A. I. Sarwat, "Future challenges and mitigation methods for high photovoltaic penetration: A survey," *Energies*, vol. 11, no. 7, p. 1782, 2018.

[91] "IEEE standard conformance test procedures for equipment interconnecting distributed energy resources with electric power systems and associated interfaces," *IEEE Std 1547.1-2020*, pp. 1–282, 2020.

[92] "Proposal to revise standard generator interconnection agreements," North American Electric Reliability Corporation (NERC), Standard.

[93] P. Unahalekhaka and P. Sripakarach, "Reduction of reverse power flow using the appropriate size and installation position of a bess for a pv power plant," *IEEE Access*, vol. 8, pp. 102 897–102 906, 2020.

[94] M. Ahmadi, M. E. Lotfy, R. Shigenobu, A. M. Howlader, and T. Senjyu, "Optimal sizing of multiple renewable energy resources and pv inverter reactive power control encompassing environmental, technical, and economic issues," *IEEE Systems Journal*, vol. 13, no. 3, pp. 3026–3037, 2019.

[95] J. Rocabert, R. Capó-Misut, R. S. Muñoz-Aguilar, J. I. Candela, and P. Rodriguez, "Control of energy storage system integrating electrochemical batteries and supercapacitors for grid-connected applications," *IEEE Transactions on Industry Applications*, vol. 55, no. 2, pp. 1853–1862, 2019.

[96] A. Adamczyk, M. Altin, Ö. Göksu, R. Teodorescu, and F. Iov, "Generic 12-bus test system for wind power integration studies," in *2013 15th European*

Conference on Power Electronics and Applications (EPE). IEEE, 2013, pp. 1–6.

[97] A. Mahendru and R. K. Varma, "Reduction in system losses and power demand by combination of optimal power flow and conservation voltage reduction using smart pv inverters," in *2019 IEEE Power Energy Society General Meeting (PESGM)*, 2019, pp. 1–5.

[98] K. A. Kumar, M. P. Selvan, and K. Rajapandiyan, "Dynamic grid support system for mitigation of impact of high penetration solar pv into grid," in *2017 7th International Conference on Power Systems (ICPS)*, 2017, pp. 646–652.

[99] P. Wu, W. Huang, and N. Tai, "Novel grid connection interface for utility-scale pv power plants based on mmc," *The Journal of Engineering*, vol. 2019, no. 16, pp. 2683–2686, 2019.

[100] S. T. Ojetola, J. Wold, D. Trudnowski, F. Wilches Bernal, and R. T. Elliott, "A real power injection control strategy for improving transient stability." Sandia National Lab.(SNL-NM), Albuquerque, NM (United States), Tech. Rep., 2019.

[101] *U.S. Battery Storage Market Trends*. U.S. Energy Information Administration, May 2018.

[102] F. Blaabjerg and D. M. Ionel, *Renewable energy devices and systems with simulations in MATLAB® and ANSYS®*. CRC Press, 2017.

[103] C. Zhao, J. Sun, and Q. Wang, "Thermal runaway hazards investigation on 18650 lithium-ion battery using extended volume accelerating rate calorimeter," *Journal of Energy Storage*, vol. 28, p. 101232, 2020. [Online]. Available: http://www.sciencedirect.com/science/article/pii/S2352152X19311077

[104] X. Feng, M. Ouyang, X. Liu, L. Lu, Y. Xia, and X. He, "Thermal runaway mechanism of lithium ion battery for electric vehicles: A review," *Energy Storage Materials*, vol. 10, pp. 246–267, 2018.

[105] H. V. Nguyen, D. To, and D. Lee, "Onboard battery chargers for plug-in electric vehicles with dual functional circuit for low-voltage battery charging and active power decoupling," *IEEE Access*, vol. 6, pp. 70 212–70 222, 2018.

[106] M. Y. Metwly, M. S. Abdel-Majeed, A. S. Abdel-Khalik, R. A. Hamdy, M. S. Hamad, and S. Ahmed, "A review of integrated on-board ev battery chargers: Advanced topologies, recent developments and optimal selection of FSCW slot/pole combination," *IEEE Access*, vol. 8, pp. 85 216–85 242, 2020.

[107] R. Kushwaha and B. Singh, "Power factor improvement in modified bridgeless landsman converter fed ev battery charger," *IEEE Transactions on Vehicular Technology*, vol. 68, no. 4, pp. 3325–3336, 2019.

[108] M. Restrepo, J. Morris, M. Kazerani, and C. A. Cañizares, "Modeling and testing of a bidirectional smart charger for distribution system ev integration," *IEEE Transactions on Smart Grid*, vol. 9, no. 1, pp. 152–162, 2018.

[109] D. Dvorak, T. Bäuml, A. Holzinger, and H. Popp, "A comprehensive algorithm for estimating lithium-ion battery parameters from measurements," *IEEE Transactions on Sustainable Energy*, vol. 9, no. 2, pp. 771–779, April 2018.

[110] C. R. Lashway and O. A. Mohammed, "Adaptive battery management and parameter estimation through physics-based modeling and experimental verification," *IEEE Transactions on Transportation Electrification*, vol. 2, no. 4, pp. 454–464, Dec 2016.

[111] H. M. Usman, S. Mukhopadhyay, and H. Rehman, "Universal adaptive stabilizer based optimization for li-ion battery model parameters estimation: An experimental study," *IEEE Access*, vol. 6, pp. 49 546–49 562, 2018.

[112] S. A. Hamidi, D. M. Ionel, and A. Nasiri, "Batteries and ultracapacitors for electric power systems with renewable energy sources," *Renewable Energy Devices and Systems with Simulations in MATLAB® and ANSYS®*, 2017.

[113] A. Biswas, R. Gu, P. Kollmeyer, R. Ahmed, and A. Emadi, "Simultaneous state and parameter estimation of li-ion battery with one state hysteresis model using augmented unscented kalman filter," in *2018 IEEE Transportation Electrification Conference and Expo (ITEC)*, June 2018, pp. 1065–1070.

[114] D. C. Cambron and A. M. Cramer, "A lithium-ion battery current estimation technique using an unknown input observer," *IEEE Transactions on Vehicular Technology*, vol. 66, no. 8, pp. 6707–6714, Aug 2017.

[115] A. M. Bizeray, J. Kim, S. R. Duncan, and D. A. Howey, "Identifiability and parameter estimation of the single particle lithium-ion battery model," *IEEE Transactions on Control Systems Technology*, pp. 1–16, 2018.

[116] R. Gu, P. Malysz, H. Yang, and A. Emadi, "On the suitability of electrochemical-based modeling for lithium-ion batteries," *IEEE Transactions on Transportation Electrification*, vol. 2, no. 4, pp. 417–431, 2016.

[117] F. Feng, X. Hu, K. Liu, Y. Che, X. Lin, G. Jin, and B. Liu, "A practical and comprehensive evaluation method for series-connected battery pack models," *IEEE Transactions on Transportation Electrification*, vol. 6, no. 2, pp. 391–416, 2020.

[118] J. Lee, J. Ahn, and B. K. Lee, "A novel li-ion battery pack modeling considerging single cell information and capacity variation," in *2017 IEEE Energy Conversion Congress and Exposition (ECCE)*, 2017, pp. 5242–5247.

[119] J. Meng, D. Stroe, M. Ricco, G. Luo, and R. Teodorescu, "A simplified model-based state-of-charge estimation approach for lithium-ion battery with dynamic linear model," *IEEE Transactions on Industrial Electronics*, vol. 66, no. 10, pp. 7717–7727, 2019.

[120] H. Chun, M. Kim, J. Kim, K. Kim, J. Yu, T. Kim, and S. Han, "Adaptive exploration harmony search for effective parameter estimation in an electrochemical lithium-ion battery model," *IEEE Access*, vol. 7, pp. 131 501–131 511, 2019.

[121] *Energy Storage Integration Council (ESIC) Energy Storage Test Manual*. EPRI, Palo Alto, CA: 2017. 3002011739.

[122] Z. Yu, L. Xiao, H. Li, X. Zhu, and R. Huai, "Model parameter identification for lithium batteries using the coevolutionary particle swarm optimization method," *IEEE Transactions on Industrial Electronics*, vol. 64, no. 7, pp. 5690–5700, 2017.

[123] M. Partovibakhsh and G. Liu, "An adaptive unscented kalman filtering approach for online estimation of model parameters and state-of-charge of lithium-ion batteries for autonomous mobile robots," *IEEE Transactions on Control Systems Technology*, vol. 23, no. 1, pp. 357–363, 2015.

[124] X. Liu, W. Li, and A. Zhou, "PNGV equivalent circuit model and soc estimation algorithm for lithium battery pack adopted in AGV vehicle," *IEEE Access*, vol. 6, pp. 23 639–23 647, 2018.

[125] V. Rallabandi, O. M. Akeyo, N. Jewell, and D. M. Ionel, "Incorporating battery energy storage systems into multi-MW grid connected PV systems," *IEEE Transactions on Industry Applications*, pp. 1–1, 2018.

[126] F. Blaabjerg and D. M. Ionel, "Renewable energy devices and systems – state-of-the-art technology, research and development, challenges and future trends," *Electric Power Components and Systems*, vol. 43, no. 12, pp. 1319–1328, 2015.

[127] S. Jain, R. Karampuri, and V. T. Somasekhar, "An integrated control algorithm for a single-stage pv pumping system using an open-end winding induction motor," *IEEE Transactions on Industrial Electronics*, vol. 63, no. 2, pp. 956–965, Feb 2016.

[128] J. Sachs and O. Sawodny, "A two-stage model predictive control strategy for economic diesel-PV-battery island microgrid operation in rural areas," *IEEE Transactions on Sustainable Energy*, vol. 7, no. 3, pp. 903–913, July 2016.

[129] V. Karthikeyan and R. Gupta, "Varying phase angle control in isolated bidirectional dc 8211;DC converter for integrating battery storage and solar PV system in standalone mode," *IET Power Electronics*, vol. 10, no. 4, pp. 471–479, 2017.

[130] Y. Chang, Y. Feng, W. Chiang, R. Chang, M. Chiueh, and T. Holtz, "5kw dc-coupling distribution power generation system based on photovoltaic and aqueous hybrid ion battery," in *2017 IEEE 3rd International Future Energy Electronics Conference and ECCE Asia (IFEEC 2017 - ECCE Asia)*, June 2017, pp. 1719–1724.

[131] Kyohei Kurohane, T. Senjyu, Akie Uehara, A. Yona, T. Funabashi, and Chul-Hwan Kim, "A hybrid smart ac/dc power system," in *2010 5th IEEE Conference on Industrial Electronics and Applications*, June 2010, pp. 764–769.

[132] T. Ma, M. H. Cintuglu, and O. A. Mohammed, "Control of a hybrid ac/dc microgrid involving energy storage and pulsed loads," *IEEE Transactions on Industry Applications*, vol. 53, no. 1, pp. 567–575, Jan 2017.

[133] V. Rallabandi, O. M. Akeyo, N. Jewell, and D. M. Ionel, "Incorporating battery energy storage systems into multi-mw grid connected pv systems," *IEEE Transactions on Industry Applications*, vol. 55, no. 1, pp. 638–647, Jan 2019.

[134] H. Mahmood, D. Michaelson, and J. Jiang, "Strategies for independent deployment and autonomous control of PV and battery units in islanded microgrids," *IEEE Journal of Emerging and Selected Topics in Power Electronics*, vol. 3, no. 3, pp. 742–755, Sept 2015.

[135] N. A. DiOrio, J. M. Freeman, and N. Blair, "Dc-connected solar plus storage modeling and analysis for behind-the-meter systems in the system advisor model," in *2018 IEEE 7th World Conference on Photovoltaic Energy Conversion (WCPEC) (A Joint Conference of 45th IEEE PVSC, 28th PVSEC 34th EU PVSEC)*, June 2018, pp. 3777–3782.

[136] M. O. Badawy and Y. Sozer, "Power flow management of a grid tied PV-battery system for electric vehicles charging," *IEEE Transactions on Industry Applications*, vol. 53, no. 2, pp. 1347–1357, March 2017.

[137] N. Saxena, I. Hussain, B. Singh, and A. L. Vyas, "Implementation of a grid-integrated PV-battery system for residential and electrical vehicle applications," *IEEE Transactions on Industrial Electronics*, vol. 65, no. 8, pp. 6592–6601, Aug 2018.

[138] P. Satapathy, S. Dhar, and P. K. Dash, "Stability improvement of PV-BESS diesel generator-based microgrid with a new modified harmony search-based hybrid firefly algorithm," *IET Renewable Power Generation*, vol. 11, no. 5, pp. 566–577, 2017.

[139] R. Teichmann and S. Bernet, "A comparison of three-level converters versus two-level converters for low-voltage drives, traction, and utility applications," *IEEE Transactions on Industry Applications*, vol. 41, no. 3, pp. 855–865, May 2005.

[140] *Utility Scale Solar Inverter*, Power Electronics.

[141] S. Chen, T. Huang, S. S. Ng, K. Lin, M. Du, Y. Kang, K. Chen, C. Wey, Y. Lin, C. Lee, J. Lin, and T. Tsai, "A direct ac–dc and dc–dc cross-source energy harvesting circuit with analog iterating-based mppt technique with 72.5efficiency," *IEEE Transactions on Power Electronics*, vol. 31, no. 8, pp. 5885–5899, Aug 2016.

[142] A. Sangwongwanich, Y. Yang, and F. Blaabjerg, "A cost-effective power ramp-rate control strategy for single-phase two-stage grid-connected photovoltaic systems," in *2016 IEEE Energy Conversion Congress and Exposition (ECCE)*, Sept 2016, pp. 1–7.

[143] D. Cormode, A. D. Cronin, W. Richardson, A. T. Lorenzo, A. E. Brooks, and D. N. DellaGiustina, "Comparing ramp rates from large and small PV systems,

and selection of batteries for ramp rate control," in *2013 IEEE 39th Photovoltaic Specialists Conference (PVSC)*, June 2013, pp. 1805–1810.

[144] W. A. Omran, M. Kazerani, and M. M. A. Salama, "Investigation of methods for reduction of power fluctuations generated from large grid-connected photovoltaic systems," *IEEE Transactions on Energy Conversion*, vol. 26, no. 1, pp. 318–327, March 2011.

[145] R. Yan and T. K. Saha, "Power ramp rate control for grid connected photovoltaic system," in *2010 Conference Proceedings IPEC*, Oct 2010, pp. 83–88.

Vita

Oluwaseun Akeyo, PhD Candidate

Department of Electrical and Computer Engineering, University of Kentucky

Seun Akeyo is a Ph.D. candidate in Electrical Engineering at University of Kentucky (UK), He started his studies at UK in 2016 and since then also served within the Electrical and Computer Engineering Department as a TA and as an RA in the SPARK Laboratory. Akeyo received his B. Eng. degree in Electrical and Electronics Engineering from Abubakar Tafawa Balewa University (ATBU), Bauchi, Nigeria and his MS in Electrical Engineering from UK in 2017. His main research interests are in the integration of renewable energy and energy storage in the electrical power system. His research at UK contributed to projects sponsored by DOE and in close collaboration with large utilities especially LG&E-KU. Akeyo published more than fifteen journal and conference peer-reviewed proceedings papers. He participated and presented at the large conferences including ECCE 2018, ECCE 2019, PESGM 2019 and IASAM 2020 and attended the 2018 FEEDER DOE Sponsored Summer Institute program at the University of South Carolina, where he won the best presentation award. His publications include a Best Poster/Paper Award at the 2016 IEEE International Conference on Renewable Energy Research and Applications (ICRERA) in Birmingham, England, and the 2020 Best Paper Award - Third Prize from the IEEE Industry Application Society (IAS) RESCCS based on a paper published in IEEE Transactions on Industry Applications, Vol. 55.